ELSEVIER

Surface Science Reports 47 (2002) 197–301

surface science reports

www.elsevier.com/locate/surfrep

Dynamic atomic force microscopy methods

Ricardo García[a,*], Rubén Pérez[b]

[a]*Instituto de Microelectrónica de Madrid, CSIC, Isaac Newton 8, 28760 Tres Cantos, Madrid, Spain*
[b]*Departamento de Física Teórica de la Materia Condensada, Universidad Autónoma de Madrid, E-28049 Madrid, Spain*

Manuscript received in final form 15 April 2002

Abstract

In this report we review the fundamentals, applications and future tendencies of dynamic atomic force microscopy (AFM) methods. Our focus is on understanding why the changes observed in the dynamic properties of a vibrating tip that interacts with a surface make possible to obtain molecular resolution images of membrane proteins in aqueous solutions or to resolve atomic-scale surface defects in ultra high vacuum (UHV). Our description of the two major dynamic AFM modes, amplitude modulation atomic force microscopy (AM-AFM) and frequency modulation atomic force microscopy (FM-AFM) emphasises their common points without ignoring the differences in experimental set-ups and operating conditions. Those differences are introduced by the different feedback parameters, oscillation amplitude in AM-AFM and frequency shift and excitation amplitude in FM-AFM, used to track the topography and composition of a surface.

The theoretical analysis of AM-AFM (also known as tapping-mode) emphasises the coexistence, in many situations of interests, of two stable oscillation states, a low and high amplitude solution. The coexistence of those oscillation states is a consequence of the presence of attractive and repulsive components in the interaction force and their non-linear dependence on the tip–surface separation. We show that key relevant experimental properties such as the lateral resolution, image contrast and sample deformation are highly dependent on the oscillation state chosen to operate the instrument. AM-AFM allows to obtain simultaneous topographic and compositional contrast in heterogeneous samples by recording the phase angle difference between the external excitation and the tip motion (phase imaging). Significant applications of AM-AFM such as high-resolution imaging of biomolecules and polymers, large-scale patterning of silicon surfaces, manipulation of single nanoparticles or the fabrication of single electron devices are also reviewed.

FM-AFM (also called non-contact AFM—NC-AFM) has achieved the long-standing goal of true atomic resolution with AFM in UHV. Our analysis starts with a discussion of the relation between frequency shifts and tip–surface interactions, emphasising the ability of perturbation theory to describe the measured frequency shift. We discuss the role of short-range chemical interactions in the atomic contrast, with particular attention to semiconductor and ionic (alkali halides and oxides) surfaces. Also included is a detailed quantitative comparison between theoretical simulations and experiment. Inversion procedures, the determination of the tip–sample

* Corresponding author. Tel.: +34-91-806-07-00; fax: +34-91-806-07-01.
E-mail address: rgarcia@imm.cnm.csic.es (R. García).

0167-5729/02/$ – see front matter
PII: S0167-5729(02)00077-8

interaction from the frequency shift versus distance curves above specific sites, are also reviewed. We finish with a discussion of the optimal range of experimental operation parameters, and the use of damping (excitation amplitude) as a source of atomic contrast, including the possible interpretation in terms of microscopic dissipation mechanisms.

PACS: 68.37Ps; 07.79.Lh; 87.64.Dz

Keywords: Atomic force microscopy; Tapping-mode AFM; Amplitude modulation AFM; Frequency modulation AFM; Dynamic force microscopy; Scanning probe microscopy

Contents

1. Introduction

In the last decade the atomic force microscope (AFM) invented by Binnig et al. [1] experienced a significant transformation when a vibrating probe was used to explore the surface topography [2,3]. Since then, dynamic AFM methods are emerging as powerful and versatile techniques for atomic and nanometer-scale characterisation and manipulation of a wide variety of surfaces. High-resolution images of DNA, proteins and polymers have been obtained in air and liquids [4–8]. *True* atomic resolution images of several semiconductor and insulator surfaces [9–11] have also been reported.

Additionally, dynamic AFM modes are being applied to develop methods for nanometer-scale modification and patterning of surfaces [12].

The interest and sophistication of dynamic AFM modes stems on four factors: (i) routine nanometer-scale spatial resolution of semiconductors, polymers and biomolecules and atomic resolution images of insulator surfaces in ultra high vacuum (UHV); (ii) the existence of several parameters sensitive to the tip–sample interactions (amplitude, frequency, phase shift and cantilever deflection); (iii) the challenging features of the motion of a vibrating tip interacting with a surface and (iv) the potential to develop quantitative methods to characterise material properties at nanometer scale.

The amplitude, the resonance frequency and the phase shift of the oscillation link the dynamics of a vibrating tip to the tip–surface interactions. Any of them could be used as a feedback parameter to track the topography of a surface. Presently, two major dynamic AFM modes, amplitude modulation atomic force microscopy (AM-AFM) [2,13] and frequency modulation atomic force microscopy (FM-AFM) [3] are being developed to measure the topography of a sample surface. In AM-AFM (also known as tapping-mode), a stiff microlever, which has a sharp tip at its free end, is excited at or near its free resonance frequency. The oscillation amplitude is used as a feedback parameter to measure the topography of the sample surface. Additionally, material properties variations could be mapped by recording the phase shift between the driving force and the tip oscillation. On the other hand, in frequency modulation the cantilever is kept oscillating with a fixed amplitude at its resonance frequency. This resonance frequency depends on the forces acting between tip and sample surface. The spatial dependence of the frequency shift, the difference between the actual resonance frequency and that of the free lever, is the source of contrast. An image is formed by profiling the surface topography with a constant frequency shift. Most experiments in UHV are performed in FM-AFM while the majority of the experiments in air or in liquids are performed in AM-AFM.

The FM-AFM was also called the non-contact AFM (NC-AFM) because atomic resolution images in UHV were obtained without tip–surface mechanical contact. However, later developments have shown that FM-AFM can be used to probe the tip–surface interaction in the repulsive regime. On the other hand, it has been demonstrated that the AM-AFM can be operated in a *real* non-contact mode. Thus, operation in non-contact or intermittent contact mode is not exclusive of a given dynamic AFM method. For the above reason we consider more clarifying to refer the different experiments according to the dynamic AFM mode used.

To a certain extent the dynamics of a vibrating tip in the proximity of a surface and the interactions experienced by the tip are independent of the dynamic method used. However, the emphasis in different experimental quantities, amplitude and phase shift in amplitude modulation, and resonance frequency and amplitude in frequency modulation implies rather different experimental set-ups. As a consequence, the understanding of the tip motion has evolved independently. Two different scientific communities have emerged with the prevailing impression that amplitude and frequency modulation methods have little in common.

In this contribution we review the fundamentals, applications and future trends of dynamic AFM methods. We attempt to describe and understand why the changes observed in the dynamic properties of a vibrating tip that interacts with a surface make it possible to obtain molecular resolution images of membrane proteins in aqueous solutions or to resolve atomic-scale defects of semiconductor surfaces in UHV. Our goal is to provide a description of AM- and FM-AFM methods that emphasises their common points without ignoring their differences. Currently, AM-AFM is used in air or liquid environments while FM-AFM is mostly used in UHV environments. This division is not artificial.

Amplitude modulation will be an unlike technique for UHV because the high quality factor of the microlever ($Q \sim 10^4$) would imply extremely slow feedback responses. On the other hand, FM-AFM requires two feedback loops which makes its electronics complex and slow for operation in air or liquids.

Major theoretical and experimental advances concerning AM-AFM are described in Sections 2–4. Amplitude modulation experiments usually involve amplitudes in the 1–100 nm range. The analysis of large oscillation amplitudes is complicated by several factors. The force gradient varies considerably during an oscillation. This introduces non-linear features in the dynamics of the tip motion. Furthermore, dissipative processes such as surface adhesion hysteresis, viscoelasticity or electronic dissipation may also be involved in the tip–surface interaction. The rich phenomenology observed in AM-AFM has generated an intense theoretical activity that has established a solid framework to interpret the experimental observations.

The presence of attractive and repulsive components in the tip–surface interaction force and their non-linear character determines, in many situations of interest, the coexistence of two stable states or oscillations. The dependence of those states on the tip–surface separation generates two oscillation branches, a low and a high oscillation amplitude branch. We show that all the relevant properties of AM-AFM, including resolution, sample deformation and image contrast depend on the oscillation state chosen to operate the microscope. High amplitude states imply tip–sample mechanical contact while, in most cases, low amplitude solutions do not imply mechanical contact. On the other hand, simultaneous topographic and compositional contrast in heterogeneous samples has been achieved by recording the phase angle difference between the external excitation and the tip motion (phase imaging). Because phase shifts are closely related to tip–surface inelastic processes, AM-AFM can be applied for mapping energy dissipation processes at nanometer scale.

Significant although by no means representative applications of AM-AFM for high-resolution imaging of biomolecules and polymers are described in Section 4. Large-scale patterning of silicon surfaces, metallic nanoparticle manipulation or the fabrication of single electron devices by AM-AFM illustrate its potential for device fabrication at nanometer scale. A brief introduction to AM-AFM operation in liquids is also provided.

Section 5 is devoted to frequency modulation. We start with a discussion of the relationship between frequency shifts and tip–surface interactions, that emphasises the ability of perturbation theory, confirmed by detailed numerical simulations including the amplitude feedback, to describe the frequency shift. Ab initio calculations soon revealed that short-range tip–surface interactions were relevant for the atomic resolution in FM-AFM. These results prompted a more thorough consideration of tip preparation and characterisation. A normalised frequency shift which isolates the intrinsic contribution of the tip–surface interaction from the dependence on the operation parameters, can be defined. Simple approximate expressions for this normalised frequency shift in terms of the interaction force and potential are discussed.

Perturbation theory also makes it possible to separate the contribution of long-range (electrical and/or van der Waals) forces to the frequency shift and provides a detailed quantitative comparison between theory and experiment for the short-range chemical contributions that confirms their role in the achievement of true atomic resolution. Special attention is paid to extensive experimental work on semiconductor and insulator (alkali halides and oxides) surfaces, with a brief reference to weakly interacting systems such as graphite or noble gases. The very different nature of the dominant contributions to the tip–surface interaction in all these systems provides further understanding about the role of purely structural and electronic contributions to the contrast observed.

FM-AFM can be used to map the tip–surface interaction. The improved sensitivity and accurate positioning obtained by operation at low temperature (LT) allows the determination of frequency shift versus distance curves above specific sites. This experimental information, combined with the recently developed inversion procedures, has made possible the determination of the interaction potential at those sites. This in turn opens the possibility of using the FM-AFM as a spectroscopic technique, with chemical identification capabilities. The section ends with a discussion of the optimal range of experimental operation parameters, and the use of damping (excitation amplitude) as a source of atomic contrast, with a brief account of the possible interpretation in terms of microscopic dissipation mechanisms.

Finally, in Section 6 we discuss future tendencies and applications of dynamic AFM modes. We also summarise the results of previous sections.

2. Principles of AM-AFM

AM-AFM is a dynamic force microscopy mode where the cantilever-tip ensemble is excited at a fixed frequency, usually near or at the free resonance frequency. The oscillation amplitude is used as a feedback parameter to image the sample topography. In this section the current understanding of AM-AFM is presented. Special emphasis is devoted to address two fundamental questions: (i) Why does the oscillation amplitude of a vibrating tip depends on the tip–surface forces? and (ii) Should the amplitude increase or decrease if the strength of the force is increased?

2.1. From non-contact to tapping AFM imaging

Martin et al. [2] pioneered the use of a force microscope operated in an oscillating mode. They proposed an analytical model that allows for very small vibration amplitudes (say below 1 nm), to connect changes in the oscillation amplitude with variations in the derivative of the force along the normal to the surface. In Wickramasinghe and co-workers experiments, the changes in the amplitude were dominated by long-range attractive forces of van der Waals type. They also suggested the use of the amplitude as the feedback signal for imaging applications. A few years later Zhong et al. [13] reintroduced the use of the amplitude as the signal feedback. They proposed two modifications. First, the cantilever was excited with large oscillation amplitudes up to 100 nm. Second, relatively stiff cantilevers with spring constants of about 40 N/m were also used. It was thought that those values were needed to avoid the trapping of the tip by surface forces. It was also believed that short-range repulsive forces (contact forces) were responsible for the amplitude reduction. Their method was named tapping-mode AFM (or intermittent contact AFM). Since then both approaches have evolved separately. However, in this section it is shown that non-contact and intermittent contact are the fundamental solutions of the equation of motion of a vibrating tip in the proximity of a surface.

2.1.1. Experimental methods to excite the cantilever

Acoustic and magnetic excitation modes have been developed to excite the microcantilever-tip ensemble. In the acoustic excitation mode a piezoelectric actuator is attached below the substrate containing the cantilever-tip ensemble [4,13] (Fig. 1(a)). The application of an oscillating voltage to the actuator produces its vibration and this in turn produces the oscillation of the microcantilever.

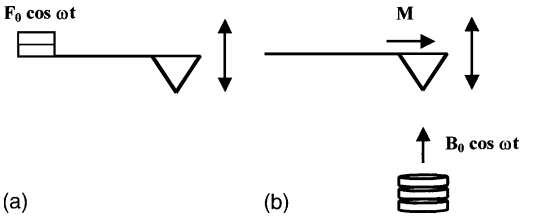

Fig. 1. Schematic depiction of acoustic (a) and magnetic (b) excitation methods in AM-AFM.

This excitation mode is widely used in air and liquids, although in liquids it also excites the fluid. Other authors [14] have directly excited the tip by applying an oscillating magnetic field to a magnetised cantilever (Fig. 1(b)).

2.2. Equation of motion of a vibrating cantilever

A thorough understanding of dynamic AFM operation requires to solve the equation of motion of the cantilever-tip ensemble under the influence of tip–surface forces. A complete rigorous approach is a formidable task that involves the solution of the equation of motion of a three-dimensional object, a vibrating cantilever (Fig. 2). Some symmetry considerations allow to approximate the microcantilever beam by a one-dimensional object, then

$$EI\frac{\partial^4 w(x,t)}{\partial x^4} + \mu\frac{\partial^2 w}{\partial t^2} = F(x,t) \tag{2.1}$$

Here $w(x,t)$ is the transverse displacement of the cantilever beam. E, I and μ are the Young's modulus, moment of inertia and mass per unit of length of the cantilever, respectively. $F(x,t)$ is a term that contains all the forces per unit of length acting on the tip. The above equation implicitly assumes that the tip is a massless object. The difficulties to tackle the above equation can be grasped by following the works of Butt and Jaschke [15], Sader [16] and Stark and Heckl [17].

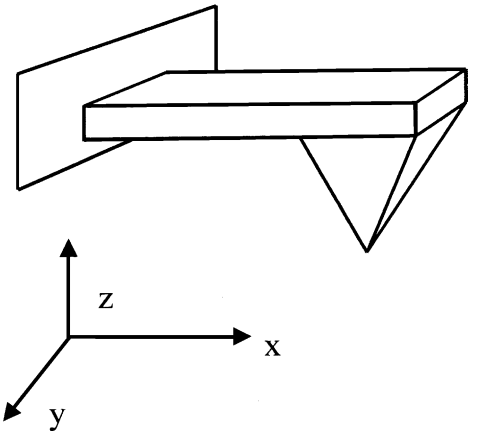

Fig. 2. Three-dimensional representation of the microcantilever-tip system.

To gain some insight into the tip motion, several authors have considered the cantilever-tip ensemble as a point-mass spring, then the tip motion could be approximately described by a non-linear, second-order differential equation [18–32]

$$m\ddot{z} + kz + \frac{m\omega_0}{Q}\dot{z} = F_{ts} + F_0\cos(\omega t) \tag{2.2}$$

where F_0 and ω are the amplitude and angular frequency of the driving force, respectively; Q, ω_0 and k are the quality factor, angular resonance frequency and force constant of the free cantilever, respectively. F_{ts} contains the tip–surface interaction forces. In the absence of tip–surface forces, Eq. (2.2) describes the motion of a forced harmonic oscillator with damping.

2.3. Interaction forces

The forces relevant to AFM are ultimately of electromagnetic origin. However, different intermolecular, surface and macroscopic effects give rise to interactions with distinctive distance dependencies. In the absence of external fields, the dominant forces are van der Waals interactions, short-range repulsive interactions, adhesion and capillary forces.

The introduction of those forces in Eq. (2.2) makes it difficult to find the solution of the tip motion. Several approximations to simulate tip–surface forces have been followed. To further simplify the calculations, Winkler et al. [22] ignored long-range interaction forces. They also considered short-range contact forces described by a harmonic potential. In the other end, Anczykowski et al. [33] used the sophisticated Muller–Yushenko–Derjaguin (MYD) model (see below) to calculate tip–surface interaction forces. In this section, we present an intermediate approach that represents a compromise between a *realistic* description of the tip–surface interaction and reasonable computational times [25]. Sarid et al. [19] and Wang [26] have also used similar approaches.

2.3.1. Long-range attractive interactions

Long-range interactions of van der Waals type arise from electromagnetic field fluctuations that could result from thermal and/or zero-point quantum fluctuations. Field fluctuations are universal which makes van der Waals forces ever-present, independent of the chemical composition of the surfaces or the medium. van der Waals forces are amenable to several theoretical treatments of varying complexity [34,35]. Here we will be concerned with simple approximations for a geometry (sphere-flat) that resembles the tip–surface interface.

Assuming additivity, for a sphere-flat geometry the van der Waals force is

$$F_{ts}(z_c, z) = -\frac{HR}{6d^2} \tag{2.3}$$

where H is the Hamaker constant, R the tip radius, z_c the rest tip–surface separation, z the instantaneous tip position and d the instantaneous tip–surface separation, $d = z_c + z$ (see Fig. 3). For separations $d < a_0$ (a_0 is an intermolecular distance that is introduced to avoid the divergence of Eq. (2.3), [34]), the resulting van der Waals force is identified with the adhesion force derived from one of the models to be presented in the next subsection.

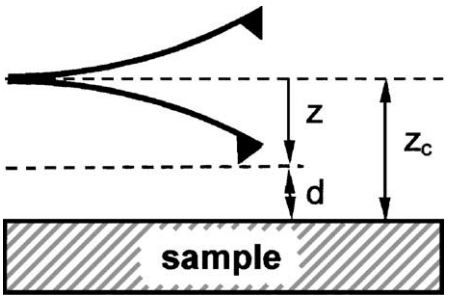

Fig. 3. Scheme of the relevant spatial distances in dAFM. The instantaneous tip–surface separation d, the instantaneous position of the tip z and the average tip–surface separation z_c are plotted. The position of the tip z is defined with respect to the rest position of the tip, positive values and negative values above and below the rest position of the cantilever-tip system, respectively.

2.3.2. *Contact and short-range repulsive forces*

Repulsive forces between atoms or molecules arise from Pauli and ionic repulsion. However, if the contact area between two objects involves tens or hundreds of atoms, the description of the effective repulsive force can be obtained without considering Pauli and ionic repulsion. The surfaces of two bodies are deformed when they are brought into mechanical contact. The deformation depends on the applied load and the properties of the material. Continuum elasticity theories describe the contact and adhesion between finite bodies under an external load. The first model was provided by Hertz in 1881. It described the problem for elastic spheres without adhesion forces. Since then a variety of approximations and models have been developed. Johnson–Kendall–Roberts (JKR) [36] and Derjaguin–Muller–Toporov (DMT) [37] models provide analytical relationships between deformation and applied force. They have become the standard contact models for AFM studies. More sophisticated and self-consistent descriptions of the deformation, stress and interaction between surfaces have been developed by Maugis [38] and Muller et al. [39].

The problem of two elastic objects in contact, here tip and sample, consists in establishing and solving the relationship between the stress (σ) and strain (ε) tensors. This functional relationship is called the constitutive equation. For isotropic materials it is deduced as

$$\sigma_{ij} = \eta\varepsilon_{ll}\delta_{ij} + G\varepsilon_{ij} \tag{2.4}$$

where η is the Lamé coefficient and G the shear modulus ($G = E/2(1+\upsilon)$, where υ is the Poisson's ratio). In equilibrium, the form of the solutions of the above equation can be parameterised by the elasticity parameter, λ ($\lambda = \sigma_0\sqrt[3]{9R/2\pi WE^*}$), where W is the work per unit of area required to fully separate the surfaces and σ_0 is the stress at the equilibrium spacing. The parameter λ compares the relative magnitude of the elastic deformation at pull-off forces and the effective range of the surface force. It can be demonstrated that the general solutions reduce to Hertz for $\lambda = 0$, DMT for $\lambda < 0.1$ and JKR for large λ ($\lambda > 5$). Fig. 4 shows the adhesion map of Greenwood and Johnson [40]. A description of the contact mechanics models and their application to AFM interfaces is discussed by Unertl [41] and Capella and Dietler [42]. A brief description of some of the expressions commonly used to calculate contact and adhesion forces for AFM interfaces follows.

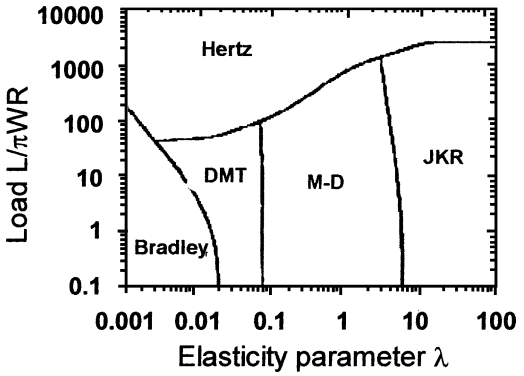

Fig. 4. Normalised load versus elasticity parameter (adhesion map according to Johnson and Greenwood).

2.3.3. DMT adhesion and contact forces

The DMT model [34,37] is suitable for describing stiff contacts with low adhesion forces and small tip radii. The contact force is calculated by

$$F_{\mathrm{DMT}}(z_{\mathrm{c}}, z) = \frac{4E^{*}\sqrt{R}}{3 - 3\upsilon_{\mathrm{s}}^{2}}(a_0 - z - z_{\mathrm{c}})^{3/2}, \quad z_{\mathrm{c}} + z \leq a_0 \tag{2.5}$$

$$\frac{1}{E^{*}} = \frac{1 - \upsilon_{\mathrm{t}}^{2}}{E_{\mathrm{t}}} + \frac{1 - \upsilon_{\mathrm{s}}^{2}}{E_{\mathrm{s}}} \tag{2.6}$$

and the adhesion force is given by

$$F_{\mathrm{a}} = 4\pi R\gamma \tag{2.7}$$

where υ is the Poisson's coefficient and γ the surface energy. The subindices t and s stand for tip and sample, respectively.

2.3.4. JKR adhesion and contact forces

The JKR model should be the choice for contacts characterised by relatively low stiffness, high adhesion forces and large tip radii [34,36]. The adhesion force is calculated by

$$F_{\mathrm{a}} = 3\pi R\gamma = \frac{9}{8}\frac{HR}{6a_0^{2}} \tag{2.8}$$

This model allows to express the penetration as a function of the applied force

$$\bar{\delta} = 3\left(\overline{F_{\mathrm{JKR}}} + 2 + 2\sqrt{1 + \overline{F_{\mathrm{JKR}}}}\right)^{2/3} - 4\left(\overline{F_{\mathrm{JKR}}} + 2 + 2\sqrt{1 + \overline{F_{\mathrm{JKR}}}}\right)^{1/6} \tag{2.9}$$

where $\bar{\delta} = \delta/\delta_{\mathrm{a}}$ and $\overline{F_{\mathrm{JKR}}} = F_{\mathrm{JKR}}/F_{\mathrm{a}}$ are the normalised penetration (indentation) and force, respectively. The parameter δ_{a} is the pull-off separation given by

$$\delta_{\mathrm{a}} = \left(\frac{\pi^{2}R\gamma^{2}}{3E^{*2}}\right)^{1/3} \tag{2.10}$$

2.3.5. Capillary and electrostatic forces

In ambient conditions a thin film of water is adsorbed on hydrophilic surfaces. At close proximity of tip and surface, the separation scales with the Kelvin radius, a meniscus or liquid bridge may be formed between tip and sample. This meniscus implies an attractive (capillary) force that shows a dependence with the distance [43–46].

The trapping of electrostatic charge in dielectric surfaces could give rise to long-range interaction forces. Additionally, in many experimental situations an external electric field is applied between tip and sample [47]. Capillary and/or electrostatic forces may play a dominant role in a given experiment. However, those forces are not needed to describe the general features of AM-AFM. In the following sections we only consider the presence of van der Waals and contact forces as described above. Needless to say that to compare experiment and theory requires the identification and consideration of all the forces acting on the tip.

2.4. Dynamics of a vibrating tip in the proximity of a surface

The aim of this section is to provide the fundamental concepts needed to understand the tip motion in AM-AFM. The description of the tip dynamics is performed for a tip–surface interaction potential with long-range van der Waals forces and contact repulsive forces. Even with simplified assumptions, those forces have power law dependencies on the tip–surface separation. The non-linearity of the interactions has deep implications in the resulting tip motion. It also makes difficult to find analytical solutions.

2.4.1. Harmonic approximations

In the absence of tip–surface forces $F_{ts}(z) = 0$, Eq. (2.2) is the equation of a forced harmonic oscillator with damping. The study of the motion of a harmonic oscillator can be considered as a prerequisite towards the understanding of the complex tip motion in AM-AFM.

Let us start with some qualitative considerations about the asymptotic limits of the oscillation amplitude as a function of the excitation frequency. At low driving frequencies with respect to the free resonance frequency the response is controlled by the stiffness of the spring. The oscillator moves in step with the driving force with an amplitude close to F_0/k. At frequencies very large with respect to the free resonance frequency, the term kz is small compared to (d^2z/dt^2) so the response is controlled by inertia. Then a relatively small oscillation amplitude should be expected with a phase shift of 180°. The acceleration of a harmonic oscillator is 180° out of phase with the displacement.

The solution of a harmonic oscillator with damping can be found in an introductory textbook to the study of vibrations and waves [48]

$$z = B\exp(-\alpha t)\cos(\omega_r t + \beta) + A\cos(\omega t - \phi) \tag{2.11}$$

The solution has a transient term and a steady solution. Initially, both motions are prominent, however, after a time $2Q/\omega_0$, the transient term is reduced by a factor of $1/e$, from then on the motion is dominated by the steady solution. The steady term is a sinusoidal function (harmonic) with a phase lag with respect to the excitation force. The dependence of the amplitude with the excitation frequency can be calculated by the Lorenztian expression

$$A(\omega) = \frac{F_0/m}{\left[(\omega_0^2 - \omega^2)^2 + (\omega\omega_0/Q)^2\right]^{1/2}} \tag{2.12}$$

and the phase shift by

$$\tan\phi = \frac{\omega\omega_0/Q}{\omega_0^2 - \omega^2} \tag{2.13}$$

where ϕ is the angle by which the driving force leads the displacement. The above expressions are simplified by exciting the oscillator at its resonance frequency in absence of damping $\omega = \omega_0$.

$$A_0 = \frac{QF_0}{k} \tag{2.14}$$

The damping modifies the resonance frequency of the cantilever. Resonance and natural (free resonance) frequencies are related by

$$\omega_r = \omega_0\left(1 - \frac{1}{2Q^2}\right)^{1/2} \tag{2.15}$$

Eq. (2.12) shows that the oscillation amplitude depends on the driving force F_0, the hydrodynamic damping and the position of the excitation frequency with respect to the natural frequency.

Let us assume that the tip, i.e., the harmonic oscillator, is under the influence of a parabolic tip–surface interaction potential, then the total force acting on the tip F includes the elastic response kz and the interaction force F_{ts}. For small displacements with respect to the equilibrium position, the total force can be expressed by

$$F = F_0 + \left(\frac{dF}{dz}\right)_{z_0}(z - z_0) \tag{2.16}$$

with

$$k_e = -\frac{dF}{dz} = \left(k - \frac{dF_{ts}}{dz}\right)_{z_0} \tag{2.17}$$

Eq. (2.16) describes the motion of a harmonic oscillator with an effective spring constant given by (2.17), then the new effective resonance frequency is calculated by

$$\omega_e = \left(\frac{k - (dF_{ts}/dz)}{m}\right)^{1/2} \tag{2.18}$$

Eq. (2.18) shows that the resonance frequency of a weakly perturbed harmonic oscillator depends on the gradient of the interaction. A change in the effective resonance frequency implies a whole shift of the resonance curve according to Eq. (2.12) where ω_0 is replaced by ω_e. The dependence of the amplitude on the excitation and effective resonance frequencies introduces a possible mechanism to explain the dependence of the oscillation amplitude with the strength of the interaction force, or in other words, with the tip–surface separation.

Let us assume that the tip is excited at the natural frequency. The approaching of the tip towards the surface will modify the resonance frequency which in turns implies a modification of the oscillation amplitude (Eq. (2.12)). The actual oscillation amplitude will be given by the value of the new resonance curve at the excitation frequency of the oscillator. As a consequence, the new oscillation amplitude would be smaller than the free amplitude (Fig. 5). However, if the excitation frequency was just off

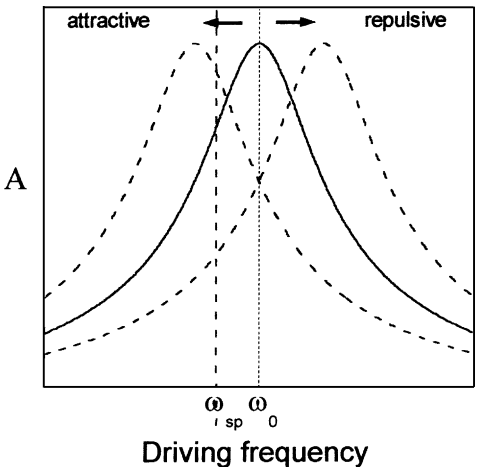

Fig. 5. Resonance curve for a single harmonic oscillator (solid line) and under the influence of attractive and repulsive forces (dashed lines). An external force, its force gradient, produces a shift of the resonance curve (weakly perturbed harmonic oscillator model) without introducing any shape or size modifications.

resonance to the left, the oscillation amplitude could decrease or increase depending on the position of the new resonance frequency with respect to the natural frequency.

The availability of analytical expressions has stimulated the use of models based on weakly perturbed harmonic oscillators to describe AM-AFM [49–52]. Harmonic models are useful to provide some of the concepts that appear in dynamic AFM experiments, however, in most cases they fail to provide quantitative or even semi-quantitative agreement with the experiments. They also lead to misconceptions about AM-AFM operation.

Fig. 6 shows the oscillation amplitude as a function of the excitation frequency for vibrating silicon microcantilever in the proximity of a mica surface for different tip–surface separations (12, 6 and 5 nm). For relatively large separations ($z_c = 12$ nm) the resonance curve coincides with the resonance curve of the free cantilever. Resonance curves in AM-AFM experiments ($z_c = 5$ and 6 nm) show a considerable depart from a Lorentzian curve. Long-range attractive forces introduce a considerable bend and distortion of the resonance curve. Furthermore, experimental resonance curves in AM-AFM do not show the frequency shift predicted by the harmonic approximation.

The limitations of harmonic models to describe dynamic AFM can be traced back to the implicit assumptions used to derive Eqs. (2.16)–(2.18). First it was assumed that tip–surface forces induce a frequency shift and not energy transfer. Second, the force gradient was assumed independent of the separation. Third, the force gradient was smaller than the cantilever force constant $\dot{F}_{ts} \ll k$. However, most experiments imply oscillation amplitudes above 5 nm which violate at least one of the above assumptions. A quantitative discussion on the limitations of the harmonic approach to interpret dynamic AFM experiments is provided by Hölscher et al. [53].

2.4.2. *Coexistence of two stable oscillation states*

From a fundamental point of view, the participation of attractive and repulsive tip–surface interactions and their non-linear character gives rise to one of the most exciting properties of AM-AFM, the coexistence of two stable oscillation states [25,30,56,57]. Furthermore, for some extreme conditions

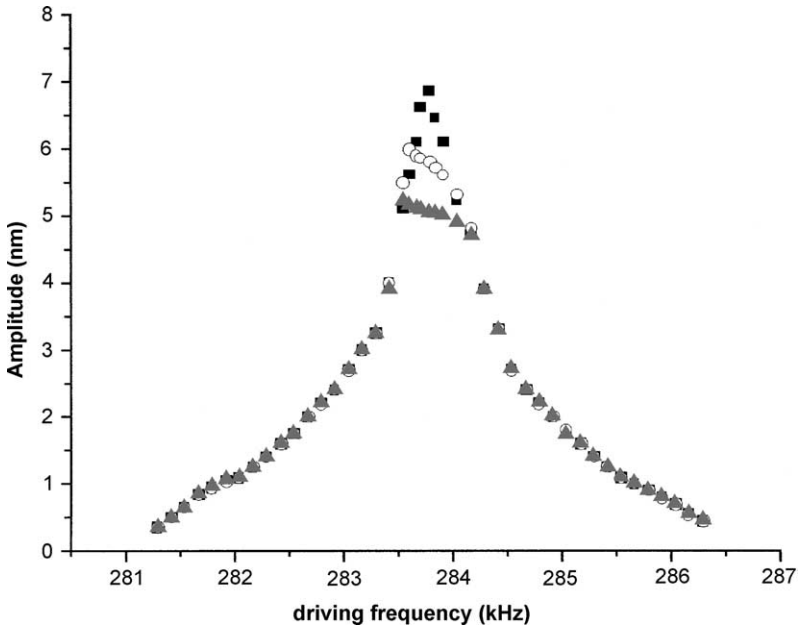

Fig. 6. Experimental resonance curves for three different tip–surface separations ($z_c = 5$, 6 and 10 nm). At relatively large tip–surface separations with respect to the free oscillation amplitude ($z_c = 12$ nm), the resonance curve coincides with the free resonance curve. At closer separations, tip–surface forces modify dramatically the resonance curve. The curve appears truncated at the centre. We note that this experiment was performed in such a way that there was not tip–sample mechanical contact, i.e., the forces were exclusively LR attractive forces. The experiment was performed in air with a silicon cantilever and a mica sample. Solid symbols $z_c = 12$ nm, circles, $z_c = 6$ nm and triangles $z_c = 5$ nm. Frequency sweep from low to high frequencies.

such as when small rest tip–surface separations are used and relatively large free oscillation amplitudes more than two steady-state solutions [59] or even chaotic solutions [60,61] can be found. Nevertheless, those extreme situations are far from the standard operational parameters and unsuitable for imaging. They are not considered in this report.

Gleyces et al. [54] were the first to describe non-linear dynamic effects in scanning probe microscopy experiments. They measured the oscillation amplitude as a function of the excitation frequency for an STM tip vibrating in the proximity of a surface. They observed that for some frequencies two different values of the amplitude could be obtained. Anczykowski et al. [20] invoked bi-stability to explain hysteresis effects in amplitude versus distance curves. On the other hand, Aimé and co-workers [55] proposed a non-linear dynamics analysis to explain the dependence of the hysteresis on the strength of the attractive interaction. Furthermore, the contributions of García and San Paulo [25,56,57], Wang [26], Nony et al. [28] and Marth et al. [30] have emphasised the intrinsic non-linear character of the tip motion in AM-AFM.

The oscillation amplitude A is the key experimental parameter measured in AM-AFM. Its representation as a function of the average tip–surface separation, called amplitude curve, clarifies the operation in AM-AFM. The numerical solution of Eq. (2.2) shows that in some situations the tip has two different solutions, a low (L) and high amplitude (H) solution, $Z_{H(L)} = Z_0 + A_{H(L)} \cos(\omega t - \phi_{H(L)})$.

Both of them have the same period than the external excitation. If the rest tip–surface separation and the external parameters ω, F_0, remain unchanged, the initial conditions (z, dz/dt, ωt) will determine which solution or state is reached.

The dependence of the low and high oscillation solutions on the rest of the tip–surface separation for a system characterised by R, A_0, $f_0 = f$, k, Q, H, γ and E^* of 20 nm, 10 nm, 350 kHz, 40 N/m, 400, 6.4×10^{-20} J, 30 mJ/m^2 and 1.51 GPa, respectively, are plotted in Fig. 7(a). The collection of L and H solutions gives rise to the L and H branches, respectively. In both branches the amplitude decreases almost linearly with decreasing the separation. The coexistence of two branches illustrates an ambiguity in the operation of an AM-AFM. Both branches could provide a value of the amplitude that matches the feedback amplitude A_{sp}. The discussion of the results of Fig. 7(b) and (c) is postponed to Section 2.4.5.

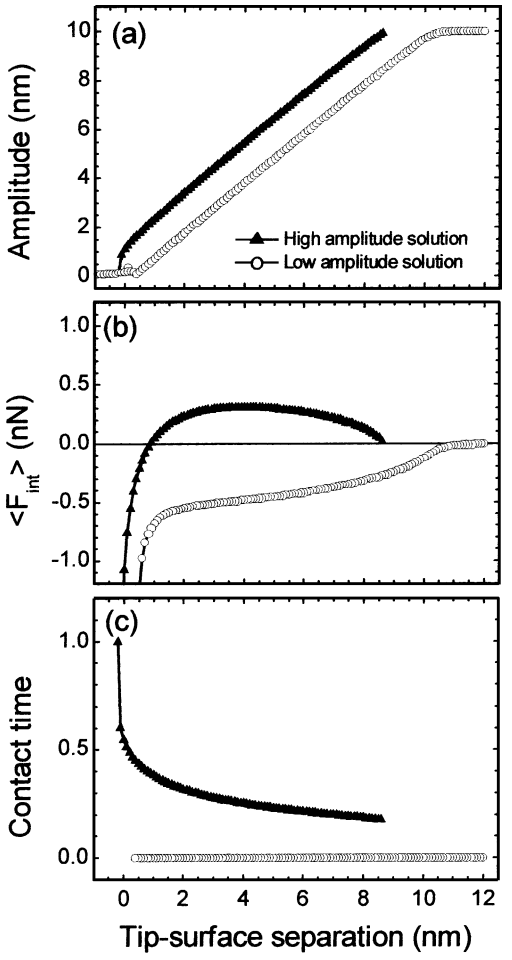

Fig. 7. (a) Amplitude, (b) average force and (c) contact time as a function of the (rest) tip–surface separation. The coexistence of two solutions for different tip–surface separations gives rise to the formation of branches. There are two relevant observations for the case simulated here. The average force in the H branch changes from positive to negative at very small separations. There is not tip–surface mechanical contact in the L branch.

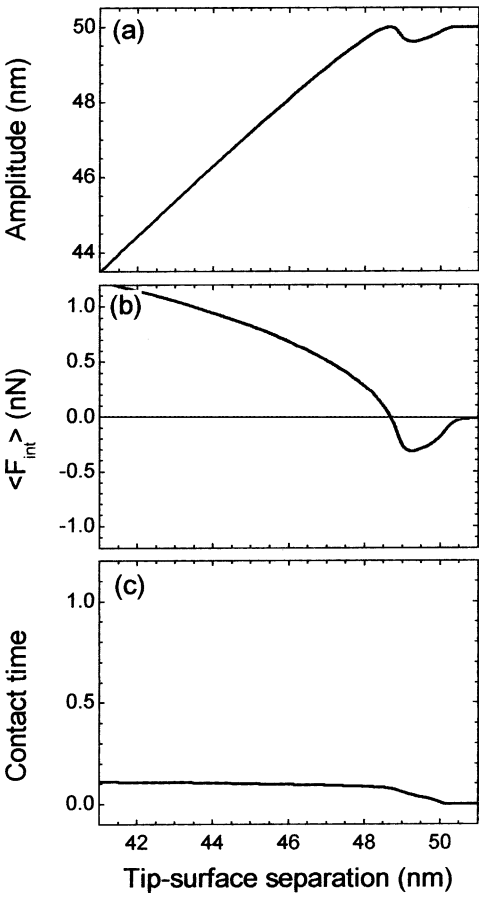

Fig. 8. (a) Amplitude, (b) average force and (c) contact time curves for large driving forces ($A_0 = 50$ nm). A single branch is observed. It shows a continuous transition from attractive to repulsive interaction regimes. Adapted from [65].

The coexistence of two oscillation states depends on sample properties such as the sample's elastic modulus or the adhesion force, non-conservative interactions as well as on operational parameters such as the free oscillation amplitude or the cantilever force constant [57,58]. In general, the compliance of the sample or the use of large driving forces reduce the occurrence of two stable states. For example, if the free oscillation amplitude is increased, the region of coexistence of both solutions is fractured and squeezed [57]. A gap is observed in the low amplitude branch. The gap grows wider as the driving force is increased. Eventually, both branches merge into a single branch, i.e., for each tip–surface separation there is only one possible stable solution. This situation is illustrated in Fig. 8(a) where the amplitude curve is single branched. The curve has been calculated by using the same parameters as in Fig. 7 but the free amplitude of 50 nm in this case.

2.4.3. Non-linear dynamics: phase space diagrams

The representation of the tip's final state as a function of the initial velocity and position, *phase space diagram*, is a very useful tool to understand the interplay between the high and low amplitude states and

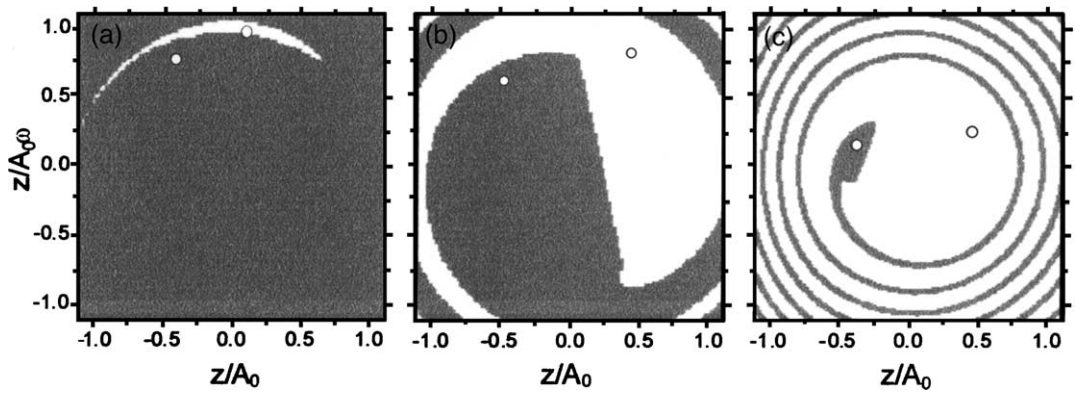

Fig. 9. Two-dimensional phase space projection for different tip–surface separations. The tip evolves from a phase space dominated by the basin of the low amplitude solution at $z_c = 16$ nm (a), to a phase space with a balanced distribution of both basins of attraction at $z_c = 14.5$ nm (b); at $z_c = 7.5$ nm the phase space is dominated by the basin of the high amplitude solution (c). The open circles indicate the Poincaré sections of the H and L solutions. A_0 is the free oscillation amplitude (adapted from [56]).

its consequences in the operation of AM-AFM. Phase space diagrams are standard and unavoidable representations to describe the dynamics of non-linear systems [62]. Those representations were introduced by Marth et al. [30] and García and San Paulo [56] in the context of AFM imaging.

Fig. 9 shows three snapshots taken at $t = 0$ of the phase space projection for different rest tip–surface separations. The numerical simulations were performed for R, A_0, f_0, k, Q, H, E^* and F_0 of 30 nm, 18 nm, 350 kHz, 40 N/m, 400, 6.4×10^{-20} J, 1.51 GPa and 1.8 nN, respectively. The phase space is divided in two inter-locking regions. Initial conditions that give rise to the L state are plotted in grey, while those that give rise to the H state are plotted in white. A rotation of an angle ωt about the origin generates the phase space projection for a different time t. The Poincaré sections of H and L states are represented by circles.

For $z_c = 16$ nm the basin of attraction of the low amplitude state dominates the phase space projection. At $z_c = 14.5$ nm the phase space is almost equally distributed between L and H basins of attraction, 52 and 48%, respectively. However, at $z_c = 7.5$ nm, the H basin of attraction amounts about 95% of the phase space projection. In the range of separations studied here 6–18 nm we find that the dependence of the phase space on the tip–surface separation can be divided in to three regions. For z_c separations close the value of the free amplitude, the phase space is dominated by the basin of attraction of the L state. Then there is an intermediate region where the phase space is roughly equally distributed between both basins of attraction. For z_c in the interval (6–12) nm the phase space is dominated by the basin of attraction of the H state. However, the relative extension of H and L regions depends on several factors such as the free amplitude, sample mechanical properties, dielectric constants, surface free energy and tip's radius [56,57].

Phase space diagrams are very useful to understand and predict the tip behaviour in AM-AFM. For a given tip–surface separation, the tip should oscillate in the state with the largest basin of attraction. Whenever there is an asymmetric distribution of the phase space between basins of attractions such as the ones depicted in Fig. 9(a) and (c) a stable operation of the microscope should be expected. On the other hand, H and L transitions are likely to happen for a phase space diagram like the one depicted in Fig. 9(b).

Those transitions could complicate the acquisition and interpretation of a topographic image. However, the use of phase diagrams to describe the tip motion has a subtle caveat. The deterministic character of the equation of motion implies that if the tip is placed, say in the H state depicted in Fig. 9(a), it should remain indefinitely there with independence of the smallness of its basin of attraction. This objection, however, is removed by realising that in any experiment there is *noise*. The noise is originated by the presence of mechanical, electronic, thermal or feedback perturbations. Those perturbations, in particular *feedback* perturbations which are always present in AFM may limit the accessibility of the state with the smallest basin of attraction.

Feedback or *intrinsic* perturbations are due to the finite time response of the feedback electronics in AM-AFM, usually in the 10^{-4} s range. This implies that if the tip is laterally displaced at a speed of 10 μm/s, a topographic feature of arbitrary height (or depth) with a side slope of 60° would produce a maximum change of the rest tip–surface separation Δz_c of approx. ± 1.7 nm before the feedback takes over. The actual process of how the tip evolves from one state to the other once a perturbation has occurred is rather involved. The perturbation will be followed by a transient and after that the tip will reach a stable (intermediate) oscillation. From there the feedback will smoothly re-establish the A_{sp} value. An AM-AFM will be operating properly if the intermediate and initial (unperturbed) states belong to the same branch, otherwise instabilities and image artefacts should appear. Numerical simulations show that for the situation shown in Fig. 9(a) a perturbation in the tip–surface distance of $+0.1$ nm would move the tip from H to L. The converse transition requires a perturbation of -1.6 nm. For Fig. 9(b), however, the transition from H to L requires a perturbation of $+1.4$ nm, which coincides with the value needed to go from L to H. The H state in Fig. 9(c) is very robust. A sudden decrease (increase) of -3.5 nm ($+7.5$ nm) in the tip–surface separation is required to produce the transition. A detailed discussion on the role of perturbations in the operation of an AM-AFM is given in [56].

2.4.4. *Implications of the coexistence of stable states*

Several experimental observations provide evidence of a bi-stable tip motion in AFM. Steplike discontinuities in amplitude curves have been reported on SiO_x [20,63], GaAs [56], polystyrene [58] and mica samples [65]. Those discontinuities have a straightforward interpretation in terms of the coexistence of two stable states. Each discontinuity is a transition between L and H states or viceversa. We note that it is not possible to obtain experimental amplitude curves such as the theoretical curves depicted in Fig. 7(a), i.e., with both branches side by side. Because no matter how many oscillation states are available, at a given instant only one state can be explored.

Fig. 10 shows an experimental amplitude curve obtained on a mica surface. The amplitude is measured while the tip is approached towards and then retracted from the surface. A hysteresis loop is observed in the central section of the curve. The hysteresis is also explained by the simulations presented previously. The loop requires the presence of two transitions at different tip–surface separations. An L–H transition while approaching the tip towards the sample (A) and an H–L transition while withdrawing the tip (B). At relatively large tip–surface separations, always smaller than the free oscillation amplitude, the tip should oscillate in a state belonging to the L branch. At those separations the basin of attraction of L states are considerably larger than those corresponding to H states. Approaching the tip towards the surface changes the relative size of the basin of attractions until eventually the basin of attraction of the states belonging to the H branch dominate the phase space. At those separations a transition from the L to H branch should be expected. From then on the tip should

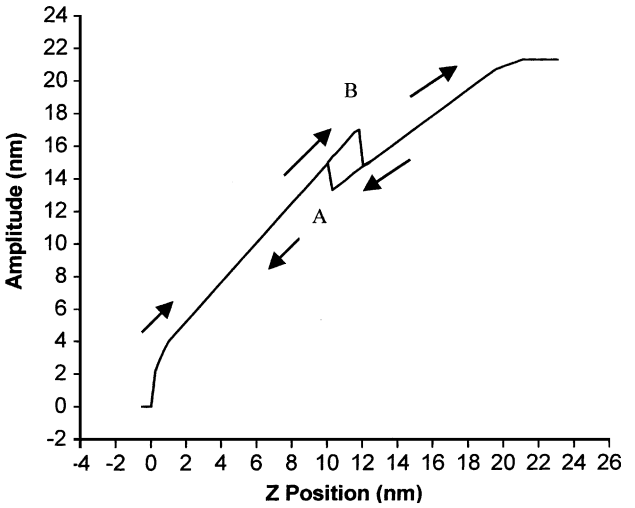

Fig. 10. Amplitude curve (approach and retraction sections) taken on a mica sample. Partial sections of the H and L branches are observed. The presence of two transitions between L and H states give rise to the formation of an hysteresis loop.

oscillated in the H branch. In the retraction part of the curve the tip first oscillates in the H branch because at those separations the phase space diagram is dominated by the basin of attraction of H states. Increasing the separation from the surface increases the basin of attraction of the states belonging to the L branch until eventually it equals and overcomes to the one of H states. At those separations a transition should be expected.

Hysteresis loops are highly reproducible for a given system, however, the points at which a transition happens (A or B) may change from curve to curve. The transition represents a competition among three factors, the phase space distribution between the basin of attractions, the deterministic character of the equation of motion and the presence of perturbations. The deterministic character of the equation of motion explains the tendency of the tip to remain in the branch corresponding to the preceding separation. This is illustrated by the observation, that in general, the transition point (A) in the approaching part of the curve is closer to the surface than the transition point (B) of the retracting curve. A perturbation is needed to break determinism and have a transition. However, a perturbation will be more effective, in terms of producing a transition, whenever the basin of attraction of the final state is larger or at least of the same size than the one of the initial state. The slight changes observed on the loop size whenever multiple amplitude curves are recorded is a consequence of the random nature of the occurrence of a perturbation.

The simultaneous existence of two oscillation states and the randomness of perturbations also suggests amplitude curves with multiple steplike discontinuities. For example, initially the tip could oscillate in the low amplitude state. By reducing the tip–surface separation a transition to the high oscillation state could be observed. Then, reducing the distance even more could produce a transition back to the low amplitude branch. Imaging thin polyvinyl alcohol films, Haugstad and Jones [66] found the existence of double transitions. Higher order transitions are also possible although unlikely.

The coexistence of two stable states has strong implications for the operation of a sophisticated instrument such as the tapping-mode AFM. Fig. 11(a) shows an experimental amplitude curve taken on a GaAs(1 0 0) substrate [56]. The presence of a steplike transition between the H and L branches shows

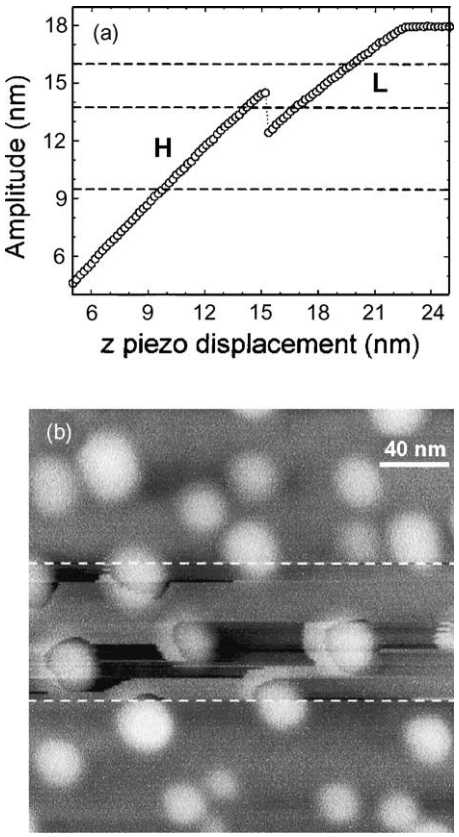

Fig. 11. Experimental determination of the low and high amplitude branches. (a) Amplitude curve, the L and H branches are plotted by open circles. Dashed lines indicate the A_{sp} values used to image a 200×200 nm^2 InAs quantum dot sample. (b) The system evolves from stable imaging in the L state $A_{sp} = 16$ nm (top) to unstable imaging due to switching between H and L states $A_{sp} = 13.8$ nm (middle) and finally to stable imaging in the H state $A_{sp} = 9.5$ nm (bottom). Adapted from [56].

that an A_{sp} value within the step range could be achieved with two different tip–surface separations. This open three possibilities for imaging. Imaging in either the H or L state or imaging with a tip motion characterised by switching between them. The latter implies the switching between one z_c position to the other. This would introduce some height variations unrelated to the topography of the surface which in turn would complicate height measurements. An illustration of the *spontaneous* switching between L and H amplitude states is provided by imaging at $A_{sp} = 13.8$ nm in Fig. 11(b). In the central region, the quantum dots appear surrounded by fringes. Those features represent a tip switching between H and L states. For such a A_{sp} value imaging exclusively in the H or L state although physically possible is, in practice, unlikely because of the existence of feedback perturbations.

Fig. 11 also illustrates that a suitable choice of set point amplitudes allows stable imaging in both states. At $A_{sp} = 16$ nm a stable image of the quantum dots is obtained in the L branch while the same happens by operating the instrument in the H branch with a set point amplitude of $A_{sp} = 9.5$ nm.

It is an established practice in probe microscopy to attribute noisy or *unstable* data to a contaminated tip or a changing tip shape. However, the above example shows that in some cases noisy or unstable

data only reflects the intrinsic structure of the tip motion. It also explains the manipulation of the observer with the driving frequency or set point amplitude as a process that modifies the tip's phase space to reach a configuration where a single basin of attraction dominates the phase space projection.

Phase space diagrams does not tell the whole story about either the physical properties of L and H amplitude solutions or their implications for AFM imaging. For example, does resolution depend on the oscillation state? or more generally, Are low and high amplitude solutions equivalent for imaging purposes?

Some biomolecules are excellent systems to test the imaging advantages and/or limitations of different scanning probe microscopy methods [7,67,68]. High-resolution imaging of antibodies has shown that resolution and sample deformation are highly dependent on the oscillation state selected to operate the instrument [7]. The morphology and dimensions of the fragments that form antibodies were clearly visible in the image obtained by using the L state (Fig. 12(A)), while the image obtained in the H state shows a jagged topography with no clear evidence of the domain structure (Fig. 12(B)). Furthermore, the hinge regions connecting the Fc fragment with the Fab arms are clearly resolved in Fig. 12(A).

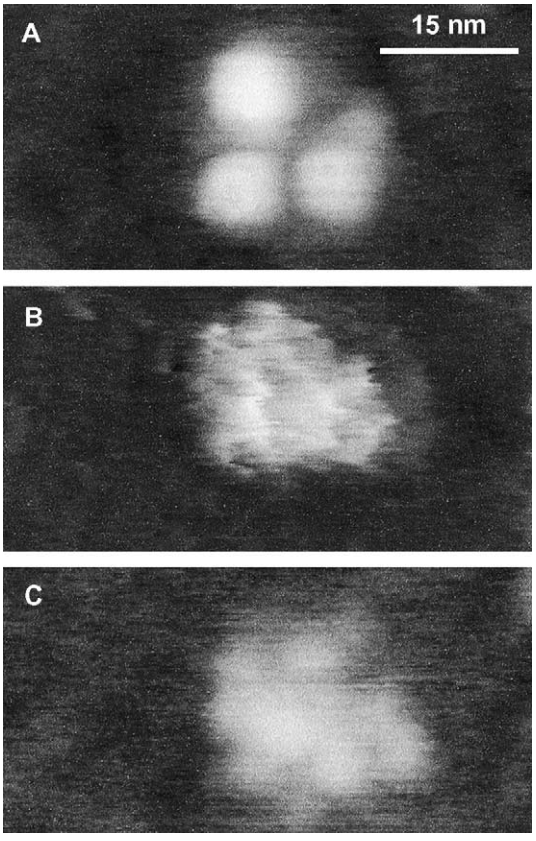

Fig. 12. (A) High-resolution image of a single a-HSA (obtained by operating in an L state). The three fragments and the hinge regions are clearly resolved. (B) Image of the same molecule obtained by operating the instrument in an H state. (C) Image of the molecule in the initial L state after repeated imaging in an H state. The characteristic shape of the molecule has been lost by imaging in an H state. Adapted from [7].

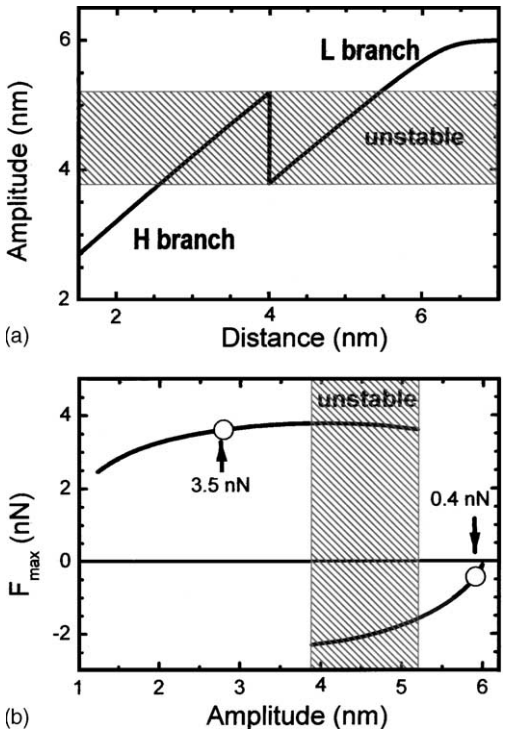

Fig. 13. (a) Theoretical amplitude curve. The shadowed region indicates the values of the oscillation amplitude that produce an unstable behaviour. (b) Calculated maximum force dependence on the oscillation amplitude. The arrows indicate the values of the experimental set point amplitudes used for recording the images in Fig. 11. Adapted from [7].

It was also demonstrated that imaging in the H state produced irreversible morphological modifications in the antibody (Fig. 12(C)).

Theoretical simulations [7] revealed two major physical differences between H and L oscillation states used in the above experiments. The existence of tip–sample contact in the H state and the maximum force exerted by the tip which also was about one order of magnitude higher in the H state (3.5 and 0.4 nN, respectively, Fig. 13). Those factors explained the enhanced resolution obtained by using an L oscillation state to image antibodies. The shaded area in Fig. 13 represents the values of set point amplitudes unsuitable for imaging because the presence of multiple H and L transitions produces an unstable tip motion.

2.4.5. Attractive and repulsive tip–surface interaction regimes

To advance in the understanding of the physical properties of L and H amplitude states we first introduce two new parameters, the contact time, i.e., the time that the tip is in mechanical (repulsive) contact with the surface and the average value of tip–surface forces. Those quantities can be easily calculated by numerical simulations although pose considerable difficulties for their experimental evaluation [69]. The average force per period is calculated by

$$\langle F_{\mathrm{ts}} \rangle = \frac{1}{T} \oint F_{\mathrm{ts}} \, \mathrm{d}t \tag{2.19}$$

Fig. 7 shows the amplitude curve, average force and contact time for a system characterised by R, A_0, $f_0 = f$, k, Q, H, γ and E^* of 20 nm, 10 nm, 350 kHz, 40 N/m, 400, 6.4×10^{-20} J, 30 mJ/m^2 and 1.51 GPa, respectively [25,26]. There are several relevant observations. The average force in the low amplitude branch is negative, i.e., attractive. It also shows a correlation between the strength of the interaction and the amplitude reduction. Increasing the force strength increases the amplitude reduction. On the other hand, the average force in the high amplitude branch is positive (repulsive) except for small oscillation amplitudes where it becomes negative (Fig. 7(b)). For the case calculated here, the low amplitude branch does not imply tip–surface contact while there is a finite tip–surface contact in the high amplitude branch (Fig. 7(c)). These observations seem to give support to the proposal of the existence of two distinct operating regimes in AM-AFM, *attractive* and *repulsive* tip–surface interaction regimes [20,25,28,63,64]. García and San Paulo [25] proposed a definition of those regimes in terms of average forces. In the attractive regime, the tip–sample force averaged in one oscillation is negative while in the repulsive regime, the average force is positive. Previously, Anczykowski et al. [20], Kühle et al. [63] and Nony et al. [28] assumed that the attractive regime was given exclusively by long-range attractive forces. However, this more restrictive definition could not account for a situation like the one depicted in Fig. 8(b) where the average force curve shows a region of negative values (attractive) with a minimum value which is indicative of a competition between attractive and repulsive interactions acting on the tip. Furthermore, Fig. 8(c) shows a finite contact time during the attractive regime ($t_c \sim 0.1T$).

At first glance it may seem straightforward to relate the attractive and repulsive regimes to the coexistence of L and H branches, respectively. However, a close attention to some of the features observed in the H branch challenges the above equivalence. The average force dependence on the separation first shows an increase until a maximum is reached, then the average force decreases and changes sign for very small tip–surface separations (Fig. 7(b)). In this example the H branch has a section dominated by repulsive forces and another section, albeit rather small, dominated by attractive forces. Remarkably, the amplitude seems unaffected by those changes because it decreases monotonously with the separation.

The above discussion shows that a description of AM-AFM operation in terms of attractive and repulsive interaction regimes, although intuitively appealing, is imprecise and in some cases inappropriate.

2.4.6. *Analytical descriptions of AM-AFM*

Numerical simulations have been decisive to determine amplitude–distance curves, sample deformations, average tip–surface forces, contact times and to describe the existence of several oscillation states. They have also been useful to understand the sources of an unstable tip motion. However, they fail to provide a comprehensive view of the physical factors governing the tip motion in AM-AFM. In the previous section we have already discussed some examples where the amplitude reduction did not show any correlation with the average value of the force.

Despite the mathematical difficulties involved in solving analytically the equation of motion for non-linear tip–surface forces, several analytical or semi-analytical approaches have been developed to shed some light into the physical parameters governing the amplitude reduction [26–28,70]. Aimé and co-workers [28] have used a variational approach based on the principle of least action to obtain a relationship between the separation and the oscillation amplitude. They investigated three different situations with respect to the tip–surface forces, a pure attractive interaction, a pure repulsive

interaction and the mixing of the two. They obtained that the dynamics of the tip were governed by the product of the quality factor and a reduced stiffness (κ), $Q\kappa$. The reduced stiffness depends on the character of the interaction. For a pure attractive interaction the reduced stiffness is the ratio of an attractive stiffness and the cantilever one ($\kappa_a = HR/kA_0^3$). For a pure repulsive interaction, they assumed a repulsive force with a harmonic form of the type, $(1/2)k_s(z(t) - z_c)^2$, the reduced stiffness is the ratio between the contact stiffness and the cantilever one ($\kappa_r = k_s/k$). In all cases the functional relationship between amplitude and distance are rather complex. For an interaction with repulsive and attractive components, they have deduced

$$\frac{z_c}{A_0} = a\left\{1 - \left(\frac{C}{a}\right)^{2/3}\right\} \tag{2.20}$$

C is calculated by

$$C = \frac{3\pi}{4\sqrt{2}Q\kappa_s}\left[Qa(u^2-1) + \sqrt{1-(ua)^2} + \frac{Q\kappa_a}{6\sqrt{2a}d_0^{3/2}}\right] \tag{2.21}$$

where $a = A/A_0$, $d_c = 0.165\,\text{nm}/A_0$ and $u = \omega/\omega_0$ are the reduced amplitude and frequency respectively.

Wang [26,27] has assumed a sinusoidal oscillation $z = A\cos(\omega t - \phi) = A\cos\theta$ and applied the Krylov–Bogoliubov–Mitroposky asymptotic approximation. He deduced the following relationships for the amplitude and phase shift

$$A = \frac{F_0/k}{(1+\varpi)\sqrt{\alpha_e^2 + (\varpi - \varpi_e)^2}} \tag{2.22}$$

$$\tan\phi = \frac{\varpi_e - \varpi}{\alpha_e} \tag{2.23}$$

where

$$\alpha_e = \alpha_0 + \frac{2}{\pi}\int_0^{\theta_0} \alpha_s \sin^2(\theta)\,d\theta \tag{2.24}$$

$$\varpi_e^2 = 1 + \frac{1}{\pi kA}\int_0^{\theta_0} F_{ts}[A\cos\theta]\cos\theta\,d\theta \tag{2.25}$$

where θ_0 is determined from the contact position

$$\cos\theta_0 = \frac{z_c + a_0}{A} \tag{2.26}$$

where α_0 is the hydrodynamic damping ($1/2Q$) and α_e the effective damping due to hydrodynamic forces with the medium and inelastic interactions in the sample (α_s). ϖ and ϖ_e are the normalised driving frequency (ω/ω_0) and effective (also normalised) resonance frequency. Eq. (2.22) resembles the Lorentzian expression for a forced harmonic oscillator with damping. It says that in the absence of tip–surface inelastic interactions, the variations of the oscillation amplitude are related to changes of the

effective resonance frequency of the system. The changes of the effective resonance are induced by the tip–surface interaction forces as it is shown in Eq. (2.25).

A different approach has been proposed by San Paulo and García [70]. They have applied the virial theorem $\langle K\rangle = -\frac{1}{2}\langle Fz\rangle$ and the consideration that in the steady-state the average rate at which energy is supplied to the tip must be equal to the average rate at which energy is dissipated by hydrodynamic and tip–surface forces. Those assumptions have allowed to derive a general relationship for the oscillation amplitude

$$A \approx \frac{A_0}{\sqrt{2}}\left(1 - \frac{2P_{ts}}{P_{med}} \pm \sqrt{1 - \frac{4P_{ts}}{P_{med}} - 16\left(\frac{\langle F_{ts}z\rangle}{F_0A_0}\right)^2}\right)^{1/2} \tag{2.27}$$

where P_{ts} and P_{med} are the average dissipated power in a cycle by tip–surface and hydrodynamic forces, respectively. For conservative interactions ($P_{ts} = 0$) or negligible tip–surface power dissipation ($P_{ts} \ll P_{med}$), Eq. (2.27) gives

$$A \approx \frac{A_0}{\sqrt{2}}\left(1 \pm \sqrt{1 - 16\left(\frac{\langle F_{ts}z\rangle}{F_0A_0}\right)^2}\right)^{1/2} \tag{2.28}$$

which still can be further simplified by considering that in many cases of interest, attractive and repulsive forces take only significant values near the lower turning point of the oscillation, then $\langle F_{ts}z\rangle \approx -A\langle F_{ts}\rangle$

$$A \approx A_0\left(1 - 4\left(\frac{\langle F_{ts}\rangle}{F_0}\right)^2\right)^{1/2} \tag{2.29}$$

Eq. (2.27) is general in the sense that it does not place any restrictions on the tip–surface forces. It states that the average interaction force times the deflection and the average power dissipated by the tip–sample forces are the quantities that control the amplitude reduction. The dependence on average quantities is a direct consequence of a tip motion that experiences different values of the tip–surface force per cycle. Specifically, the dependence of the amplitude on $\langle F_{ts}z\rangle$ explains the failure to generalise the correspondence between attractive and repulsive interaction regimes and L and H branches.

On the other hand, Eq. (2.29) shows that for some special conditions, albeit not extraordinary from an experimental point of view, the oscillation amplitude decreases by increasing the absolute value of the average value of the interaction force, i.e., in those cases the amplitude depends exclusively on the strength of the force. Because the average value of the interaction force usually increases by decreasing the separation, the amplitude will decrease with the tip–surface separation. A special situation may arise when attractive and repulsive forces cancel each other as it is shown in Fig. 7(b). Then for a small range of tip–surface separations the amplitude may increase as the separation is reduced. It may even reach the free oscillation value in the absence of inelastic tip–surface interactions.

2.4.7. Point-mass springs versus continuous microcantilevers

The theoretical results presented above were based on the solution of Eq. (2.2), i.e., by assuming that the cantilever-tip dynamics could be described by the equation of motion of a point-mass particle. This is undoubtedly a strong assumption that deserves some assessment. Rodríguez and García [71] have

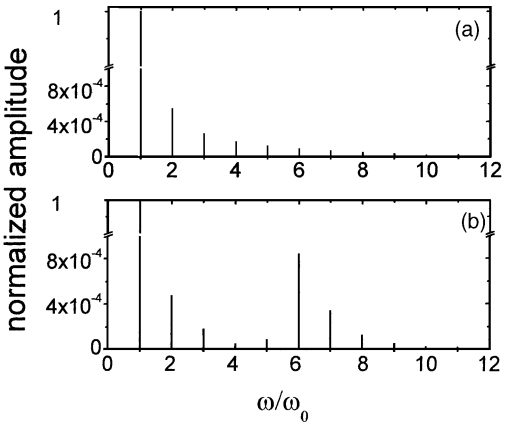

Fig. 14. Spectra of the oscillation signal for a point-mass microcantilever operated in an H state (a) and for a continuous microcantilever beam (b). The amplitude is normalised to the value of the first mode of the cantilever. Adapted from [71].

performed a comparative analysis of the dynamics of a cantilever beam and a point-mass spring described by Eqs. (2.1) and (2.2), respectively. Their study was focused on the relative strength of high order frequency components with respect to the fundamental frequency (excitation frequency). Those components are excited by tip–surface forces [17]. They are modulated by the presence of several oscillation modes in a continuous microcantilever beam or are simply higher harmonics of the excitation frequency in a point-mass model.

Fig. 14 shows the spectra of the oscillation signal calculated for point-mass and continuous models. The dimensions of the beam, the driving force and the hydrodynamic damping are established in such a way that the resonance curve for the first mode is fitted to the Lorentzian curve of a single harmonic oscillator with R, f_0, k, A_0 and Q of 30 nm, 350 kHz, 40 N/m, 18 nm and 400, respectively. Those values represent some of the most common cases for tapping-mode cantilevers and also the optimum conditions to minimise tip–sample damage while maximising resolution in stiff materials. A monotonous decay is observed for the point-mass model while the contributions in the continuous model are modulated by the eigenmodes of the cantilever. Whenever a higher harmonic is close or coincide with an eigenmode of the cantilever an increase of the corresponding frequency component should be expected. However, in both cases the fundamental peak is about 1000 times higher that the second highest peak. This type of analysis allows to conclude that for recommended operation conditions in air, i.e., free oscillation amplitudes below 30 nm, set point amplitude ratios (A_{sp}/A_0) of 0.9–0.4 and $Q \in [50-1000]$ point-mass models give a precise description of the tip motion [71].

2.5. Lateral and vertical resolution

A figure of merit of any microscopic technique is its resolution. An AFM generates three-dimensional images of the sample surface. As a consequence two different, although not always independent, resolutions should be distinguished, *lateral* and *vertical*. Vertical resolution is limited by both noise from the detection system and thermal fluctuations of the cantilever. In general, the thermal noise of the cantilever is the largest source of noise in AFM. Damping systems have become so effective that mechanical vibrations represent a negligible perturbation of the cantilever oscillation.

If the oscillation amplitude is measured with an optical deflection system the thermal noise is calculated by [15]

$$z = \sqrt{\frac{4k_B T}{3k}} = \frac{0.074\,\text{nm}}{\sqrt{k}} \tag{2.30}$$

where the cantilever force constant is in N/m and $T = 295$ K. For a cantilever with a force constant of 40 N/m, the thermal fluctuations of the cantilever are below 0.01 nm. The above values and the experimental observation that amplitude curves show slopes in the 1.2–0.7 range allows AM-AFM to obtain images with a vertical resolution of 0.1 nm or better.

Image formation in AFM has a non-linear character due to the multiple interacting regions between tip and sample. This makes hard to find a generally accepted definition of lateral resolution. As a guide we will adopt the rather intuitive approach of considering that it is the resolution with respect to the object what matters and not only the actual instrumental resolution. The instrumental resolution is defined by the ratio between size and number of pixels of the image. In general, lateral resolution in AM-AFM depends on tip size, tip–surface separation, tip–surface force and sample's compliance. Near true atomic resolution by AM-AFM has been obtained by Ohnesorge [72] on a flat crystalline sample. Atomic periodicities of about 0.5 nm and atomic steps were imaged in a calcite surface immersed in water.

The fine tip size is responsible for the broadening effects observed in most AFM images. AFM measurements always tend to overestimate lateral dimensions of tree dimensional objects. Fig. 15 shows a typical AM-AFM image obtained in air of a DNA fragment. The DNA molecule appears as filament structure on the flat substrate. The apparent width of the molecule at its base is about 17 nm while its value at half maximum is 11 nm. In any case those values are about 5–9 times larger than nominal value (∼2 nm in diameter). A good tip selection and the application of one of the different algorithms or protocols proposed to minimise tip's broadening and distortion effects [5,73–75] should contribute to obtain images with lateral features closer to their *real values*.

The DNA image also illustrates another aspect regarding lateral resolution on single objects. The DNA appears protruding 0.4 nm from the flat surface. In general, AFM studies of single biomolecules report heights that are always smaller than nominal values, although the values vary with sample preparation and operating conditions. Smaller heights could be a consequence of different processes. van Hulst et al. [76] have estimated that dehydration could account for a reduction of 0.6 nm in the height of the DNA molecule. It seems also reasonable to expect some sample deformation due to tip–sample forces (see antibody example below). Fig. 16 illustrates convolution and sample deformation effects for a compliant material.

Amplitude reduction depends, in most cases of interest, on the average strength of tip–surface forces as a consequence height anomalies could also come from differences on molecule–tip and substrate–tip interactions. For example, if the local charge distribution on the molecule is different from the substrate the damping of the oscillation amplitude should also be different, and this could give rise to a height difference that is not topographical. The above hypothesis have not been confirmed experimentally in AM-AFM yet. However, Müller and Engel [77] have demonstrated that in contact AFM imaging of protein membranes in liquids, height measurements depend on electrostatic interactions. Those observations suggest that this should also be the case in AM-AFM.

Lateral resolution on biomolecules is also limited by the strength of the tip–surface forces. Möller et al. [6] obtained a lateral resolution of 1.1 nm on a regular protein surface of purple membrane.

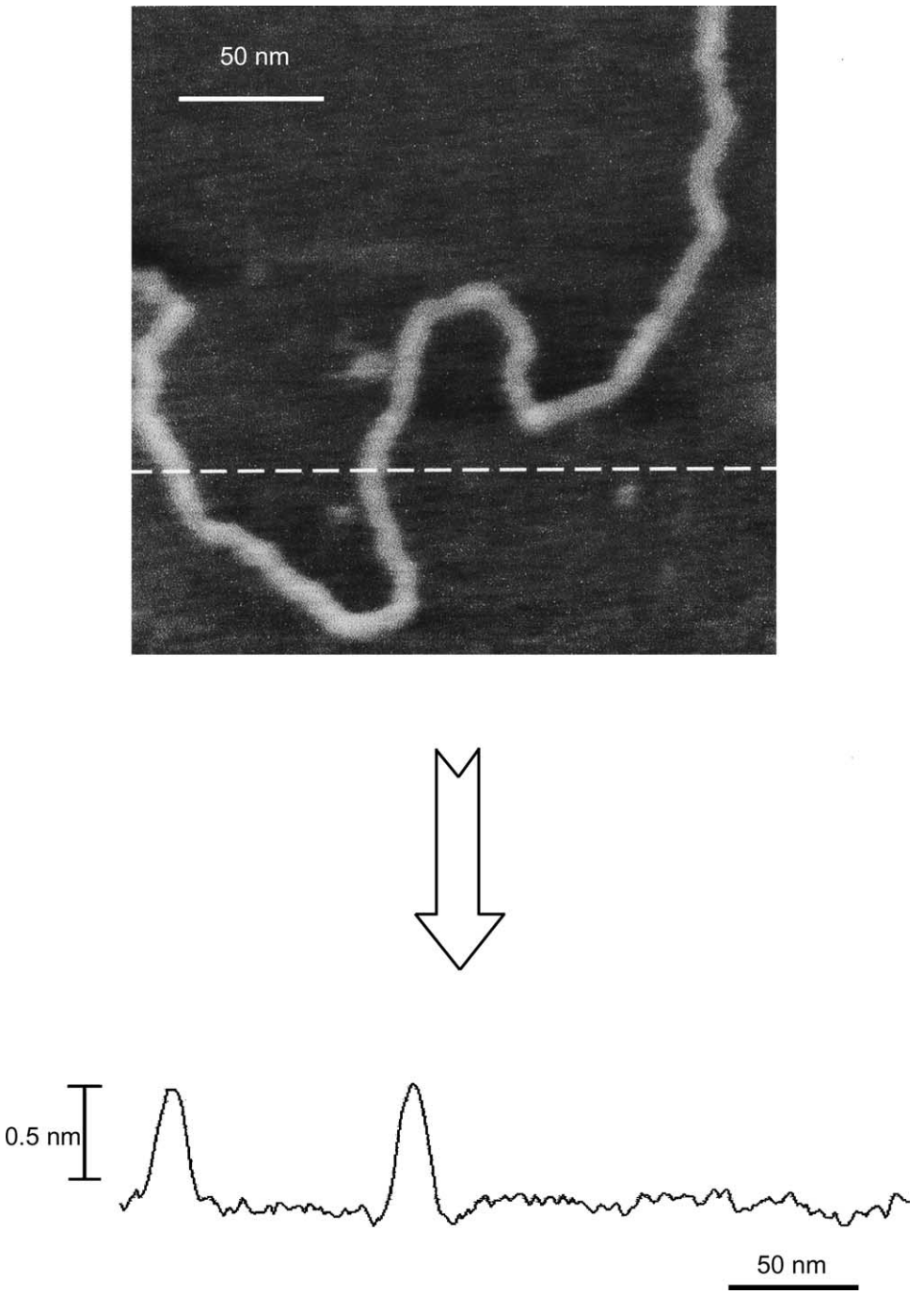

Fig. 15. (a) (top) AM-AFM image of a DNA fragment deposited on mica. (b) (bottom) Cross-section along the dashed line shown in (a).

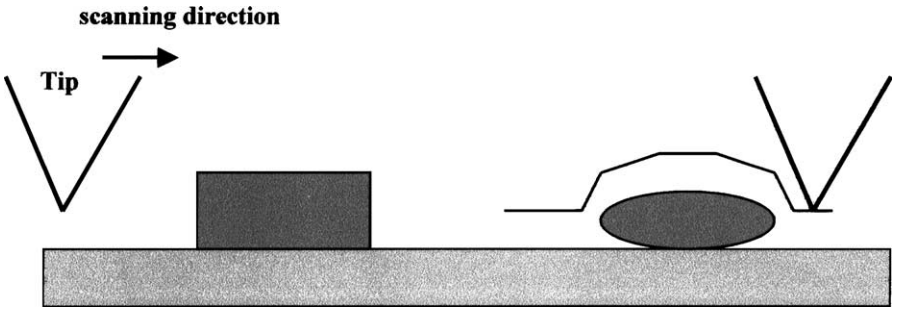

Fig. 16. Schematic of the tip's induced convolution and deformation while imaging. Convolution is mainly a geometrical effect that depends on the geometry of the objects while deformation depends on the strength of the interaction forces and sample mechanical properties.

The key to their success was a combination of small tip–surface forces and the rigidity of the two-dimensional surface. Individual domains of about 6 nm on antibodies have been resolved by operating the instrument in the L branch [7]. The key factor was to realise that the L branch offers easiest conditions to reduce the maximum tip–molecule force (Fig. 13(b)). The antibodies were imaged by applying a maximum tip–molecule force below 0.5 nN. Higher tip–molecule forces produced irreversible sample deformations with the corresponding loss of resolution.

Loss of resolution by irreversible sample deformation should not be a concern only while imaging biomolecules. Fig. 17 shows a cobalt nanoparticle imaged in an L state (Fig. 17(a) and (b)) and the same particle imaged afterwards in an H state (Fig. 17(c) and (d)). The cross-sections obtained in L and H states give a height of 3.3 and 2 nm, respectively. The height change was irreversible because subsequent imaging in the initial L state gave a height of 2 nm. The force (its maximum value) exerted on the particle by imaging in an H state have produced a substantial particle deformation.

On the other hand, H states should be preferred for imaging stiff materials, i.e., whenever sample deformation is not an issue. Usually in most of the L branch there is no tip–surface mechanical contact

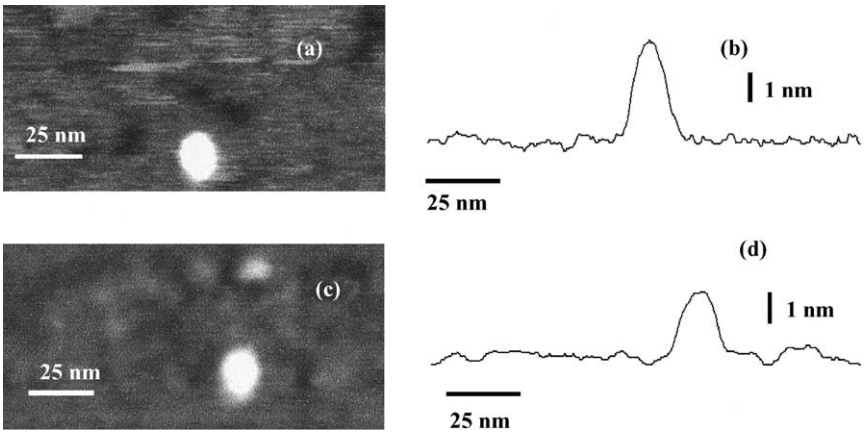

Fig. 17. (a) L state image of a single Co nanoparticle. (b) Cross-section of (a). (c) H state topography of the particle imaged in (a). (d) Cross-section of (c).

(see e.g., Fig. 7(c)), i.e., there is a finite tip–surface separation. This means that imaging is controlled by long-range forces which by their own nature are less sensitive to surface changes than short-range forces. A hint of this behaviour is shown in Fig. 11(b). The average size of the quantum dots is larger in the top (L state) than in bottom of the image (H state).

The above discussion summarises the main factors that influence image resolution in AM-AFM. Some of them are sample dependent such as the sample's compliance while others depend on the nature and geometry of the tip such as the tip's radius and force constant. Finally, there are some factors that depend on operational parameters such as the average and maximum forces. Unfortunately, those factors are not totally independent which in turns complicates the application of general rules.

3. Imaging material properties

Simultaneous mapping of topography and chemical composition has always been one of the main goals of microscopic techniques. The success of AFM to imaging a wide variety of surfaces with nanometer-scale resolution has prompted its application to extract information about the chemical composition of the sample. In the past decade several methods based on AFM have been proposed to image material properties. Friction force microscopy was applied to map compositional domains in phase-separated Langmuir–Blodgett films [78] and semiconductor heterostructures [79]. A more selective approach to study chemical properties was achieved by functionalising the AFM probe to sense a specific chemical or biological interaction. In this way the binding forces of individual ligand–receptors pairs (avidin–biotin) [80] and the adhesion forces between methyl ($-CH_3$) acid (–COOH) and amino ($-NH_2$) groups were determined [81]. Atomic force acoustic microscopy was specifically designed to image material properties [82,83].

However, the capability to achieve chemical contrast by AFM methods has been inferior and not as straightforward as topographic imaging. In most experimental conditions several physical properties contribute to the total tip–surface force. For example, surface forces (such as adhesion) and bulk properties (such elasticity or viscoelasticity) can determine the final tip deflexion. This lack of selectivity may prevent the proper identification of the sample property responsible for the observed behaviour. On the other hand, a model is always needed to relate experimental measurements to material properties. Most of the models applied up to now made use of continuous theories. It is still under debate whether models based on continuous theories can be freely applied to describe the mechanical properties of nanometer-size contacts. Imaging material properties by AFM methods is a rather young topic, so it should not be surprising to find challenges and difficulties in this application.

AM-AFM offers a powerful method for mapping variations in the composition, friction, viscoelasticity and adhesion of the sample surface. This method is called *phase-contrast imaging* or simply *phase imaging*. Below we provide a description of phase imaging as well as the main concepts needed to understand phase images.

3.1. Phase imaging

In the previous section we have seen that the description of AM-AFM starts by considering a tip motion characterised by a (nearly) sinusoidal oscillation with a certain amplitude (the set point amplitude)

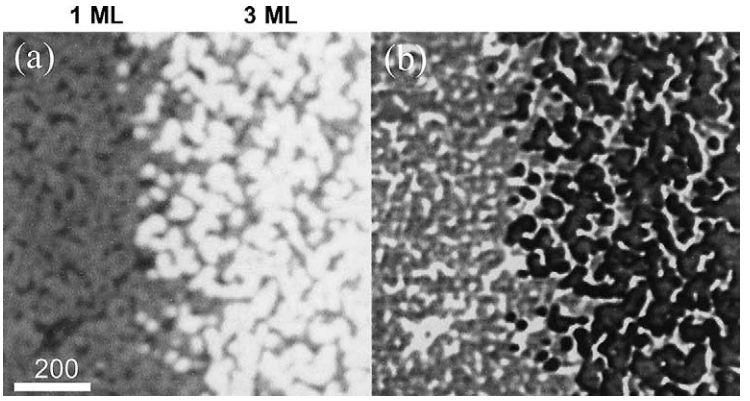

Fig. 18. AM-AFM images of a Langmuir–Blodgett film interface on Si(1 0 0). (a) Topography and (b) phase image of the 1 ML/3 ML interface. $A_0 = 25$ nm, $A_{sp}/A_0 = 0.63$, $f_0 = 322$ kHz. Adapted from [95].

and a phase lag with respect to the external driving force. We have seen that the amplitude depends on $\langle F_{ts}z \rangle$ which in some cases is reduced to a dependence on the average value of the tip–surface force. On the other hand, in a damped harmonic oscillator the phase lag depends on the medium (Q factor) and the relationship between the excitation and resonance frequencies of the oscillator, i.e., the same factors that control the amplitude. Based on the harmonic oscillator analogy it seems reasonable to expect some sensitivity of the phase shift to surface properties.

In phase imaging, the phase lag of the tip relative to the excitation signal is monitored and recorded while the feedback keeps the amplitude at a fixed value. In the few years since the first phase image was published [84] several contributions have investigated the potential of phase imaging to detect variations in material properties such as adhesion, elasticity and viscoelasticity or to image samples with large vertical variations [85–96].

Fig. 18 shows the topography and the phase image of a Langmuir–Blodgett film interface on Si(1 0 0) [95]. The interface was designed to be composed of a monolayer (ML) region and a three monolayer region of an amphiphilic polymer. The differences in height between the first and third monolayers made it difficult to extract morphological information from the topographic image (Fig. 18(a)). However, the phase image reveals that the formation of the 1 ML and 3 ML regions have not been perfect. Bare substrate regions are seen in the 1 ML side (white islands) and some 1 ML regions are embedded in the 3 ML side (Fig. 18(b)).

Fig. 19 provides another striking example of the contrast obtained by phase images. The topography and phase images of a thin film of a hydrogenated diblock copolymer (PEO–PB) are shown [97]. The topography does not reveal any particular features on the polymer surface (Fig. 19(a)), however, the phase image (Fig. 19(b)) allows to establish that the copolymer organises itself in a spherical mesophase for poly-ethyleneoxide (PEO) blocks. It also reveals that crystallisation occurs individually for each sphere (white spheres are crystalline while dark spheres are amorphous).

3.2. Phase shift between excitation and cantilever response: qualitative considerations

Before studying the dependence of phase shifts on mechanical and morphological properties, it will be helpful to revise some basic properties of phase shifts for a damped oscillator with harmonic forcing.

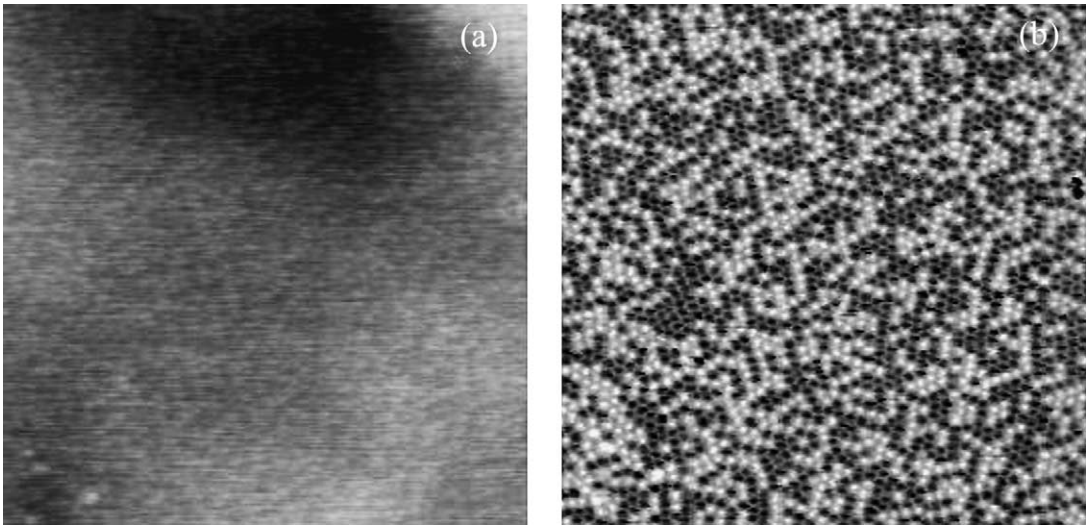

Fig. 19. AM-AFM images of a block copolymer mesophase. (a) Topography and (b) phase image. The phase image allows to resolve the individual spheres (12 nm in diameter). It also allows to distinguish between the crystalline (light) and molten (dark) PEO micelles. Image size 1 mm × 1 mm. The maximum height variation in (a) is 10 nm. By courtesy of Dr. G. Reiter.

For an oscillation described by $z = A\cos(\omega t - \phi)$ the relationship between the phase shift and the driving frequency is given by Eq. (2.13), $\tan\phi = (\omega\omega_0/Q)/(\omega_0^2 - \omega^2)$. This equation establishes that at resonance, the phase lag is exactly 90°. Driving frequencies far below the free resonance produce zero phase shifts. Excitation frequencies far above resonance produce a phase shift of 180°. The dependence of the phase shift with the excitation frequency is plotted in Fig. 20. Nonetheless, it should be noted that the above convention has not always been followed in AFM contributions. Some commercial software has assumed that the cantilever oscillation is shifted 180° when it is excited far

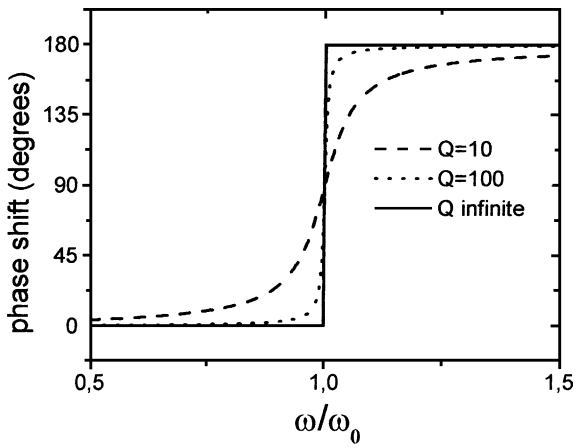

Fig. 20. Phase shift behaviour of a driven harmonic oscillator as a function of driving frequency. For the ideal case ($Q = 0$) there is sharp transition from 0° to 180° at $\omega = \omega_0$. The damping produces continuous changes of the phase shift.

below resonance [98]. Driving frequencies far above resonance produce phase shifts of 0°. This convention implies that a DC excitation produces a displacement of the cantilever that is out phase with the excitation. A compromise between commercial software and physical intuition was proposed in [20]. They have plotted the phase shift in an inverted way. The 0° is at the top of the axes and 180° at the bottom. Although this is a clever compromise it seems artificial. Here, we return to the convention found in most physics textbooks [48].

3.3. Phase shifts and material properties: harmonic approximations

To interpret phase images in terms of sample properties requires to find an expression to relate a given material property with its corresponding phase shift. Let us advance that this is a difficult problem where just a handful of theoretical descriptions have been attempted [50,51,87,92,99,100].

Magonov et al. [50] assumed a harmonic approximation to relate phase shifts and sample stiffness. They argued that the effect of tip–surface interactions on the tip motion could be accounted by introducing an effective force constant $k_{\text{eff}} = k + \sigma$, where $\sigma = \sum \partial F_i/\partial z$ is the derivative of the forces acting on the tip. They proposed to calculate the phase shift by

$$\phi = \tan^{-1}\left(\frac{m\omega_0\omega}{Q(k+\sigma-m\omega^2)}\right) \tag{3.1}$$

If $\sigma \ll k$, the above expression gives

$$\phi = \tan^{-1}\left(\frac{k}{Q\sigma}\right) \approx \frac{\pi}{2} - \frac{Q\sigma}{k} = \frac{\pi}{2} - \varepsilon a E^* \frac{Q}{k} \tag{3.2}$$

where σ has been approximated by the surface stiffness $s = \xi a E^*$, where a is the contact diameter [101]. Eq. (3.2) establishes a proportionality between the phase shift and the reduced Young's modulus of the surface.

A different approach was proposed by Whangbo et al. [51]. They considered that the effects of the tip–surface interactions on the phase shift could described by the introduction of an effective quality factor. They proposed to calculate phase shifts by

$$\phi = \tan^{-1}\left(\frac{\omega_0}{2Q^{\text{eff}}\Delta\omega}\right) \approx \frac{\pi}{2} - 2Q^{\text{eff}}\frac{\Delta\omega}{\omega_0} \tag{3.3}$$

where Q^{eff} and $\Delta\omega$ can be determined experimentally by acquisition of amplitude versus frequency curves. They also proposed a relationship for Q^{eff} and the energy dissipated by tip–surface and hydrodynamic forces $W_{\text{d}}^{\text{eff}}$

$$Q^{\text{eff}} = 2\pi\frac{W_0}{W_{\text{d}}^{\text{eff}}} \tag{3.4}$$

where W_0 is the maximum kinetic energy of the cantilever. Bar et al. [89] found some agreement between the above expression and measurements performed on polystyrene and polydimethylsiloxane samples. Nevertheless, both models suffer from the shortcomings of harmonic approximations to describe AM-AFM (see discussion in Section 2.4.1). Consequently, their validity is restricted to a few experimental situations.

3.4. Phase shift and energy dissipation at the tip–surface interface

A capacitor, a coil and a resistor provides one of the most important resonant systems. The resistor is the element that introduces continuous changes in the phase lag between the driving voltage and the current. In other words, continuous changes in phase shifts can be traced back to dissipative elements in the electrical system. Following this analogy, Tamayo and García [85] performed some numerical simulations that demonstrated that this was indeed the case in AM-AFM. They studied the dependence of the phase shift as a function of the elastic modulus of the sample. It was found that in the absence of dissipative processes at the tip–surface interface, the phase shift *at constant oscillation amplitude* was independent of the elastic modulus. Bar et al. [102] studied the experimental dependence of the phase shift on the elastic modulus by using polydimethylsiloxane samples of different cross-link density. The experimental observations confirmed the theoretical predictions.

Cleveland and co-workers [87,103] have deduced an analytical relationship between the phase angle of the tip motion and the energy dissipated by the tip–surface forces. Their model is based on the assumption that in the steady-state the average energy supplied to the cantilever per period must equal to the average energies dissipated via hydrodynamic viscous interactions with the environment (E_{med}) and by inelastic interactions at the tip–sample interface (E_{dis}), then

$$E_{\text{ext}} = E_{\text{med}} + E_{\text{dis}} \tag{3.5}$$

where

$$E_{\text{ext}} = \oint F_0 \cos \omega t \frac{\mathrm{d}z}{\mathrm{d}t}\, \mathrm{d}t \tag{3.6}$$

$$E_{\text{med}} = \oint -\frac{m\omega_0}{Q}\frac{\mathrm{d}z}{\mathrm{d}t}\, \mathrm{d}z \tag{3.7}$$

$$E_{\text{dis}} = \oint F_{\text{ts}} \frac{\mathrm{d}z}{\mathrm{d}t}\, \mathrm{d}t \tag{3.8}$$

The above equations and the assumption of a sinusoidal cantilever response turns Eq. (3.4) into an expression that relates the phase shift angle (ϕ) with the energy dissipated by the tip–sample interactions, E_{dis}, per period

$$\sin\phi = \frac{\omega}{\omega_0}\frac{A_{\text{sp}}(\omega)}{A_0} + \frac{QE_{\text{dis}}}{\pi k A_0 A_{\text{sp}}(\omega)} \tag{3.9}$$

where ω and ω_0 are the excitation and natural frequencies of the cantilever, respectively.

Tamayo and García [99] have verified the above model by measuring the phase shift dependence on set point amplitude for two different surfaces: a stiff sample, graphite, and a rather compliant sample, a membrane protein surface (purple membrane) (see Figs. 21 and 22). The agreement between experimental data and Eq. (3.9) is very good over a wide range of oscillating amplitudes. The value of E_{dis} in each case was determined from force versus distance curves [99].

A closer examination of Eq. (3.9) reveals the presence of two components, one elastic (A_{sp}/A_0) while the other gathers the inelastic contributions (Q and E_{dis}). The presence of an elastic term seems at variance with the simulations of Ref. [85]. However, phase imaging in AM-AFM is performed at a fixed set point amplitude $A_{\text{sp}} = cte$. This means that the elastic term remains constant while imaging.

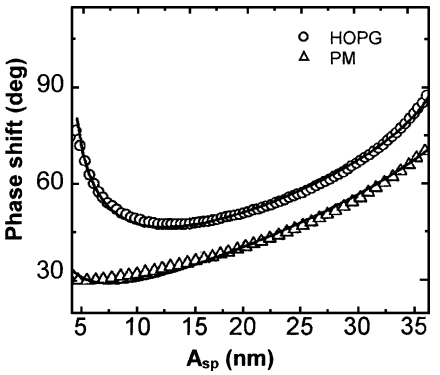

Fig. 21. Experimental and theoretical phase shift dependence on the set point amplitude on a purple membrane (triangles) and on a graphite surface (circles). Solid lines correspond to the theoretical calculations. Adapted from [99].

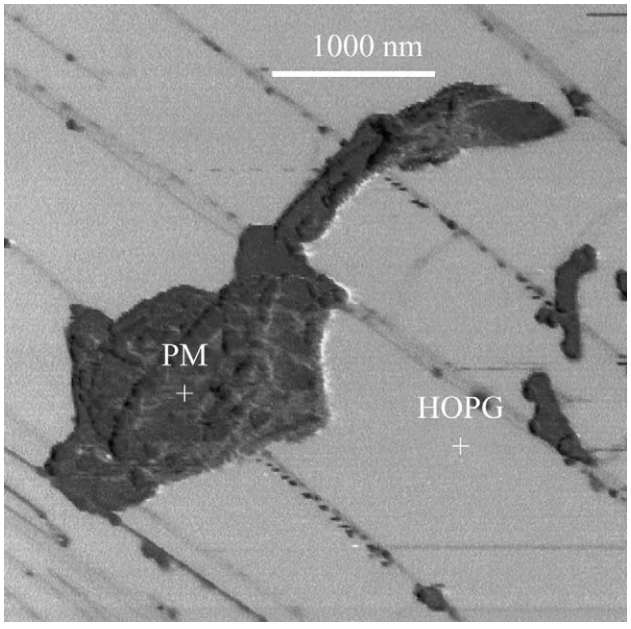

Fig. 22. Phase image of a purple membrane on graphite. A sharp and non-topographical contrast is observed between the membrane and the graphite. The phase shift is 10.5° higher on graphite than on the membrane. The phase shift is independent of the number of membranes piled up. $A_0 = 43$ nm, $A_{sp} = 34$ nm and $f_0 = 356$ kHz. Adapted from [99].

Consequently, changes in phase shifts could only come from changes in the energy dissipated by the tip–sample forces.

3.5. Topographic contributions to phase shifts

Eq. (3.9) implicitly assumes that the electronic feedback responds instantaneously to amplitude changes. However, a finite response time would imply an instantaneous oscillation amplitude A_i

different from A_{sp}. As a consequence, A_i should replace A_{sp} in Eq. (3.9) and phase shifts could also arise from the elastic term (A_i/A_0). This effect is particularly noticeable in regions of the sample with abrupt topographic changes.

Stark et al. [100] have proposed a procedure to separate topographic components from material-dependent contributions to the phase shift. Their approach is based on Eq. (3.5), the consideration of small local variations of the representative quantities (phase, amplitude, energy and topography) around their average values and the finite feedback response. By using a proportional–integral feedback mechanism, they found a relationship between variations in amplitude and topography

$$\delta\left(\frac{A_i}{A_0}\right) = -\frac{v}{\lambda}\delta\left(\frac{\partial H}{\partial x}\right) \tag{3.10}$$

where H is the topography, x the represents the lateral position, v the scanning speed and λ is proportional to the integral gain of the feedback. They also considered that the mechanical energy dissipated per cycle can be considered as a net energy density ε integrated over the interaction area, S

$$E_{dis} = \varepsilon S \tag{3.11}$$

Furthermore, they considered that the interaction area and the dissipation energy density were assumed as independent quantities. Finally, they have obtained

$$\delta\phi = \alpha\delta\left(\frac{\partial H}{\partial x}\right) + \beta\delta E_{dis} \tag{3.12}$$

where H is the topography and δ refers to differences; α, β are coefficients to be determined experimentally. The first term in the above equation (right side) corresponds to contributions of amplitude variations while the second includes changes in the dissipated energy.

3.6. Phase shift dependence on the oscillation branch

Eq. (3.9) provides a quantitative description of the phase shift dependence on inelastic interactions. However, it does not clarify the effect of conservative tip–surface interactions on phase shifts. They are somehow hidden in the elastic term (A_{sp}/A_0). Furthermore, Eq. (3.9) does not specify any phase shift dependence on the oscillation branch.

The virial theorem allows to derive a complementary expression to Eq. (3.9) to calculate phase shifts in AM-AFM [70]

$$\cos\phi = \frac{2Q}{kAA_0}\left[\frac{\langle F_{ts}\rangle^2}{k} - \langle F_{ts}z\rangle + \frac{1}{2}k_cA^2\left(1 - \frac{\omega^2}{\omega_0^2}\right)\right] \tag{3.13}$$

The above equation can be simplified by exciting the tip at resonance $\omega = \omega_0$ and by observing that in many experimental situations the mean deflection of the cantilever is negligible with respect to the oscillation amplitude $(z_0 \ll A)$, then

$$\frac{\langle F_{ts}\rangle^2}{k_c} = \langle F_{ts}\rangle z_0 \ll \langle F_{ts}z\rangle \tag{3.14}$$

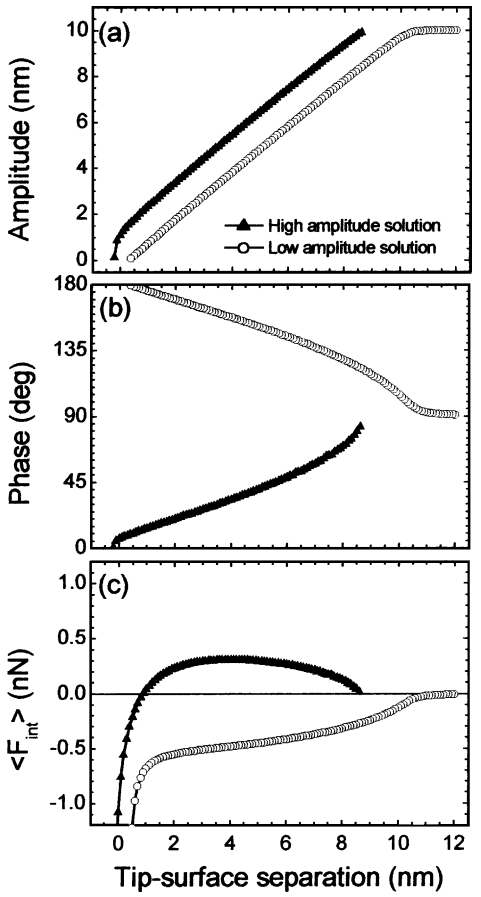

Fig. 23. Dependence on the oscillation branch of (a) amplitude, (b) phase shift and (c) average force as a function of the tip–surface separation; solid symbols correspond to the H branch and light symbols to the L branch.

which reduces Eq. (3.13) to

$$\cos\phi \approx -\frac{2Q\langle F_{\mathrm{ts}}z\rangle}{kAA_0} \tag{3.15}$$

which can be further simplified for conservative interactions and oscillations with small contact times, $\langle F_{\mathrm{ts}}z\rangle \approx -A\langle F_{\mathrm{ts}}\rangle$, then

$$\cos\phi \approx 2\frac{\langle F_{\mathrm{ts}}\rangle}{F_0} \tag{3.16}$$

Eqs. (3.13)–(3.16) show that $\langle F_{\mathrm{ts}}z\rangle$ and $\langle F_{\mathrm{ts}}\rangle$ are parameters that control phase shift variations and contain information on the sample properties. The participation of $\langle F_{\mathrm{ts}}z\rangle$ and $\langle F_{\mathrm{ts}}\rangle$ was also found in the expressions deduced to calculate the amplitude [70] (Eqs. (2.28) and (2.29)), however, a remarkable difference is observed. The phase shift depends on both the average value and its sign. Fig. 23 shows amplitude, phase shift and average force curves for a system with H and L branches. We note that there

are no differences in calculating phase shift curves by using Eq. (3.13) or by direct numerical solution. The theoretical curve has been obtained with the same parameters as in Fig. 7.

In the low amplitude branch the phase shift increases from 90° by decreasing the tip–surface separation. The absence of tip–surface mechanical contact implies that the amplitude reduction is exclusively controlled by long-range attractive forces. Eq. (3.16) applies in this case but for very small separation where the sharp increase of the average force (in absolute value) is not reflected by the phase shift curve. The high amplitude branch shows a different behaviour. Phase shift values decrease monotonously from 90° by decreasing the tip–surface separation in spite of the fact that the average value of the force has a maximum and changes sign. The monotonic decrease of the phase shift could be modified by the presence of inelastic interactions (see Fig. 21). The distinctive behaviour of the phase shift on the oscillation branch allows to use phase shifts to distinguish between H and L oscillation states. Experimental phase shift curves reproducing the above features have been obtained on SiO_2, polyvinyl alcohol and mica surfaces [23,65,66,93].

3.7. Prospects

The usefulness of phase imaging to record material properties variations in heterogeneous samples or to enhance topographic contrast in samples with large topographic variations is beyond doubt. The above analysis has established the intimate relationship between phase shift, dissipative processes at the tip–surface interface and amplitude variations. In the standard AM-AFM mode ($A_{sp} = cte$) topographic contributions in the phase should also be taken into account, particularly when the roughness of the sample is comparable to the tip radius. Those contributions arise from the finite time response of the AFM electronics. The results presented in this section should be considered as the basic elements to develop a general model to interpret quantitatively phase shift variations in terms of properties such as viscoelasticity, adhesion energy hysteresis, plastic deformation and Young's modulus. On the other hand, for experimental conditions that imply the coexistence of oscillation states, phase shifts provide an easy way to discriminate between oscillation states. Phase shifts above 90° are usually characteristic of low amplitude states while phase shifts below 90° are associated with high amplitude states.

4. Selected applications of AM-AFM

Flexible and versatile are two of the adjectives that better describe AFM. Its flexible character allows the AFM to meet different sample requirements. The same instrument can be used to image a variety of systems such as quantum dots, biomolecules, polymers or self-assembled monolayers. On the other hand, the AFM is a technique with a variety of applications such as imaging, manipulation or intermolecular force measurements at nanometer scale.

In this section we provide a short description of some relevant applications of AM-AFM that either have introduced new technical, conceptual or methodological developments. In any case, the examples described below should be considered as representative of the considerable number of AM-AFM applications.

4.1. Biomolecular imaging

High-resolution imaging of biomolecules such as DNA, proteins or cell membranes has been a source of motivation to the AFM community. Several key pivotal developments in scanning probe microscopy

were motivated by the challenges posed to image biological molecules. The invention of the AFM itself was motivated by the limitations of the scanning tunnelling microscope to image insulating materials, biomolecules among them.

Before dynamic AFM modes were developed, reliable AFM imaging of biomolecules was restricted to a few systems such as DNA or regular arrays of protein membranes where immobilisation procedures and/or the rigidity of the sample surface allowed reproducible results. In other cases, weakly attached single macromolecules on the substrate support were often pushed away or damaged by the tip during imaging. The absence or small value of lateral forces in AM-AFM has broaden the variety of biomolecule structures accessible to AFM.

4.1.1. DNA and DNA–protein complexes studies

Single- and double-stranded DNA and DNA–protein complexes have been widely imaged by AM-AFM [5,104–110]. AM-AFM studies of biomolecules involve the deposition of the molecules on a flat support. The transition from three dimensions (solution) to two dimensions (surface) alters the conformation of molecules, in particular for long polymers such as DNA. Those changes may pose some limitations on the information obtained from AFM measurements. Rivetti et al. [108,109] have studied how the adsorption on the surface modifies the conformation of DNA molecules. They have used molecules of different base pairs. By plotting the measured mean-square end-to-end distance as a function of the DNA contour length, they concluded that DNA molecules were able to equilibrate in two dimensions prior to their final attachment to the mica surface. Then, the molecules on the surface represent an ensemble of the lowest energy conformations of molecules existing in a two-dimensional space, thus, meaningful information about the structure of the molecules can be extracted from AFM images. Those studies have validated the conclusions of many AFM studies involving the conformation of DNA fragments and DNA–protein complexes deposited on mica.

One example of DNA–protein complex studies is the interaction of the bacteriophage $\phi 29$ connector with circular and linear DNA molecules [110]. The morphology of DNA–connector interaction is revealed by measuring DNA bend angles. Those angles are readily obtained from AFM images (Fig. 24). The interaction of the connector with circular DNA revealed that the strands of DNA that enter and exit the protein complex form an angle with a mean value of 132° (a)–(c). This angle is consistent with an interaction of the DNA with the outer side of the connector. However, when the connector is incubated with linear DNA there was an additional bend angle of 168° (d)–(f). The images also reveal a structure of the protein–DNA complex with the DNA traversing the connector through its inner channel.

4.1.2. Single proteins

High-resolution imaging of individual proteins physisorbed to surfaces is one of the most challenging tasks for AFM methods. Most AM-AFM images of individual proteins are unable to reveal the fragments or subunits forming the molecule [111]. Several factors such as the tip–molecule convolution or the deformation induced by the tip–molecule forces during imaging are responsible for the lack of contrast.

The theoretical understanding of the tip's dynamics has offered a procedure to improve the lateral resolution of AM-AFM in biology. San Paulo and García have studied the implications of the coexistence of two oscillation states to image biomolecules [7,56]. To this purpose antibody molecules (IgG anti-human serum albumin) were imaged by AM-AFM. Antibody molecules ($\sim$150 kD) are made

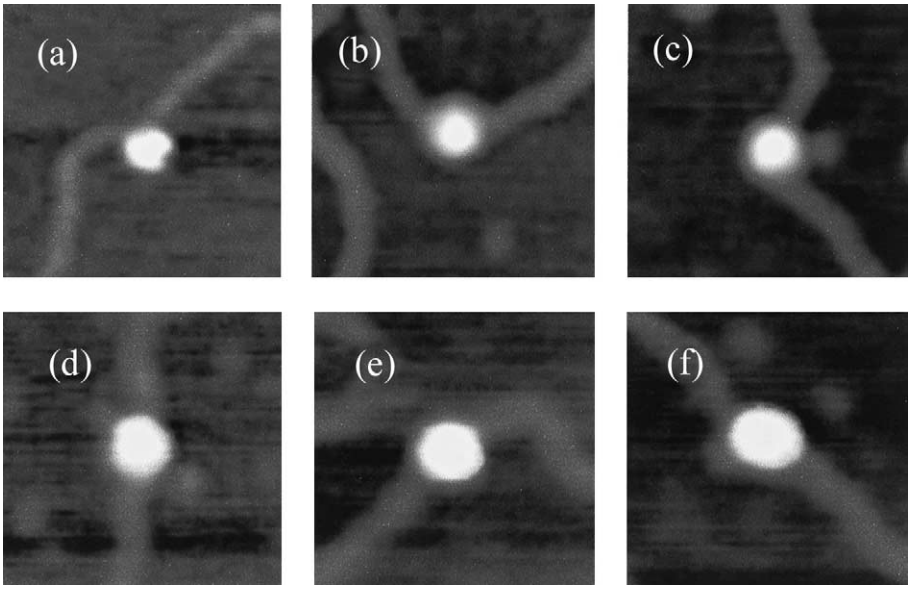

Fig. 24. Topographic images of the different morphologies shown by the DNA/connector complexes. (a)–(c) complexes formed with circular DNA. (d)–(f) Complexes formed with linear DNA (and later circularised). Scan size 150 nm. Adapted from [110].

of three fragments, two separate and identical fragments with active sites for antigen binding Fab and one Fc fragment. The three-dimensional structure resembles a T- or Y-shaped conformation (Fig. 25). This conformation gives antibodies a distinctive morphology. The ability to distinguish this morphology was used to evaluate the performance of L and H oscillation states to image biomolecules.

Fig. 26 shows a typical AM-AFM imaging of a-HAS molecules. The image was obtained in the L sate (or attractive interaction regime). An inspection of the image reveals that the molecules show four basic morphologies. A high-resolution image of each morphology is shown in Fig. 27. Those morphologies have been associated with the orientation of the antibodies on the support. In this way, Fig. 27(a) would be consistent with the antibody resting on the Fab fragments while the Fc protrudes from the surface. Fig. 27(b) would likely represent the opposite situation, the antibody rest on the Fc

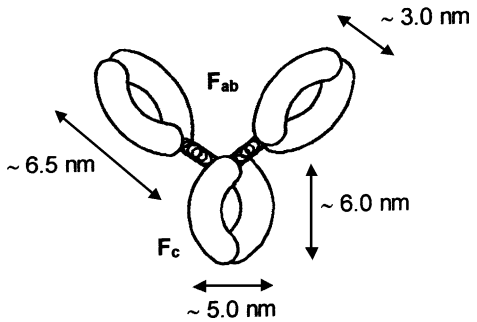

Fig. 25. Schematic drawing and dimensions of the a-HSA molecule showing the Fab arms and the Fc arm.

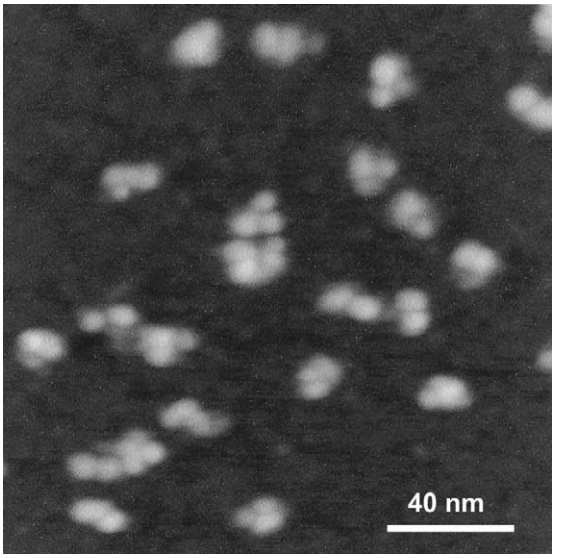

Fig. 26. AM-AFM image (L state) of several antibodies deposited on mica. The molecules show several morphologies according to the orientation of the antibody domains with respect to the support. Several molecules show the characteristic Y shape of antibodies. The image was obtained in air and at room temperature. $A_0 = 5$ nm, $A_{sp} = 4.3$ nm, $f_0 = 250$ kHz.

fragment while the Fab arms stick out of the surface. The molecule could also have one of the Fab arms and the Fc domain attached to the support while the other Fab arm protrudes from the surface. An AFM image of this antibody would produce an image like the one shown in Fig. 27(c). Finally, the Y-shaped morphology shown in Fig. 27(d) would be consistent with the three fragments lying flat on the support.

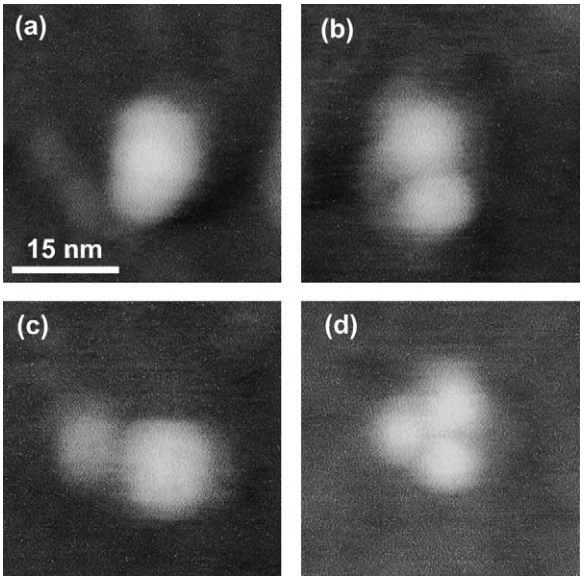

Fig. 27. Characteristic morphologies of antibodies on mica. All images (a)–(d) have been obtained by operating the microscope in an L state. Image size, 40×40 nm^2. Adapted from [7].

This is also supported by the observation that molecules showing this topography show the lowest apparent height (∼1.5 nm).

The different topographies are probably a consequence of the non-specific nature of adhesion on mica. Within each morphology, the lateral and vertical dimensions of the antibodies show a small variability from molecule to molecule due to the flexibility of the hinge region connecting the Fab arm with the Fc domain. For molecules showing a Y shape, the small differences in the lateral dimension of the Fab or Fc domains by AFM (∼8 nm) and X-ray and transmission electron microscopy measurements (6–7 nm) are mostly attributed to the finite size of the tip (nominal tip radius in the 5–15 nm range).

4.1.3. Membrane proteins

The smallest lateral feature resolved by AM-AFM in a biological surface is 1.1 nm on a regular two-dimensional protein layer. Möller et al. [6] have explicitly addressed the issue of high-resolution images of protein surfaces by AM-AFM. The AFM was used to image two different regular protein layers whose structures are known to great detail, the purple membrane from Halobium salinarium and the hexagonally packed intermediate layer from Deinococcus radiodurans. Images exhibited a lateral resolution of 1.5 nm for the HPI layer and of 1.1 nm for the purple membrane. Vertical resolution was about 0.1 nm in both cases.

The image (Fig. 28(A)) shows the extracellular purple membrane surface which exhibits trimeric structures protruding 0.4 ± 0.1 nm above the lipid bilayer. The trimers are arranged in a trigonal lattice of 6.2 ± 0.2 nm side length. After some correlation averaging to enhance the signal-to-noise ratio a major and a minor trimeric protrusion could be distinguished (Fig. 28(B)). The major domains were separated by 2.8 nm while the minor domains were 1.7 apart. The threefold symmetrised standard deviation map is shown in Fig. 28(C). Fig. 28(D) and (E) show some average images of the same surface obtained by contact AFM imaging.

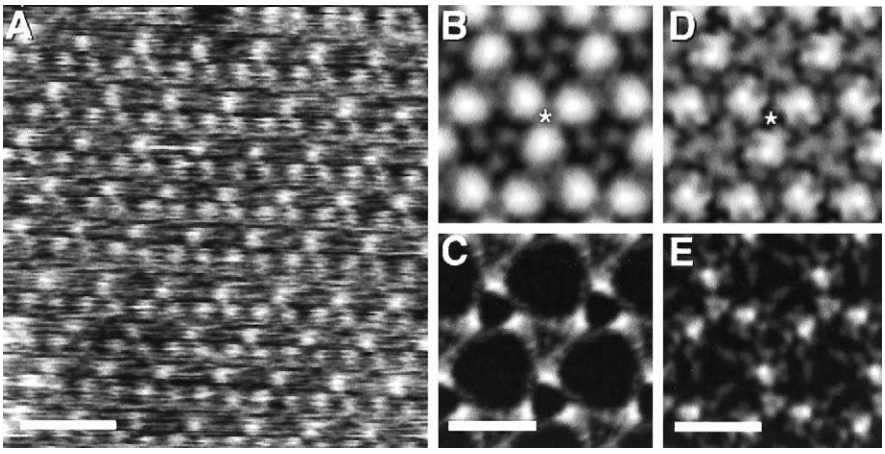

Fig. 28. AM and contact AFM images of the extracellular purple membrane surface. (A) Raw data obtained in 300 nM KCl, pH 7.8, 10 mM Tris–HCl. (B) Threefold symmetrised correlation average. (C) Threefold symmetrised standard deviation map. (D) Averaged topography of the extracellular membrane surface, recorded by contact AFM. (E) Threefold symmetrised standard deviation map of D. The asterisk marks the centre of the bacteriorhodopsin trimer. By courtesy of Dr. D. Müller.

Möller et al. [6] also demonstrated that the AM-AFM was capable of imaging the fragile polypeptide loops connecting the transmembrane α-helices in their native, extended conformation.

4.2. Polymers

Prior to the invention of AM-AFM high-resolution imaging of polymers by scanning probe microscopy was restricted to a few polymer surfaces. Normal and lateral tip–surface forces often produced dramatic modifications of the polymer surface. Most of those modifications came to an end when the polymer was imaged by AM-AFM. Since then a large variety of surfaces such as conducting polymers, single crystals, oriented polymers and block copolymers have been imaged [8,112]. AM-AFM did not just open the potential of scanning probe methods to investigate the nanostructure morphology of polymer surfaces. It also provided an imaging mode, *phase imaging*, specially suited to study polymer surfaces. The sensitivity of the phase to detect surface features and compositional variations has made phase imaging the mode of choice for studying polymer surfaces. Despite the extended use of the instrument to image polymer surfaces a detailed quantitative understanding of the tip–surface interactions in AM-AFM operation on polymer surfaces is still underway [113,114].

Fig. 29 shows the topography (a) and phase image (b) of a wood pulp fibre sample [115]. The roughness of the sample surface and its height variation limit the amount of information contained in the topographic image (a) (grey scale is of 1 μm). However, the phase image reveals a rich structure. The cellulose fibres are visible as well as the lignin residues (white regions).

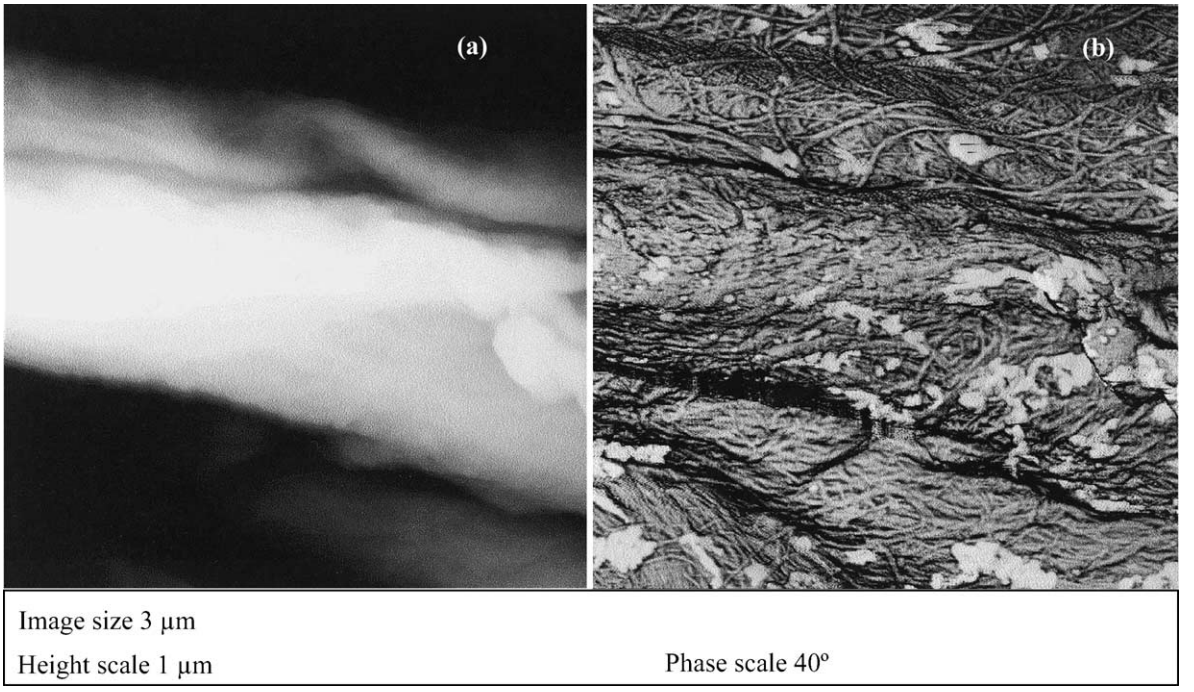

Fig. 29. Topography (a) and phase image (b) of wood pulp fibre. The phase image allows to visualise the fine microfibrils (cellulose) and the amorphous, bright deposits (lignin). Image size 3 mm, height scale 1 mm and phase scale 40°. By courtesy of Dr. D. Chernoff.

The studies of the changes in the polymer morphology and structure as a function of the temperature and the description of the transition between amorphous and crystalline states exemplified the potential of AM-AFM. In the latter aspect, Reiter et al. [97] have used the AFM to record the different processes leading to the transition from an amorphous state to a crystalline state of polymers in constrained geometries. They have used a diblock copolymer mesophase, hydrogenated poly(butadiene-b-ethyleneoxide) with amorphous component (the poly-butadiene block), while the other PEO crystallises at temperatures below $-20\ ^{\circ}C$. The PEO microphase consists of spherical micelles (12 nm in diameter) arranged on a body centred cubic lattice with a lattice constant of 24 nm. Melting of the copolymers occurs, on the other hand, at $+40\ ^{\circ}C$. The sensitivity of phase images to detect in real-space changes in the viscoelastic properties was a key element in their studies.

Fig. 30 is an image of the polymer surface (taken at room temperature) of a sample that was crystallised at $-35\ ^{\circ}C$ for about 5 min. The retraction of the polymer film has uncovered the bare substrate (lower right corner). The central part of the image shows an amorphous film. While in the upper corner shows an ordered arrangement of the PEO spheres. Fig. 30 shows that cells close to the rim (upper part of the image) remained mostly molten (dark spheres) while some distance away from

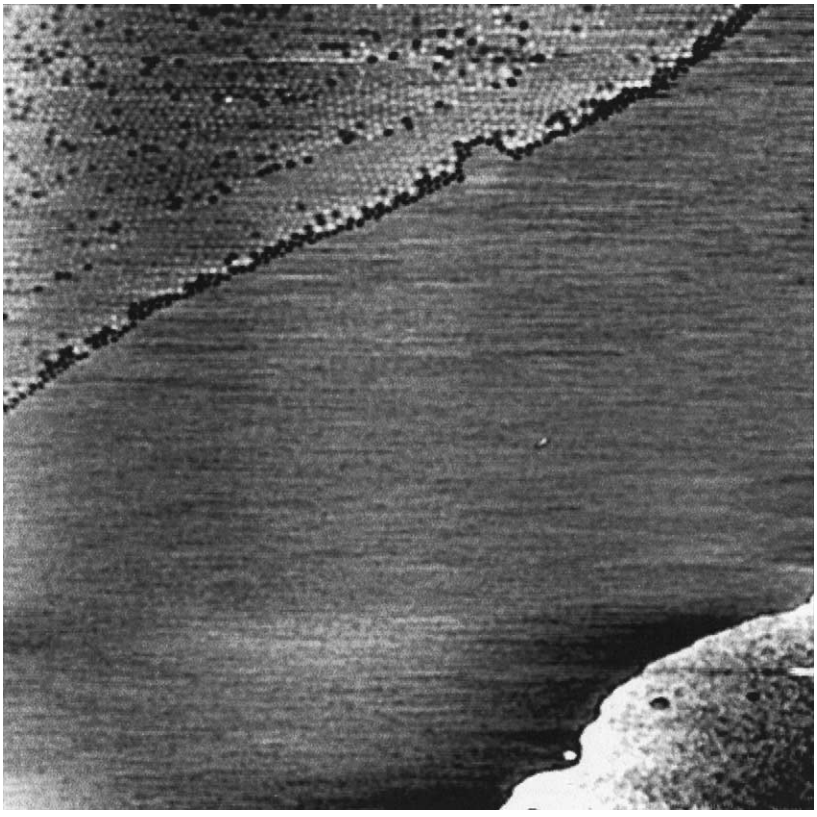

Fig. 30. Phase image of a diblock copolymer mesophase. The image has been taken at the edge of a partially dewetted region. The retraction of the polymer film has uncovered the bare substrate (lower right corner). The remaining ''monolayer'' of about 11 nm is followed by a step of about 15 nm where the rim starts and the sphere micelles are visualised. Image size of $2 \times 2\ \mu^2$. Adapted from [97].

such edges almost all cells are crystalline (bright in the image). Those studies reveal that the spheres crystallise individually and independently sphere-by-sphere. In contrast to techniques averaging over large volumes, AM-AFM images allow to distinguish which cell is melting at which temperature. In this particular example, the authors concluded that all cells crystallised or melted independently, without any correlation between cells.

4.3. Manipulation and fabrication at nanometer scale

The manipulation of atoms, molecules and nanostructures is one of the most exciting applications of scanning probe methods [116]. AM-AFM has also played an important role to develop several methods for manipulation of nanostructures or fabrication of nanometer-scale devices.

Junno et al. [117,118] have fabricated a variety of ohmic contacts, nanowires and gaps between gold electrodes by single manipulation of gold nanoparticles of 50 nm in diameter with an AM-AFM. Their protocol required the switching between imaging and manipulation modes of the instrument. First, the position of the gold particles on the surface was chosen by operating the instrument with a set point amplitude that minimises tip–particle forces (probably they were using a state belonging to the L branch). Then the particles to be moved are selected. The tip is positioned behind the particle with respect to the intended direction of displacement. The feedback is interrupted and the tip is moved into contact with the particle. The actual moving is done by physically pushing the particle with the tip to the desired position. In this way a single particle can be translated in one continuous movement. Finally, the feedback is turned back to the imaging mode to obtain an image of the manipulation. The authors have reported the fabrication of a variety of gaps, gates and ohmic contacts between electrodes. A similar process was applied by Ramachandran et al. [119] to manipulate Au nanoparticles of 5 nm in diameter.

Local oxidation or nano-oxidation lithography is a powerful and versatile approach to fabricate nanometer-scale devices with an AFM [43,120,121]. In a typical local oxidation experiment an AFM tip is brought into close proximity of the sample. Either spontaneously or by the application of an electrical field a water meniscus is formed between tip and sample. The application of an external voltage turns the tip–surface interface into a nanometer-size electrochemical cell where the AFM tip is used as a cathode, the sample acts as the anode and the water meniscus formed between tip and surface is the electrolyte. The strong localisation of the electrical field lines near the tip apex gives rise to a nanometer-size oxide dot. Local oxidation lithography has been applied to fabricate a variety of devices, such as single electron and field effect transistors and data storage units. The image illustrates some of the possibilities for patterning surfaces and for storing information with nano-oxidation (Fig. 31). The image shows π (3.14159265358979323846) written in binary code on a silicon surface. Each dot (SiO_x) is about 30 nm in diameter and the aerial density is about 0.1 Tb/cm^2.

Local oxidation lithography has allowed to perform a quantitative comparison between the performance contact and AM-AFM methods. Tello and García [122] have compared the height and width dependencies on voltage and pulse duration between contact and AM-AFM. For the same electrical conditions, NC-AFM oxides exhibit higher aspect ratios (0.04 versus 0.02) (Fig. 32). This observation is a consequence of two effects. First, operation in an L state allows controlling the lateral size of the liquid meniscus. This in turn controls the lateral size of the oxide dot. Second, the vertical growth rate is smaller in contact AFM oxidation. This effect is a consequence of the mechanical energy needed to deflect the cantilever in contact AFM during the growth of the oxide.

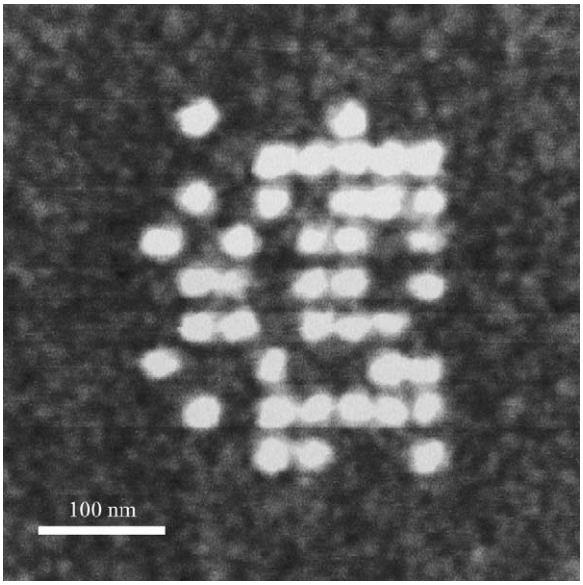

Fig. 31. Topography of π (3.14159265358979323846). π has been written by local oxidation lithography on a binary code. Each silicon oxide dot ('1') is about 30 nm in diameter.

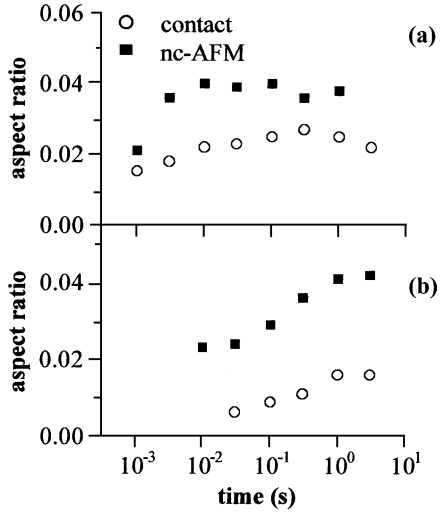

Fig. 32. Comparison of contact and AM-AFM oxidation modes. Aspect ratio (height/width) dependence on pulse duration for different voltage pulses. (a) $V = 20$ V; (b) $V = 14$ V. Adapted from [122].

4.4. AM-AFM in liquids

In previous sections we have presented a comprehensive view of AM-AFM operation in air, i.e., for cantilevers characterised with a quality factor in 50–1000 range. However, there are many relevant

molecules, materials or interactions where imaging in liquids should be preferred. Unwanted capillary forces are eliminated by immersing tip and sample in liquids. Also a fluid environment reduces or prevents tip and sample contamination. Furthermore, imaging in aqueous buffers may be critical for obtaining the morphology of biological molecules near or in physiological conditions. Operation in liquids also opens the possibility of studying biological interactions in situ [123].

In 1994, Hansma et al. [67] and Putmam et al. [124] developed the first amplitude modulation AFMs to be operated in liquids. Since then, a large variety of systems and interactions have been studied [5,111]. However, AM-AFM experiments in liquids are difficult to perform and, in some cases, to understand. The dynamics of the cantilever motion in liquids is far more complex than in air. For example, a larger number of peaks may be present in the oscillation amplitude versus the driving frequency [125] which complicates the choice of the driving frequency. Some of those peaks may come from acoustic vibrations in the liquid cell. However, other peaks could come from the coupling of some of the microcantilever normal vibration modes. The coupling is favoured in liquids with respect to air. The hydrodynamic damping between the liquid and the cantilever also produces a substantial decrease of the quality factor of the cantilever. Common Q values in liquids are in the range 1–10. A comparison of the resonance spectra of a cantilever in air and water is shown in Fig. 33. A cantilever with a k, Q and resonance frequency of 0.75 N/m, 60 and 76.7 kHz, respectively, is immersed in water. A noticeable broadening of the first resonance is observed, which gives a Q of about 3. The resonance frequency has also been reduced by a factor of 3. Additionally, the liquid film confined between the tip and sample surfaces could show some layering effects that could modify the damping of the fluid [126].

Currently, a comprehensive view of AM-AFM operation in liquids is still lacking. Key issues, such as the source of image contrast and resolution remain unsolved. The obvious although technically challenging approach to elucidate the tip motion in liquids would be by solving the equation of motion of the cantilever beam in a fluid. Chen et al. [127] have used a one-dimensional harmonic oscillator model to simulate the tip motion in liquids. Their model accounted for the changes in the fundamental frequency of the cantilever due to the added inertial mass of the liquid in contact with the cantilever. This was an early contribution and its major point was to suggest that surface sensitivity could be achieved with driven excitation frequencies well above the resonance.

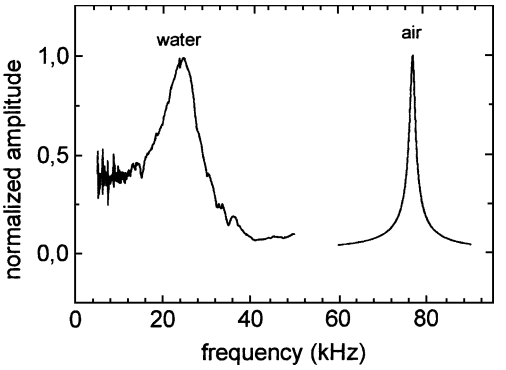

Fig. 33. Experimental resonance curves of a microcantilever in water and air. Note the shift of the resonance frequency and the broadening of the resonance curve when the measurement is done in water.

Sader [16,129] and Scherer et al. [130] have developed methods to solve the motion of a cantilever beam in a fluid (Eq. (4.1))

$$EI\frac{\partial^4 w(x,t)}{\partial x^4}+\mu\frac{\partial^2 w}{\partial t^2}+a_0\frac{\partial w}{\partial t}=F(x,t) \tag{4.1}$$

where a_0 is a coefficient that represents the hydrodynamic damping of the cantilever in the liquid, μ the mass of the cantilever per unit of length. $F(x, t)$ is the applied force per unit of length. It has a hydrodynamic loading component due to the motion of the fluid around the cantilever and an external driving force that excites the cantilever. It includes the added mass of the fluid in contact with the beam. The other parameters have already been defined in Eq. (2.1). Those contributions have analysed, among other things, the coupling of the different oscillation modes of the cantilever. The coupling in liquids is favoured by the broadening and shifting of the lower resonance peaks.

Lantz et al. [128] paid attention to the effect that tip and surface proximity had on the fluid. A compression of the liquid should be expected in the proximity of the surface. The compression should give rise to an interfacial stiffness. Force versus distance curves allowed them to determine an interfacial stiffness of about ~1 N/m. They proposed that the interfacial stiffness was a dominant factor in the amplitude reduction and in the image contrast.

Lately, to minimise some of the effects associated with the broadening of the first resonance peak observed in liquids (Fig. 33), some authors have proposed to enhance the quality factor of the cantilever by introducing an external signal proportional to the instantaneous deflection of the cantilever shifted by 90° [131,132]. However, its practical relevance at the time of the writing of this report is still under debate [133].

5. FM-AFM

5.1. In search of true atomic resolution: FM-AFM

5.1.1. Limitations of the AM-AFM for vacuum operation

Dynamic AFM (dAFM) operated in the AM mode solved some of the problems that appear in the imaging of reactive surfaces with the static AFM. The periodic motion of the cantilever prevents the tip degradation during the lateral scan due to the shear force caused by adhesion, and eliminates the jump-to-contact instability through the restoring force of the cantilever, kA_0. Notice that in dAFM, we have stable operation if any of the following conditions are fulfilled [134]:

$$\max\left|\frac{\mathrm{d}^2V_{\mathrm{ts}}}{\mathrm{d}z^2}\right|=k_{\mathrm{ts}}^{\max}<k,\qquad \max\left|-\frac{\mathrm{d}V_{\mathrm{ts}}}{\mathrm{d}z}\right|=|F_{\mathrm{ts}}^{\max}|<kA_0 \tag{5.1}$$

where V_{ts} is the tip–sample interaction, k the cantilever stiffness and A_0 the oscillation amplitude.

Although most of the applications of the dAFM have been in the intermittent contact (tapping) regime (equilibrium separation of the tip and sample is smaller than the amplitude of the cantilever oscillation), operation in the non-contact regime, where tip deformation and friction effects are eliminated, provided a promising way to achieve true atomic resolution. However, it is not possible to extend the amplitude modulation mode to UHV. The minimum frequency shift detectable in slope

detection due to thermal noise [2,135] depends on the cantilever parameters (stiffness k, $f_0 = (1/2\pi)\sqrt{k/m}$, where m is the cantilever mass, Q the quality factor) and the detection bandwidth, B

$$\delta(\Delta f) = \delta(f - f_0) = \sqrt{\frac{f_0 k_B T B}{4\pi k Q \langle z_{osc}^2 \rangle}} \tag{5.2}$$

where $\langle z_{osc}^2 \rangle$ is the mean-square amplitude of the driven cantilever vibration and $k_B T$ is the thermal energy at temperature T. B is a measure of the scanning speed, operating at small B implies a small scanning speed and long acquisition times. B approximately represents the number of pixels per second that can be recorded. Typically, a scan of a 10 nm × 10 nm area is recorded as an image with 256 × 256 pixels. If we scan four lines per second (scan speed 40 nm/s), this implies $B = 4 \times 256 \sim 10^3$ Hz bandwidth.

From this expression, it seems feasible to increase the sensitivity by more than an order of magnitude operating the dAFM in UHV, where very high values of Q (10^4–10^5) are achievable, as compared to the 10^2–10^3 values typical for air operation. However, in slope detection, increasing the Q reduces the bandwidth of the system. The response of the system to changes in its characteristic parameters, as the resonance frequency, is controlled by Q. After perturbing the system (as we do when we move to a new position over the surface during the scan), the oscillation amplitude as a function of time contains, apart from the new steady-state term (the new resonance curve) we want to measure, two transient terms that decay with time constants $\tau/2$ (transient decay) and τ (transient beat), with $\tau = 2Q/\omega_0$. Thus, τ characterises the time needed for these transient terms to disappear from the measured amplitude and, thus, limits the available bandwidth. For the high Q values in vacuum ($Q = 50{,}000$) and a typical resonant frequency of 50 kHz, we have to wait for 2 s to get a reliable amplitude measurement (maximum available bandwidth is only 0.5 Hz). This makes slope detection unsuitable for most vacuum applications.

5.1.2. FM-AFM

The FM mode developed by Albrecht et al. [3] provided the key to achieve increased sensitivity through higher Q without any restriction on bandwidth. In the FM mode the signal used to produce the image comes from the direct measurement of the resonance frequency of the cantilever, which is modified, as in the AM case, by the tip–surface interaction.

At variance with the AM mode, the cantilever is kept oscillating at its current resonant frequency (different from f_0 due to the tip–sample interaction) with a constant amplitude, A_0. The driving signal of the cantilever oscillation is generated through a feedback loop, where the a.c. signal coming from the cantilever motion detector is amplified, phase shifted (to insure maximum positive feedback on resonance), and then used as the excitation signal. The amplification is adjusted by an automatic gain controller to keep the vibration amplitude constant (see the block diagram of the FM-AFM detection system in Fig. 34). The dynamics of the cantilever is that of a self-driven oscillator, different in many aspects (in particular the approach to the steady-state) from the one generated by the constant excitation (both in frequency and amplitude) used in AM-AFM. In FM-AFM, the spatial dependence of the frequency shift induced in the cantilever motion by the tip sample interaction is used as the source of contrast: During the scan, the tip–sample distance is varied in order to achieve a set value for Δf. Thus, the topography in the images represents a map of constant frequency shift over the surface.

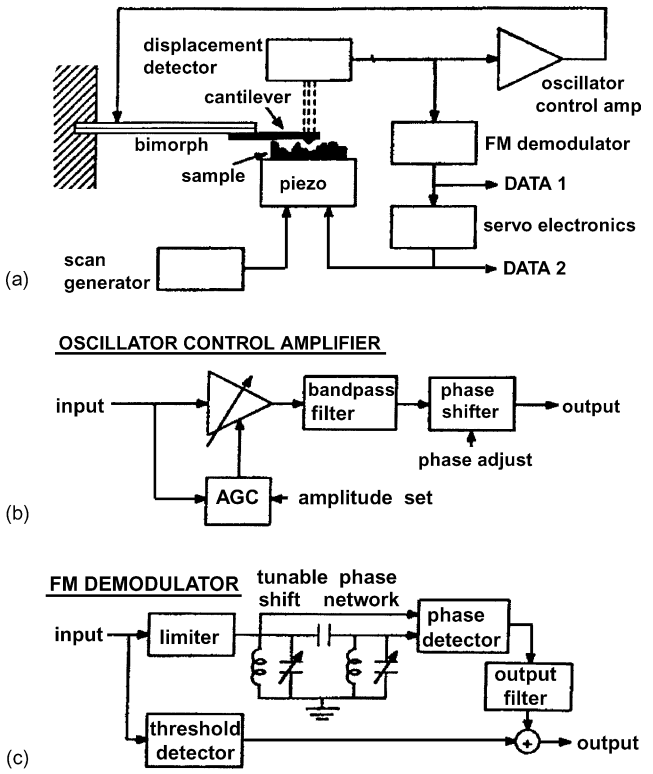

Fig. 34. Block diagram of the FM-AFM. The complete system (a) consists of conventional force microscope components except for the oscillator control amplifier (b) (that keeps the oscillating amplitude equal to the set value A_0) and the FM demodulator (c) (used to determine the frequency shift) (adapted from [3]).

Albrecht et al. [3] have shown that the minimum frequency shift detectable in FM mode was given by

$$\delta(\Delta f) = \sqrt{\frac{f_0 k_B T B}{2\pi k Q \langle z_{osc}^2 \rangle}} = \sqrt{\frac{f_0 k_B T B}{\pi k Q A_0^2}} \tag{5.3}$$

This equation shows that FM and AM modes have essentially the same sensitivity if the same set of parameters are used, but in FM the sensitivity can be increased by using a very high Q; as Q and the bandwidth B are independent in the FM mode, the frequency detection is not affected by the transient terms in the amplitude that limit the AM detection mode and the bandwidth is set only by the characteristics of the FM demodulator. The original demodulator proposed in [3] (see Fig. 34) was already able to measure a frequency shift of 0.01 Hz at 50 kHz with 75 Hz bandwidth. Since then, other FM demodulators have been developed, like the fully digital electronics based on the phase-lock loop principle [136] that offers a resolution of 5 mHz with 500 Hz bandwidth.

5.1.3. The breakthrough: true atomic resolution on the Si(1 1 1)-7 × 7 and InP(1 1 0)

In spite of the promising perspective offered by the increased sensitivity of the FM mode, it was necessary to wait for four more years until Giessibl [9] and Kitamura and Iwatsuki [11]—on the

Si(1 1 1)-7 × 7 reconstruction—and Sugawara et al. [10] on InP(1 1 0) showed the feasibility of atomic resolution with a dAFM, operated in UHV and using the FM detection mode.

Contrary to the first expectations [137], the breakthrough came through the use of stiffer cantilevers ($k \sim 20-40$ N/m) and large oscillation amplitudes (∼300 Å). These conditions were found empirically, guided by the trade-off between the increase of the frequency shift and the sensitivity observed in the experiments. For a given distance of closest approach, the frequency shift becomes smaller when the oscillation amplitude increases, but the sensitivity, according to Eq. (5.3) increases with the oscillation amplitude. On the other hand, the frequency shift increases when the tip–surface distance is decreased, but stable operation becomes more difficult in that ''near contact'' region, where tip–surface forces are large and close to its maximum.

Since that pioneering work, FM-AFM (or NC-AFM, as it is often called) has rapidly matured with applications to more challenging semiconductor surfaces, insulators like alkali halides and oxides, and metals and metallic overlayers [138–142]. The resolution has dramatically improved in the images, with corrugations that are now comparable to the ones obtained in STM [143]. The stable operation achieved by LT-FM-AFM has allowed the imaging of subtle atomic features (as the rest atoms in the Si(1 1 1)-7 × 7 [144] or the corrugation of a Xe monolayer [145]) and the first measurements of the chemical bonding forces above different sites of the unit cell [144,146]. A combined experimental and theoretical work on the CaF_2(1 1 1) surface [147] has recently established an unambiguous identification of the sublattices imaged by force microscopy on an insulator. FM-AFM also appears as a really promising technique in the imaging of organic systems like single- and double-stranded DNA [148] and adenine and thymine films [149]. FM-AFM images provide stronger contrast than tapping-mode AFM and reveal detailed features of the individual nucleic acid molecules that allow to distinguish between adenine and thymine.

Our understanding of the relation between Δf and the tip–sample interaction has also increased significantly during these years, reaching a consensus about the relation between short-range contributions to the total force (of different nature depending on the imaged surfaces) and atomic resolution. This analysis has led to the development of new operation conditions designed to enhance the atomic contrast. Some authors have proposed an operation mode where the Δf modulation is detected, but the condition of constant amplitude, kept by the amplitude feedback loop, is not enforced very rigorously when approaching small values of the tip–surface distance (where the amplitude would start to change significantly in an AM-AFM experiment) [10,143]. This procedure protects the tip in this near-contact region and leads to extremely good contrast. However, understanding this contrast is much more difficult from the theoretical point of view, as changes in frequency shift due to both the tip–sample interaction and the change of the amplitude (only in a harmonic oscillator the frequency is independent of the oscillation amplitude) are mixed in the recorded experimental values. Other groups [150–152] have proposed to keep the standard constant amplitude mode but with different operation parameters (much smaller oscillation amplitudes and stiffer cantilevers) chosen to improve sensitivity to the short-range interactions. Recent experiments implementing this proposal achieve high quality images of the Si(1 1 1)-7 × 7 reconstruction [153]. Progress has also been made in the detection of force gradients using off-resonance excitation with sub-angstrom amplitudes [154,155], including direct observation of short-range bonds [156]. In contrast to this emerging consensus on the interpretation of the frequency shift, a strong debate is still going on about the origin of the atomic resolution observed in images that use the damping (the amplitude A_{exc} necessary to keep the cantilever oscillating with a constant amplitude A_0 during the scan at constant Δf) as the source of contrast.

In the rest of the section we explore some of these issues. We start, in Section 5.2, with a discussion of the relation between frequency shifts and tip–surface interactions, stressing the ability of the simple perturbation theory approach to describe the frequency shift. Section 5.3 shows that short-range chemical forces play a significant role in the atomic resolution achieved by the FM-AFM, giving special attention to semiconductor and ionic surfaces. The inversion procedures to determine the interaction forces from the frequency shift are discussed in Section 5.4. Notice that this inversion procedures provide the FM-AFM with spectroscopic capabilities. The optimal range of experimental operation parameters, still a controversial issue, is reviewed in Section 5.5. Finally, the information on the microscopic damping mechanisms obtained from experiments and simulations is considered in Section 5.6.

5.2. Relation between the frequency shifts and the tip–sample interaction

In this section we will assume that the forces F_{ts} between the nanometer-size tip at the end of the cantilever and the sample are known and concentrate in the description of the dynamics of the cantilever under the influence of such tip–surface forces. F_{ts} will include both attractive and repulsive contributions with different ranges.

Our goal will be to find a relation between the frequency shifts measured in the experiment and the tip–surface forces. This is a complicated dynamical problem due to the intrinsic anharmonicity of F_{ts} and the effective non-local character of the interaction: In the usual operation conditions of the FM-AFM, vibration amplitudes much larger than the range of the interactions included in F_{ts} are used, and thus, the cantilever is sensing the interaction just for a very small part of its oscillation cycle.

5.2.1. The general equation of motion for the cantilever

The motion of the cantilever can be reduced to a one-dimensional problem in terms of the coordinate in the direction perpendicular to the surface, $z(t)$, and will be governed by the following equation (with z_c the cantilever support distance, see Fig. 3)

$$m\ddot{z}(t) + \frac{mQ}{\omega_0}\dot{z}(t) + kz(t) - F_{ts}[z_c + z(t)] = F_{exc}(t) \tag{5.4}$$

Eq. (5.4) is formally identical to the equation of motion used for the analysis of the AM-AFM, apart from the excitation term $F_{exc}(t)$, that describes the excitation of the cantilever motion through the driving piezo. At variance with the AM-AFM, $F_{exc}(t)$ is no longer a pure harmonic driving force $F_{exc}(t) = kA_{exc}\cos(\omega_{exc}t)$ with a constant excitation amplitude A_{exc} and constant frequency ω_{exc}, but a function describing the oscillator control amplifier where the new excitation signal is generated. The amplifier takes the input signal coming from the cantilever motion detector, modifies its amplitude to force the system to oscillate at the set amplitude A_0, and shifts the phase of this signal in order to excite the cantilever close to resonance conditions. This feedback loop keeps the cantilever always vibrating at its current resonance frequency with the same constant amplitude A_0, set at the beginning of the experiment.

Gotsmann et al. [157] proposed that $F_{exc}(t)$ can be described by a PI controller:

$$F_{exc}(t) = R(t)z(t - t_{phase}),$$
$$R(t) = p[A(t) - A_0] + i\int_{t'=0}^{t}[A(t') - A_0]\,dt' = r\left\{[A(t) - A_0] + \frac{1}{\tau_{pi}}\int_{t'=0}^{t}[A(t') - A_0]\,dt'\right\} \tag{5.5}$$

Here $R(t)$ is the loop-gain function that depends on the vibration amplitude $A(t)$ (its current and previous values), the targeted set amplitude A_0, and the settings of the PI controller (p, i or r, τ_{pi}), that characterise the response of the device (typical values, according to [157], are $r = p = 10^5$ N/m^2 and $\tau_{pi} = 1.67 \times 10^{-3}$ s). The time delay t_{phase} is introduced in order to assure that the excitation of the cantilever is always done in resonance (setting $t_{\text{phase}} = 3/4f$, with $f = f_0 + \Delta f$ the current frequency, corresponds to a phase shift of $\pi/2$ between excitation and displacement).

Although it is not possible to write down analytical solutions of the complicated integro-differential equation that results from the combination of Eqs. (5.4) and (5.5), it can be numerically integrated. This was done originally by Gotsmann et al. [157]. Recently, Gauthier et al. [175] have performed fully non-autonomous simulations of the real operation of the microscope, where the action of the FM-AFM electronics was explicitly included in the dynamical equations (see the end of Section 5.2.7). These calculations provide the most solid argument to justify the description of the cantilever motion in the FM-AFM as a weakly perturbed harmonic oscillator with a modified frequency due to the tip–surface interaction that serves as the basis for the different perturbative approaches that have been developed to get an analytical relation between the frequency shift and the F_{ts}. We will discuss first the motivation and justification for the perturbation theory approach, leaving the comparison of the different approximations with the numerical solutions of (5.4) and (5.5) to Section 5.2.4.

In AM-AFM, the dynamic interplay between dissipation and the constant excitation of an anharmonic oscillator gives rise to a wealth of phenomena in the cantilever motion that has been described in the previous sections. In the FM-AFM case, we have a self-excited system that is forced, through the oscillator control amplifier, to vibrate at its mechanical resonance with a constant amplitude. The feedback loop thus assures that the energy losses (both the ones intrinsic to the cantilever and the ones due to the tip–surface interaction) are exactly compensated by the excitation dynamically, in order to keep the amplitude constant. Under these conditions, both the excitation and damping terms in Eq. (5.4) can be neglected and we can write down the conservative equation (only conservative interactions are included in F_{ts})

$$m\ddot{z}(t) + kz(t) - F_{\text{ts}}[z_{\text{c}} + z(t)] = 0 \tag{5.6}$$

This equation can be solved numerically in a very efficient way, as has been done by Hölscher et al. [53], and provides a convenient tool to simulate FM-AFM images.

Notice that, only in the case of small oscillation amplitudes, it is a reasonable approximation to linearise the interaction force around the lever support distance z_{c}, to write the following equation:

$$m\ddot{z}(t) + (k + k_{\text{ts}})z(t) = 0 \;\text{ with }\; k_{\text{ts}}(z_{\text{c}}) = -\left.\frac{\partial F_{\text{ts}}(s)}{\partial s}\right|_{s=z_{\text{c}}} \tag{5.7}$$

and to obtain an analytic expression for Δf in terms of the force gradient $k_{\text{ts}}(z_{\text{c}})$:

$$\Delta f(z_{\text{c}}) = \frac{f_0}{2k} k_{\text{ts}}(z_{\text{c}}) \tag{5.8}$$

valid if $k_{\text{ts}} \ll k$.

5.2.2. *Perturbation theory for Δf in the large oscillation amplitude limit*

In FM-AFM experiments, the oscillation amplitudes used are usually very large compared to the tip–surface interaction range, and the linear approximation represented by Eq. (5.8) is no longer valid. However, in this limit, a new approximation can be made to Eq. (5.6). For the typical oscillation

amplitudes and the stiff cantilevers, the elastic energy stored in the cantilever $(1/2)kA_0^2$ is large compared with the energy associated to the tip–surface interaction. The restoring force at the turning point close to the surface, kA_0, is also large compared with $F_{ts}(d \simeq z_c - A_0)$ (for $k = 30$ N/m and $A_0 = 200$ Å, $kA_0 = 600$ nN and $(1/2)kA_0^2 = 3.75 \times 10^4$ eV compared to typical values of 1–5 nN and 1–10 eV for the tip–surface interaction). Thus, the cantilever can be considered as a weakly perturbed harmonic oscillator, and Δf can be calculated using classical first-order perturbation theory, as suggested, for the first time, by Giessibl [134].

Since then, many different approaches [151,152,158–162], based on the application of different perturbation schemes in the limit of large oscillation amplitudes, have been developed. The central result in all of them is the following relation between the frequency shift and the average of F_{ts} in a full harmonic cycle:

$$\Delta f(d,k,A_0,f_0) = -\frac{f_0}{kA_0^2}\langle F_{ts} z\rangle = -\frac{f_0}{kA_0^2}\frac{1}{T_0}\int_0^{T_0} F_{ts}[d + A_0 + A_0\cos(2\pi f_0 t)]A_0\cos(2\pi f_0 t)\,dt$$
$$= -\frac{1}{2\pi}\frac{f_0}{kA_0}\int_0^{2\pi} F_{ts}[d + A_0 + A_0\cos\varphi]\cos\varphi\,d\varphi \tag{5.9}$$

Notice that Δf depends on the operation conditions (k, A_0, f_0) and the distance of closest approach d. This formulation is equivalent to the numerical solution of Eq. (5.6), except that we have lost the information about the time averaged deflection of the cantilever due to the mean tip–sample interaction, but this is very small (see below) and we can safely consider $d \simeq d_0 = z_c - A_0$. Analytical expressions for the Δf associated with different power law and exponential tip–sample forces can be found in Appendix A.

5.2.3. *Fourier expansion and variational approach*

Eq. (5.9) provides a straightforward first-order evaluation of the frequency shift, assuming that the motion is still approximately harmonic. The approach based on the Fourier expansion [151,152,160] (we follow closely the variational formulation of Dürig [151,152]) shows that the assumptions in the perturbation approach (like the fact that the mean deflections and the higher harmonics are indeed negligible when the oscillation amplitudes are large compared with the interaction range) are fulfilled, and provides insight into why the frequency shift is so sensitive to what happens at the distance of closest approach.

Considering that the system has a periodic motion and is conservative, $z(t)$ has to be an even function with respect to time reversal. Thus, $z(t)$ can be written as a Fourier series involving only cosine functions: $z(t) = \sum_{n=0}^{\infty} a_n \cos(n\omega t)$. Introducing this expression into Eq. (5.6) and using the orthogonality of the cosine functions one gets the following set of coupled equations (one for each n) linking the Fourier coefficients a_n with the interaction F_{ts}:

$$0 = a_n(1 + \delta_{n,0})\pi(\omega_0^2 - n^2\omega^2) - \frac{\omega_0^2}{k}\int_0^T F_{ts}\left[z_c + \sum_{k=0}^{\infty} a_k\cos(k\omega t)\right]\cos(n\omega t)\omega\,dt \tag{5.10}$$

where we have made explicit that F_{ts} has to be evaluated at the actual cantilever motion described by $z(t)$. To proceed, we assume that the interaction is weak in the sense that all Fourier coefficients with $n \neq 1$ are small compared with a_1, the amplitude of the harmonic term. Thus, we can consider

$a_k = 0, \forall\, k \neq 1$ in $z(t)$ in the integrand, to get the following expressions for the a_n:

$$a_n = \frac{1}{(1+\delta_{n,0})\pi} \frac{\omega_0^2}{k(\omega_0^2 - n^2\omega^2)} \int_0^T F_{ts}[d + a_1(1+\cos\omega t)] \cos(n\omega t)\omega \, dt \tag{5.11}$$

For a_1, the previous expression yields precisely the perturbation theory result (Eq. (5.9)), as can be seen using that

$$\frac{\omega_0^2 - \omega^2}{\omega_0^2} \simeq -2\frac{\Delta\omega}{\omega_0} = -2\frac{\Delta f}{f_0}$$

The term a_0 represents the average deflection of the cantilever from its equilibrium position (the lever support position) due to the tip–sample interactions:

$$a_0(d) = \frac{1}{2\pi k} \int_0^T F_{ts}[d + a_1(1+\cos\omega t)]\omega \, dt = \frac{1}{2\pi k} \int_0^{2\pi} F_{ts}[d + a_1(1+\cos\varphi)] \, d\varphi \tag{5.12}$$

Calculations [144] show that a_0 is typically less than 0.01 Å for the usual dynamic conditions of large oscillation amplitudes and stiff cantilevers used in FM-AFM and can be neglected.

Anharmonic corrections can now be explored using Eq. (5.11) to relate a_n and a_1. Dürig [151] has shown that

$$a_n = -a_1 \frac{2}{n^2 - 1} \frac{\Delta f}{f_0} \quad \forall\, n \geq 2 \tag{5.13}$$

The amplitude of the higher harmonics scales with $\Delta f/f_0$ and $1/n^2$, so for the common working conditions ($\Delta f \sim$ 10–100 Hz, $f_0 \sim$ 50–100 kHz), they are generally 2–3 orders of magnitude smaller than the fundamental oscillation amplitude a_1.

More insight into the origin of Δf can be gained with a change from the circular variable ωt to the variable $u = \cos(\omega t)$, related to the position over the tip–sample axis, to get the following expressions for the a_n:

$$a_n = \frac{2}{(1+\delta_{n,0})\pi} \frac{\omega_0^2}{k(\omega_0^2 - n^2\omega^2)} \int_{-1}^{1} F_{ts}[d + a_1(1+u)] T_n(u) \frac{du}{\sqrt{1-u^2}} \tag{5.14}$$

where we have used $z_c = d + a_1$ and $T_n(u) = \cos(n \arccos(u))$ denotes the nth order Chebyshev polynomial of the first kind. These polynomials form a complete orthogonal set with respect to the metric $(1-u^2)^{-1/2}$. The first few polynomials are $T_0 = 1$, $T_1 = u$, $T_2 = 2u^2 - 1$, $T_3 = 4u^3 - 3u$, and higher order ones can be obtained with the recursion relation $T_{n+1}(u) = 2uT_n(u) - T_{n-1}(u)$.

The frequency shift can be determined from the equation for a_1

$$\Delta f(d) = \frac{f_0}{\pi k a_1} \int_{-1}^{1} F_{ts}[d + a_1(1+u)] u \frac{du}{\sqrt{1-u^2}} \tag{5.15}$$

This result, equivalent to Eq. (5.9), provides the clue to understand why there is a significant effect in the cantilever motion, even if the tip is just sensing the interaction in a small part of the oscillation cycle. Notice that the term $(1-u^2)^{-1/2}$ weights the interaction in proportion to the relative fraction of time that the tip spends at the given position. This kernel has a weak singularity precisely at the turning points of the oscillation (in particular, the point of closest approach to the surface), where the velocity

goes to 0 and the tip spends the largest fraction of the time. This explains the sensitivity of the frequency shift to $F_{ts}(d)$.

5.2.4. Integration of the equation of motion versus perturbation approaches

In order to assess the validity of the approximate analytical methods outlined in the previous paragraphs it is necessary to compare their predictions with the results of an proper integration of the cantilever equation of motion.

Hölscher et al. [53] have tested the validity of the different approximate calculations to represent the conservative dynamics described by Eq. (5.6) with both long-range and short-range inverse polynomial forces. In particular, they have considered a cantilever with $k = 40$ N/m and $f_0 = 170$ kHz, a vdW force given by $F_{vdW}(s) = -A_H R/6s^2$ ($A_H = 0.1$ aJ, $R = 120$ Å) and short-range polynomial forces with $n \geq 7$. Fig. 35 shows that the perturbation approach (continuous line) given by Eq. (5.9) (see Eqs. (A.2) in Appendix A for the analytical expressions) describes, with an accuracy better than 3%, the frequency shifts calculated by integration of the equation of motion for the vdW interaction for the two oscillation amplitudes (10 and 100 Å) and all the tip–sample distances. Notice that, as expected, the interpretation of frequency shifts as force gradients (which assumes a small variation of F_{ts} during the oscillation cycle) is only satisfactory for support distances z_c significantly larger (>$3A_0$ according to their results) than the oscillation amplitude A_0. On the other hand, the large-amplitude limit of the perturbation theory—a further simplification of Eq. (5.9), discussed in Section 5.2.5, for the case $d \ll A_0$ and given by Eq. (5.18) (see Eq. (A.3) for this particular case)—works very well for $A_0 > 10d$.

Further validation of the perturbation approach requires the comparison with the results of the integration of the general equation of motion (5.4), where both the dissipative effects and the action of feedback loop that keeps the oscillation amplitude constant are taken into account. Fig. 36 compares the numerical solution by Gotsmann et al. [157] with the large-amplitude limit of perturbation theory for a trial force $F_{ts}(s) = -(C_2/s^2) + (C_3/s^3)$. Notice that the interplay between the attractive and repulsive

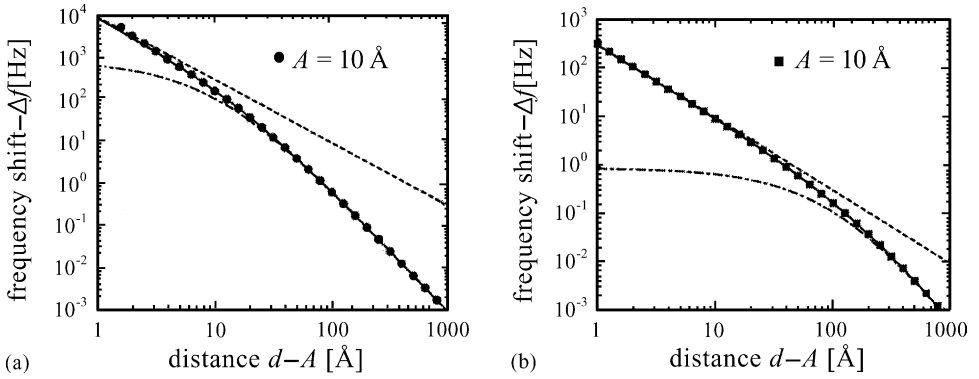

Fig. 35. Comparison of the frequency shifts calculated, as a function of the distance of closest approach d, with numerical simulations of the conservative Eq. (5.6) (black circles in (a) and squares in (b)) and different analytical approximations. A vdW force given by $F_{vdW}(s) = -A_H R/6s^2$ ($A_H = 0.1$ aJ, $R = 120$ Å) and two different oscillation amplitudes A (10 and 100 Å) are considered. The perturbation result (Eq. (5.9), continuous line) reproduces with an accuracy better than 3% the numerical result. The large amplitude approximation (Eq. (5.18), dashed line) performs very well provided that d is small compared with the oscillation amplitude, while the description in terms of local force gradients (dashed-dotted line) is only useful in the limit of small amplitudes and large d (cantilever properties: $k = 40$ N/m and $f_0 = 170$ kHz) (adapted from [53]).

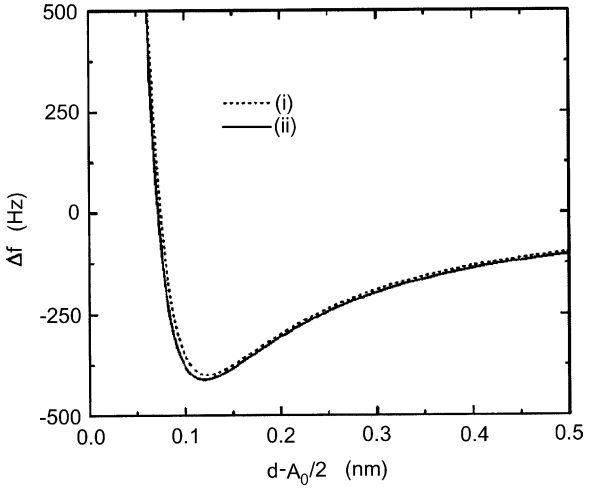

Fig. 36. Comparison of frequency shifts calculated from numerical simulations (dashed line) of the general Eq. (5.4)—where both the dissipative effects and the action of feedback loop that keeps the oscillation amplitude constant are taken into account—and the large amplitude limit of the perturbation theory (Eq. (5.18), continuous line) for a trial force $F_{ts}(s) = -C_2/s^2 + C_3/s^3$ with $C_2 = 5 \times 10^{-28}$ Nm^2 and $C_3 = 4.8 \times 10^{-38}$ Nm^3 (operation parameters: $k = 40$ N/m, $f_0 = 300$ kHz, $Q = 20\,000$ and $A_0 = 200$ Å) (adapted from [157]).

terms in the force leads to the characteristic non-monotonic behaviour of the frequency shift. There is a remarkable agreement between the two approaches, even in the repulsive regime close to contact, with differences of few percent in the region far from the surface, that increase to some 10% near the surface. Discrepancies far from the surface are probably due to the large-amplitude limit used for the comparison, that actually overestimates the frequency shift calculated from the exact Eq. (5.9), with errors of the same order—4% comparing the exact (Eqs. (A.2)) and approximate (Eq. (A.3)) expressions at $d = 5$ Å—as the differences with the numerical result. If the apparently larger quantitative deviations near the minimum of Δf are indicative of some fundamental difference between the conservative approach and the one given by Eq. (5.4) is difficult to assess without further information about the way Δf is determined in the numerical simulations (recall the differences around 3% found in [53] when comparing analytical and numerical results for the conservative equation).

These conclusions remain valid for more realistic tip–sample interactions (like the MYD/BHW model [39]), and do not depend on the Q value, the time step Δt used in the numerical simulations (provided that $\Delta t > 1/500 f_0$) or the PI parameters [157]. This confirms the validity of the "conservative" assumption: in the self-maintained oscillation imposed in FM-AFM, Δf is not significantly affected by dissipation effects, which are compensated by the feedback loop, and can be calculated using the perturbation result (Eq. (5.9)).

5.2.5. *Normalised frequency shift* γ

Eq. (5.9) reflects the dependence of Δf both on the operation parameters k, A_0, f_0 and the tip–surface interaction. Giessibl [134,163] has shown that, in the limit of large amplitudes compared to the range of F_{ts}, it is possible to isolate the two contributions and extract the intrinsic contribution coming from the tip–surface interaction.The analysis of Δf associated with inverse-power and exponential forces [134]

suggests to define a "normalised frequency shift" $\gamma(d)$

$$\gamma(d) = \frac{kA_0^{3/2}}{f_0}\Delta f(d, k, A_0, f_0) \tag{5.16}$$

representing the intrinsic contribution of the tip–surface interaction.

Using Eq. (5.9) for the frequency shift and the substitution $z' = A_0[1 + \cos(2\pi f_0 t)] = A_0[1 + \cos\varphi]$, one gets

$$\gamma(d, A_0) = \frac{1}{\sqrt{2}\pi}\int_0^{2A_0} \frac{F_{ts}[d + z']}{\sqrt{z'}} \frac{1 - (z'/A_0)}{\sqrt{1 - (z'/2A_0)}}\, dz' \tag{5.17}$$

Notice that $\gamma(d, A_0)$ still depends on A_0 (exact expressions for different interactions can be found in Appendix A). But, in typical experiments, A_0 is very large compared with the range of F_{ts}, and the second factor in the integral is very close to unity in the region where F_{ts} is not vanishing. Therefore, we can eliminate that factor and extend the integration limit to ∞ to get an expression for the "large-amplitude" normalised frequency shift γ_{lA}

$$\gamma_{lA}(d) = \frac{1}{\sqrt{2}\pi}\int_0^{\infty} \frac{F_{ts}[d + z']}{\sqrt{z'}}\, dz' \tag{5.18}$$

γ_{lA} is a good approximation to γ for any class of tip–sample forces provided that the range of the forces is small compared to A_0. (This is always the case for exponential and polynomial interactions, except $1/z$, for A_0/d and $A_0\kappa$ larger than 10, typical in FM-AFM experiments [163]).

FM-AFM experiments and simulations (like the ones described in the previous section) follow nicely this prediction. Fig. 37 shows Δf versus distance curves for graphite taken with different amplitudes [164]. All these curves collapse to a single curve for the "normalised frequency shift" $\gamma_{lA}(d)$.

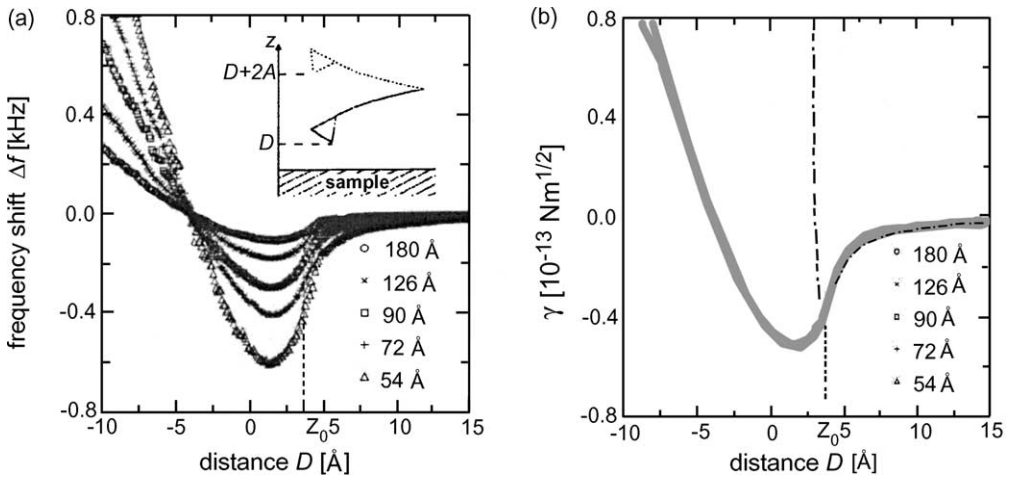

Fig. 37. (a) Experimental frequency shift versus distance curves acquired with a silicon tip and a graphite sample for different amplitudes. (b) The normalised frequency shift γ as a function of the distance of closest approach D obtained from the experimental data using Eq. (5.16). All data points perfectly fit to a single curve within the full range, demonstrating the validity of the $1/A^{3/2}$ scaling (adapted from [164]).

Table 1
Three basic types of tip–sample forces and their corresponding normalised frequency shifts γ_{1A} and $F_{ts}\sqrt{V_{ts}/F_{ts}}$ as a function of the distance of closest approach

Force	$F_{ts}\sqrt{V_{ts}/F_{ts}}$	γ_{1A}
$\frac{C}{s^n}$	$\frac{1}{\sqrt{n-1}}\frac{C}{d^{n-1/2}}$	$\frac{1}{\sqrt{2\pi}}\frac{\Gamma(n-1/2)}{\Gamma(n)}\frac{C}{d^{n-1/2}}$
$C(-s)^m$	$\frac{C(-d)^{m+1/2}}{\sqrt{m+1}}$	$\frac{1}{\sqrt{2\pi}}\frac{\Gamma(m+1)}{\Gamma(m+3/2)}C(-d)^{m+1/2}$
$C\exp(-\kappa s)$	$\frac{C\exp(-\kappa d)}{\sqrt{\kappa}}$	$\frac{C\exp(-\kappa d)}{\sqrt{2\pi\kappa}}$

Notice that in those experiments we are entering the contact region and probing the repulsive part of the tip–sample interaction and Eq. (5.16) still holds. Normalised frequency shifts γ_{1A} for three basic types of tip–sample forces (power law forces $F_{ts}(s) = C(-s)^m$ for $s < 0$ and $F_{ts} = 0$ for $s > 0$ describe Hertzian contact forces ($m = 3/2$) for a spherical tip on a flat surface, and adhesion forces ($m = 0$)) can be found in Table 1 and Appendix A.

5.2.6. Simple expressions for Δf in terms of the force and/or the interaction potential

Experimental FM-AFM images represent the variation in tip–sample distance necessary to keep a constant frequency shift during a scan over the surface. Understanding the observed atomic resolution and designing optimal operation parameters implies to determine which sample properties are actually mapped during these constant Δf scans. With the introduction of the normalised frequency shift $\gamma = kA_0^{3/2}\Delta f/f_0$, we have already separated the parameters of the cantilever dynamics, to conclude that experimental images represent surfaces of constant γ_{1A}. However, γ_{1A} is still a non-local function of d because its evaluation requires the knowledge of the tip–sample interaction over the whole oscillation path.

Nevertheless, it would be highly desirable to have a simple *local* expression that relates γ with the tip–sample interaction at the point of closest approach d. This would be the equivalent of the popular Tersoff–Hamann [165] approximation in STM, which shows that the tunnelling current essentially represents the local density of surface states at the position of the sample. Although not accurate enough to describe *quantitatively* the observed corrugation in most cases, it offers a good qualitative description of the image and, thus, it is a powerful guide for both experimentalists and theorists in the analysis of STM images.

Ke et al. [166] were the first ones to substantiate the fact that Δf had an intermediate behaviour between that of the force and the interaction potential. Their approach, based on the use of the energy conservation to get an expression of the oscillation frequency in terms of V_{ts}, shows that, in the case of large amplitudes, the ratio $\Delta f/\sqrt{|V_{ts}F_{ts}|}$ is very close to a constant in the whole non-contact region, while for small amplitudes (30–60 Å) and $d > 4$ Å, Δf is approximately proportional to the force.

Giessibl and Bielefeldt [163] reached a similar conclusion through his analysis of the large-amplitude normalised frequency shift γ_{1A}. Notice that for the different interactions considered in Table 1 we can define the *range* (or decay length) $\lambda = V_{ts}(s)/F_{ts}(s)$. This quantity has length dimensions, and in the case of an exponential interaction $F(s) = F_0\exp(-\kappa s)$, naturally defines the interaction range: $V(s+\lambda)/V(s) = 1/e$ is independent of tip–sample distance s with $\lambda = V(s)/F(s) = 1/\kappa$.

For inverse-power and power forces, a similar expression $\lambda_{\text{power}} = V(s)/F(s)$ depends on s, but it shows similar scaling properties: $V(d+\lambda_{\text{power}})/V(d) \approx 1/e$ for exponents $n > 1$ ($=1/e$ for $n \to \infty$). Table 1 compares γ_{lA} and $F_{\text{ts}}\sqrt{\lambda} = F_{\text{ts}}\sqrt{V_{\text{ts}}/F_{\text{ts}}}$. Notice that, in all the cases, $F_{\text{ts}}\sqrt{V_{\text{ts}}/F_{\text{ts}}}/\gamma_{\text{lA}} \approx \sqrt{2\pi}$. This relation is exact for exponential forces and quite accurate for power law forces, where the error decreases rapidly with n (10% for $n = 2$ and 4% for $n = 7$).

Since the frequency shift (and γ_{lA}) is a linear function of F_{ts}, we can write γ_{lA} as a linear combination of the different contributions F^i_{ts} to the total tip–sample force

$$\gamma_{\text{lA}}(d) \simeq \frac{1}{\sqrt{2\pi}} \sum_i F^i_{\text{ts}}(d) \sqrt{V^i_{\text{ts}}(d)/F^i_{\text{ts}}(d)} \tag{5.19}$$

This equation provides the link between an experimentally determined quantity like γ_{lA} and the tip–sample interaction at the point of closest approach d. Schwarz et al. [167] reach the same conclusion $\gamma_{\text{lA}}(d) \simeq (1/\sqrt{2\pi})(V_{\text{ts}}(d)/\sqrt{\lambda(d)})$ modelling V_{ts} as two modified harmonic potentials and making use of the energy conservation (see [167] for details).

After this discussion γ_{lA} appears as a powerful tool to interpret the experimental images $z(x, y, \gamma)$. The distance dependence of γ_{lA} for different relevant interactions is described by Eqs. (5.27)–(5.30) and it is plotted in Fig. 38 (see Section 5.3.1). In particular, we can estimate the orders of magnitude involved with the case of a Si tip probing a Si(1 1 1)-5 × 5 surface (see Section 5.3). For $d = 4$ Å (tip–surface distance of closest approach), theoretical calculations [168,169] give $V_{\text{SR}}(d) = -0.9$ eV, $F_{\text{SR}} = -1.75$ nN for the short-range chemical interaction, and $V_{\text{LR}} = -1.9$ eV, $F_{\text{LR}} = -0.8$ nN for the long-range vdW interaction. The corresponding range (decay lengths), determined following Ref. [167], are $\lambda_{\text{SR}} = 0.7$ Å and $\lambda_{\text{LR}} = 5.1$ Å. Then, Eq. (5.19) (or the expression in terms of V_{ts} and λ) leads to $\gamma_{\text{lA,SR}} = -6.3$ (-6.9) fJ m$^{-1/2}$ and $\gamma_{\text{lA,LR}} = -6.2$ (-5.4) fJ m$^{-1/2}$. The determined value for γ_{lA} is in excellent agreement with values extracted from different experiments [144,150]. Notice that more than

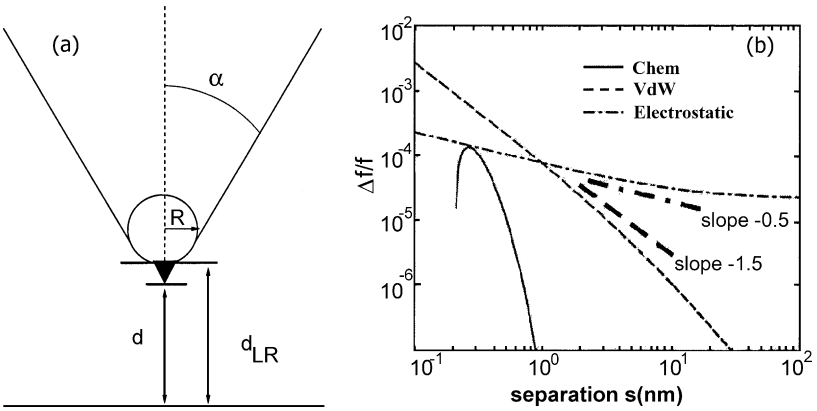

Fig. 38. (a) Model tip geometry: conical mesoscopic tip (α, half-angle of the cone) with a spherical cap (of radius R) and a nanotip at the apex. $d_{\text{LR}} = d + h_{\text{nanotip}}$ is the separation between the mesoscopic part of the tip and the sample at closest approach. (b) Computed distance dependence of the normalised frequency shift γ_{lA} for that tip with $k = 30$ N/m, $A = 20$ nm, $R = 10$ nm and $h_{\text{nanotip}} = 0$. The electrostatic (vdW) contribution scales like $1/d^{1/2}_{\text{LR}}$ ($1/d^{3/2}_{\text{LR}}$) for the distance range 1 nm $< d_{\text{LR}} <$ 10 nm. The parameters in the force laws (Eqs. (5.25) and (5.26)) are $\alpha = 100$, $V_{\text{s}} - V_{\text{c}} = 1$ V, $H = 4 \times 10^{-19}$ J. For the chemical interaction, a Morse potential (Eq. (5.29)) with $U_0 = 2.27$ eV, $d_0 = 2.35$ Å and $\lambda = 0.79$ Å is assumed ((b) after [185]).

50% of the detected value of Δf is caused by the short-range interaction and that variations in the tip–sample distance of 0.5 Å, what represents a typical corrugation measured on the Si(1 1 1)-7 × 7 surface, cause changes of γ_{1A} of ≈5 fJ m$^{-1/2}$, which are easily detectable. Finally, a word of caution about the applicability of these approximate expressions is needed. Although these equations are valid for the typical operation conditions, they lead to inaccuracies for small tip–sample distances (of the order of 2–3 Å) [170,171]. In this case, Eq. (5.18) for γ_{1A} must be used.

5.2.7. Dynamics with a constant excitation amplitude

Several groups [28,29,161,162,172] have approached the theoretical analysis of FM-AFM through the analysis of the cantilever dynamics described by Eq. (5.4) assuming that the excitation of the cantilever is given by a purely harmonic driving force

$$F_{\mathrm{exc}}(t) = kA_{\mathrm{exc}}\cos(\omega_{\mathrm{exc}}t) \tag{5.20}$$

With this choice, what we have is the equation of motion that has been studied in detailed in the first part of this review. This simplification of the real dynamics assumes that one can forget about the dynamical effects of the feedback loop that keeps the self-excited oscillation of the cantilever in FM-AFM, and concentrate on the stationary states accessible to a forced damped oscillator as the final state of the cantilever dynamics (the stationary—steady-state—solutions for the self-driven and the externally driven oscillator are the same [173]).

Although the mathematical approaches are different (a perturbative approach developed by Krilov, Bogoliubov and Mitropolsky [174] in Refs. [161,162,172], and a variational analytical treatment in [28,29]), all of them lead to the following frequency–amplitude relation (resonance curve):

$$A = \frac{A_{\mathrm{exc}}}{\sqrt{1/Q^2 + [1 - \omega^2/\omega_0^2 - r(A)]^2}} \tag{5.21}$$

where $r(A)$ depends on the already familiar average of F_{ts} over an oscillation circle

$$r(A) = \frac{\langle F_{\mathrm{ts}} z\rangle}{kA_0^2/2} \tag{5.22}$$

In a second step, they use the resonance condition to determine ω (as a function of the distance of closest approach d) from the amplitude–frequency curve with the requirement that the vibration amplitude A obtained is equal to the set point A_0 for each distance. The whole distance dependence in Eq. (5.21) is in $r(A)$ and it is easy to see that the maximum value of A corresponds to $A = QA_{\mathrm{exc}}$ and is reached when $1 - \omega^2/\omega_0^2 - r(A) = 0$. This implies that

$$\Delta f = -f_0 \tfrac{1}{2} r(A_0) \tag{5.23}$$

and we recover the result obtained in the perturbative treatment of the conservative dynamics (Eq. (5.9)).

However, differences appear when the stability of the different branches of the resonance curve is considered. The non-linearity of the interaction produces, at some critical tip–surface separation, a drastic change in the analytical resonance curve: it distorts significantly from the usual Lorentzian shape and becomes multivalued (more than one oscillation amplitudes are possible for the given driving

frequency). Sasaki and Tsukada [161] and Gauthier and Tsukada [172] have argued that the state with the larger amplitude—the one located at the extremity needle edge corresponding to the frequency shift $\Delta f = -f_0/2r(A_0)$—cannot be the final steady-state for a cantilever that have started oscillating free and then approaches the surface. If this steady-state is not accessible, one has to redefine the notion of resonance: the resonant state would be the one having the largest amplitude that corresponds to the frequency associated with the inflection in the lower branch of the resonance curve. But, the amplitude of this state is somehow smaller than A_0. In constant amplitude experiments, the driving amplitude A_d would have to be increased in order to reach an state where oscillation with the prescribed A_0 amplitude were possible. In order to evaluate the resonant frequency one has to use the resonance curve to determine the driving signal amplitude A_d which ensures that the resonant state has an amplitude A_0. This leads to a significant departure from the perturbation results for Δf (see Fig. 2(a) in Ref. [172]).

The main objection to this point of view comes from the following two facts: (1) the numerical integration of the proper equation of motion including the feedback loop [157] agrees nicely with the perturbation theory result and (2) experiments [139] show stable operation in areas which should be unstable according to this theoretical analysis. This would suggest that the particular way in which the feedback loop used in FM-AFM keeps the self-maintained oscillation with a fixed amplitude can actually influence the accessibility of the phase space.

A definite assessment of the role of these dynamical bi-stability effects in FM-AFM requires a fully non-autonomous treatment of the real operation of the microscope [173]. In this approach, quantities like A, d, A_{exc} or f are not treated as parameters but as time-dependent variables that evolve towards their steady-state values by the action of the FM-AFM electronics, that has to be properly described and included in the dynamical equations. These complicated simulations have been performed by Gauthier et al. [175] and indicate that there is no significant departure from the perturbation theory result in the case of the frequency shift, although the interplay between the response of the electronics and the non-linear tip–sample interactions can have an influence in the atomic-scale corrugation of the damping signal (see Section 5.6).

Aimé et al. [29,176] also give a word of caution about the possibility of measuring the resonance frequency when the resonance curve is highly distorted. More importantly, they provide an appealing interpretation of the large frequency shifts given by Eq. (5.23), as compared to the predictions of a linear analysis, in terms of one of the most characteristic features induced by non-linear terms: the ability to amplify small changes in the parameter conditions, and in particular, in the strength of the tip–sample interaction. Based on this idea and the fact that the vdW force considered provides a good description of the variation of Δf with the distance, they conclude that there is no need to introduce particular short-range forces in order to explain the experiments. The main criticism to this point of view comes from the fact that even in the case where Δf is largely determined by long-range forces, experiments and theoretical calculations show that the lateral variation is always dominated by short-range forces. These short-range interactions actually benefit from the amplification effect discussed by Aimé et al. to provide the atomic resolution observed in the experiments, as we discuss in the next section.

5.3. What forces are responsible for the atomic contrast?

Most of the theoretical studies of dAFM have focused on the understanding of the main features of the cantilever dynamics under the influence of model tip–surface interactions described by classical

potentials. In particular, simulations of the tapping-mode include long-range (LR) electrostatic and vdW attractive interactions and repulsive contact Hertzian forces that, although quantum mechanical in their origin (quantum fluctuations in the case of vdW and Pauli repulsion in the case of the contact forces), can be described by classical expressions. This description can be appropriate for the analysis of the main features of the distance dependence of most of the experimental results, but cannot provide an explanation for the atomic resolution observed in FM-AFM experiments.

Atomic contrast relies on a significant lateral variation of the tip–surface interaction on an atomic length scale that can only be provided by short-range (SR) interactions. Taking the case of LR vdW, it is difficult to understand how an interaction that it is not dominated by the interaction of the tip atoms closer to the surface but depends on the macroscopic shape of the tip, can provide the lateral resolution needed. A likely candidate to provide atomic resolution on the semiconductor surfaces, where atomic resolution with FM-AFM was first achieved, are the covalent bonding interactions that held these materials together. Both in the semiconductor surfaces and the tip (usually sharp chemically etched Si tips) we can find undercoordinated atoms with unsaturated dangling bonds that can contribute to the total tip–surface interaction and provide atomic resolution. We distinguish these quantum-mechanical chemical interactions from the vdW by the fact that they are related to the overlap of the atomic wavefunctions. It is this dependence with the overlap what explains the exponential variation with the distance and makes it suitable for atomic resolution.

This covalent interaction is frequently approximated by exponentially decaying potentials like the Morse potential. However, a quantitative determination requires ab initio calculations of the tip–sample system that are computationally quite expensive. One can consider the intermediate approach (in computation time and accuracy) provided by classical many body potentials (like Stillinger and Weber [177] and Tersoff [178] potentials for semiconductors and glue or embedded atoms models for metals). These potentials are fitted to reproduce accurately the mechanical properties of the bulk and do a fairly good job describing small distortions from this structure, but its application to calculate the interaction in a completely different environment as the case of a tip and a surface has to be considered with care. Experience in other related problems, like cracks in covalent semiconductors where the advance of the crack is controlled by the breaking of the atomic bond at the crack tip, indicates that all the classical potentials are not able to reproduce even qualitatively the observed behaviour (see [179,180] and references therein). Fortunately, thanks to advances in methodology and computing power, it is possible nowadays to perform ab initio calculations, based on the density functional theory, of the total energy and forces of systems containing hundreds of atoms, large enough to model realistically the SR chemical interaction between the tip and the surface. These calculations for the interaction between a Si(1 1 1) reconstructed surface and an atomically sharp Si tip [168,169], in quantitative agreement with recent LT-FM-AFM experiments [144,146] and direct measurements of the interatomic force gradients in ultra low amplitude AFM [156,181], provide a compelling evidence that these covalent interactions between single atoms are indeed responsible for the atomic resolution in FM-AFM images in the attractive regime (see Section 5.3.2).

These chemical interactions that are controlled by the exponential decay of the wavefunctions manifest in different ways according to the nature of the bonding between tip and sample. In the case of insulators (alkali halides and oxides) and oxidised tips, all the dangling bonds are saturated, but it is the very confined microscopic electric field present around the oxygen tip apex (where a couple of electrons taken from the surrounding Si atoms are located on the strongly localised O 2p wavefunctions) that provides the key to the lateral variation of the interaction. The normal displacements of the surface ions

and the related surface polarisation induced by this strongly localised electric field are responsible for the atomic resolution observed in these materials [182], as discussed in Section 5.3.3.

Finally, we will consider atomically resolved images of Xe atoms on highly oriented pyrolytic graphite (HOPG) [145] and graphite surfaces [183,184], that, in the absence of significant covalent or SR electrostatic interactions, have been interpreted [134,163,183] in terms of SR *dispersion* forces between individual atoms, described by a Lennard–Jones (LJ) potential. The attractive contribution that varies as r^{-6} will provide the lateral variation needed for atomic resolution.

After this general overview, the rest of the section is devoted to describe in more detail the calculations of the SR tip–surface interaction and the comparison with the experiment for the different systems. As LR interactions are always present, we start discussing how the LR electrostatic and vdW contributions can be modelled and separated from the frequency shift versus distance experimental curves.

5.3.1. Separation of interactions in FM-AFM

Considering that the total force acting on the tip F_{tot} is the sum of the different LR and SR interactions: $F_{\text{tot}} = F_{\text{V}} + F_{\text{vdW}} + \text{F}_{\text{chem}}$ and using the perturbation relation between Δf and F_{tot} (Eq. (5.9)) we conclude that the total frequency shift is the sum of the frequency shifts associated with the different interactions:

$$\Delta f = \Delta f_{\text{V}} + \Delta f_{\text{vdW}} + \Delta f_{\text{chem}} \tag{5.24}$$

The contribution Δf_{V} is caused by the LR electrostatic forces, Δf_{vdW} by the vdW interaction, and we have collected all the SR chemical interactions in the term Δf_{chem}.

These different contributions can be singled out by their salient features (range, absolute value, etc.) [185]. In particular, SR and LR forces can be separated by their different characteristic ranges. For distances larger than 1–2 nm only the LR interactions contribute. The electrostatic contribution is quadratic on the bias voltage $F_{\text{V}} \propto (V_{\text{s}} - V_{\text{c}})^2$. It can be eliminated from the total LR Δf by compensating for the contact potential difference between the probing tip and the sample, V_{c}, choosing the applied voltage $V_{\text{s}} = -V_{\text{c}}$. V_{c} can be determined by the position of the maxima in frequency shift versus bias voltage curves. As we can write down theoretical expressions for the LR electrostatic and vdW forces between a mesoscopic tip and the sample in terms of few parameters that depend on the tip geometry (see below), it is possible to fit Δf_{V} and Δf_{vdW} for distances larger than 1 nm. Subtracting the extrapolated LR contributions from the total frequency shift we obtain Δf_{chem}.

LR interactions depend on the detailed tip geometry. Although real tip structures can be expected to be irregular, the LR nature of the interaction suggests that we can try to model it in terms of different well-defined geometries (rod, sphere, cone, etc.) that have different power law dependences with distance (see, e.g., the book by Israelachvili [34] for details). A popular geometry that seems to provide reasonable fits is the conical, mesoscopic tip (half-angle α) with a spherical cap (with radius R) terminated by a nanotip of height h_{nanotip} shown in Fig. 38.

Electrostatic and vdW forces can then be written as the sum of the corresponding interaction between the semi-infinite bulk limited by the surface plane that simulates the sample, and the sphere and truncated cone that modelled the tip, plus a correction term that takes into account the overlap of the sphere and cone:

$$F_{\text{V}} = -\pi\epsilon_0 (V_{\text{s}} - V_{\text{c}})^2 \left\{ \frac{R}{d_{\text{LR}}} + s(\alpha) \left[\ln\left(\frac{L}{d_{\text{LR}} + R_\alpha} \right) - 1 \right] - \frac{R[1 - s(\alpha)\cos^2\alpha/\sin\alpha]}{d_{\text{LR}} + R_\alpha} \right\} \tag{5.25}$$

$$F_{\mathrm{vdW}} = -\frac{H}{6}\left\{\frac{R}{d_{\mathrm{LR}}^2} + \frac{\tan^2\alpha}{d_{\mathrm{LR}} + R_\alpha} - \frac{R_\alpha}{d_{\mathrm{LR}}(d_{\mathrm{LR}} + R_\alpha)}\right\} \tag{5.26}$$

where $d_{\mathrm{LR}} = d + h_{\mathrm{nanotip}}$, with d the tip apex–surface distance, is the separation between sample and the mesoscopic part of the tip at closest approach, $R_\alpha = R(1 - \sin\alpha)$, $s(\alpha) = (1/\ln[\cot(\alpha/2)])^2$, L is the tip length (assumed $\gg d_{\mathrm{LR}}$), and H can be taken, in the absence of specific information about the particular system, as the geometric mean of the Hamaker constants of tip and sample. Notice that for $d_{\mathrm{LR}} < R$, these forces are dominated by the spherical cap contribution, represented by the first term in Eqs. (5.25) and (5.26).

From these expressions the large-amplitude normalised frequency shift $\gamma_{\mathrm{lA}} = (\Delta f/f_0)kA^{3/2}$ can be determined. Assuming that $d_{\mathrm{LR}} < R$ and $A \gg d_{\mathrm{LR}}$ we obtain

$$\gamma_{\mathrm{lA}}^{\mathrm{V}} = -\frac{\pi\epsilon_0 R(V_{\mathrm{s}} - V_{\mathrm{c}})^2}{(\sqrt{2}d_{\mathrm{LR}})^{1/2}} \tag{5.27}$$

$$\gamma_{\mathrm{lA}}^{\mathrm{vdW}} = -\frac{HR}{12\sqrt{2}d_{\mathrm{LR}}^{3/2}} \tag{5.28}$$

The distance dependence of γ for the different interactions with typical values of the parameters is shown in Fig. 38, where the predicted power law dependences are stressed. For comparison, the γ associated with a SR chemical force has also been included.

How well does this approach work in a real experiment? Fig. 39 summarises the application of this procedure to clean Cu(1 1 1) surfaces [185]. The electrostatic contribution to Δf does show the proportionality to the square of the applied potential for all the distances and allows an accurate determination of the contact potential. After elimination of the electrostatic contribution, the vdW and SR chemical interactions can be determined. The resulting Δf can be fitted with the $d_{\mathrm{LR}}^{-3/2}$ dependence with $R = 14$ nm and a size of the nanotip $h_{\mathrm{nanotip}} = d_{\mathrm{LR}} - d$ of 0.3 nm assuming a Hamaker constant $H = 4 \times 10^{-19}$ J. The deviations for $d < 1.2$ nm are due to the SR interaction that can now be

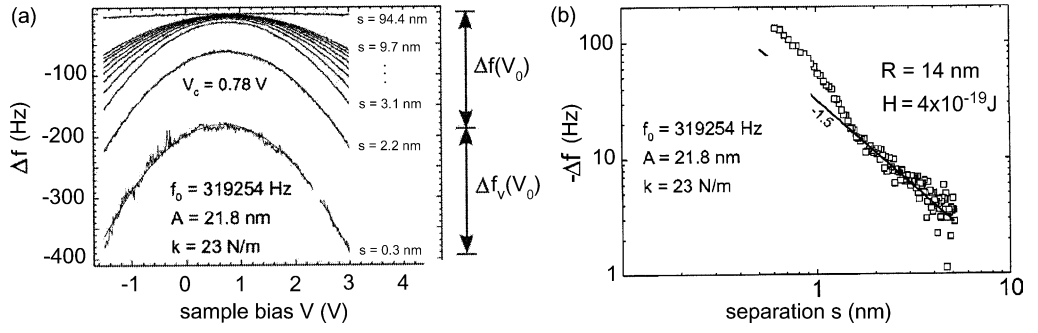

Fig. 39. (a) Voltage dependence of the frequency shift at different distances for a Si tip on a Cu(1 1 1) surface. The lowest curve was measured at a distance where tunnelling current could be collected. The curves taken at $d = s < 1.5$ nm exhibit larger noise due to SR interactions. At larger distances only vdW and electrostatic interactions affect Δf. (b) Least-squares fit of the vdW contribution (no electrostatic interaction is now present as the contact potential is compensated) in the range 1–6 nm, where chemical interactions can be neglected. The best-fit was obtained with $d_{\mathrm{LR}} - d = h_{\mathrm{nanotip}} = 0.3$ nm. The significant systematic deviation from the fit for $d < 1$ nm are due to SR chemical interactions (adapted from [185]).

determined subtracting the vdW fit. This interaction can be described with a Morse potential (known to provide a reasonable description of covalent bonding in a diatomic molecule)

$$U(d) = U_0\left[\exp\left(-2\frac{r-d_0}{\lambda}\right) - 2\exp\left(-\frac{r-d_0}{\lambda}\right)\right] \tag{5.29}$$

where $U(d)$ represents the total bonding energy as a function of the interatomic distance d, and U_0, d_0 and λ are parameters that define the strength, position of the potential minimum, and range of the bonding interaction. As the data does not extend beyond the minimum of Δf_{chem} only the attractive part of the Morse potential is included in the fit

$$\gamma_{\text{IA}}^{\text{chem}} = -\frac{U_0\sqrt{2}}{\sqrt{\pi\lambda}}\exp\left(-\frac{d-d_0}{\lambda}\right) \tag{5.30}$$

This leads to values of the interaction strength $U_0 = 2.35$ eV, with an uncertainty of a factor of 2 due to the assumption of $d_0 = 0$ and $\lambda = 3.4$ Å.

While U_0 is close to what can be expected for the interaction of the closest tip and sample atoms, λ is significantly larger than expected for covalent or metallic adhesive interactions. This has been also observed in semiconductor surfaces [146], where, at large tip–sample separations, the measured SR force and energy decay much more slowly than expected for a purely covalent interaction. These tails have been attributed [146] to local electrostatic interactions (which remain even if the average contact potential has been compensated) caused by the ionic component of the tip apex atom–adatom bond. Due to the different local environments of adatoms and tip apex, the bond formed has a small ionic component. A test charge above the sample would sense and exponentially decaying potential [186] with the longest decay length given by $\sqrt{3}a/4\pi$, with a the lattice constant of the surface reconstruction. In the case of the 7×7 surface, $a = 26.9$ Å, we can expect a decay length of 3.71 Å.

5.3.2. Atomic contrast in semiconductor surfaces from SR chemical interactions

FM-AFM images of the Si(1 1 1)-7×7 reconstruction show the same basic pattern under very different imaging conditions [143,144,146,153,187–190]: twelve protrusions and a deep depression (see Fig. 40), that were already identified in the first experiments [9,11], due to the similarity with the contrast of the empty state STM images of the same surface, with the twelve adatoms and the corner hole in the dimer-adatom-stacking fault (DAS) model [191] accepted for this reconstruction (see Fig. 41). According to this model, there are 19 dangling bonds (associated with the 12 adatoms, the six rest atoms in the second layer, and the corner hole) pointing perpendicular to the surface. These dangling bonds are fully occupied in the case of the rest atoms and the corner hole, while the remaining five electrons are shared by the adatom dangling bonds. Notice that the adatoms fall into four symmetry classes: corner faulted (CoF), centre faulted (CeF), corner unfaulted (CoU) and centre unfaulted (CeU).

Prompted by the experimental achievement of atomic resolution on the Si(1 1 1)-7×7 [9], ab initio simulations were soon performed to study the relevance of the interaction between the dangling bonds in the surface (see Fig. 41) and similar unsaturated bonds in the tip apex as a possible source of atomic contrast in FM-AFM [168,169]. The strong directionality of these orbitals, that have their origin in the sp^3 orbitals that are responsible for the covalent bonding of the solid, suggests that they still have a significant overlap for distances of the order of 5 Å (large for the chemical standards) that can lead to a non-negligible interaction.

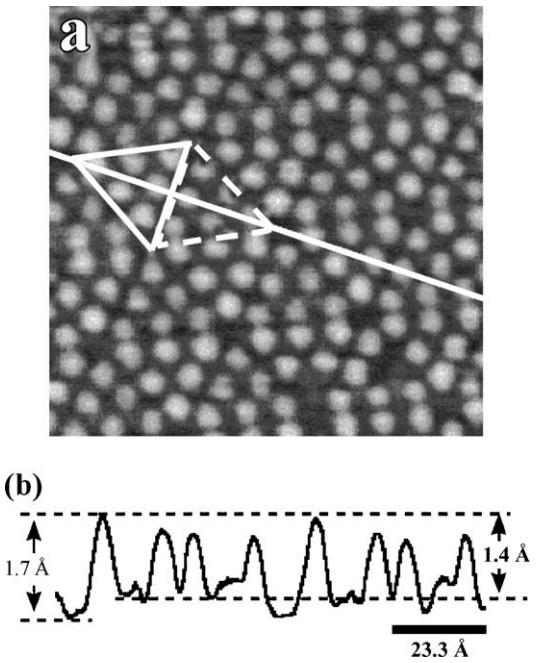

Fig. 40. (a) FM-AFM image of the Si(1 1 1)-(7 × 7) reconstruction at $\Delta f = -28$ Hz ($A_0 = 164$ Å, scan area is 89×89 Å^2). The line profile (b) shows contrast between inequivalent adatoms. The portion of the 7 × 7 unit cell surrounded by the solid (dashed) line corresponds to the faulted (unfaulted) half (adapted from [143]).

These simulations considered a realistic description of the atomic structure of the surface and the tip apex and employed state-of-the-art methods (Density Functional Theory with the Generalised Gradient Approximation (DFT-GGA) for the exchange-correlation energy, in its plane-wave pseudopotential formulation) to calculate total energies and atomic forces in molecules and solids. The surface was described by the 5 × 5 Takayanagi et al. [191] reconstruction, smaller than the experimentally observed 7 × 7 structure, but containing the same basic features: six adatoms, two rest atoms and the corner hole (see Fig. 42(A)), with unsaturated bonds (dangling bonds) pointing normal to the surface. The apex structure of the chemically etched Si tips used in the experiment is represented by sharp Si tetrahedral clusters (the tip end is expected to be bounded by the (1 1 1) cleavage planes of bulk Si). Three different tips (see Fig. 42(B)), with 4 (10) Si atoms stacked in 2 (3) Si(1 1 1) planes were considered. Notice that hydrogen atoms are attached to the Si atoms on the tip base for tips (b) and (c). During the simulations (both lateral scans and approach curves) the relative position of tip and sample is defined by the position of the tip base and the last semiconductor layers. Those parts are held fixed to simulate in both cases the bulk continuation, while the rest of the atoms in the tip and the surface are allowed to relax to their equilibrium configuration for that particular tip position. The sum of the forces on the fixed tip atoms defines the tip–surface force.

Fig. 43 shows the binding energy (the zero is defined as the sum of the total energy of the tip and surface calculated independently in the same unit cell) and the normal force for the different tips scanning at a constant height of 5 Å (the tip–surface distance at closest approach estimated for the experiment [9]) along the long diagonal of the 5 × 5 unit cell. These results show that, although

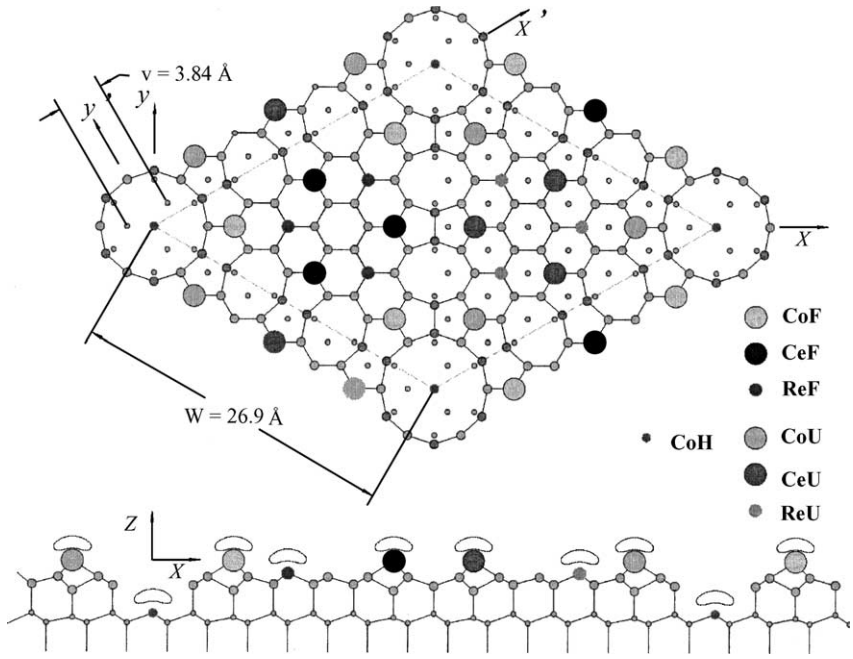

Fig. 41. Ball-and-stick model (top view and cross-section $(y = 0)$) of the DAS fault model of the Si(1 1 1)-(7×7) reconstruction. There are 19 dangling bonds associated with the 12 adatoms in the top layer, six rest atoms (ReF, ReU) in the second layer and the corner hole (CoH). The adatoms fall into four symmetry classes: CoF, CeF, CoU and CeU (adapted from [171]).

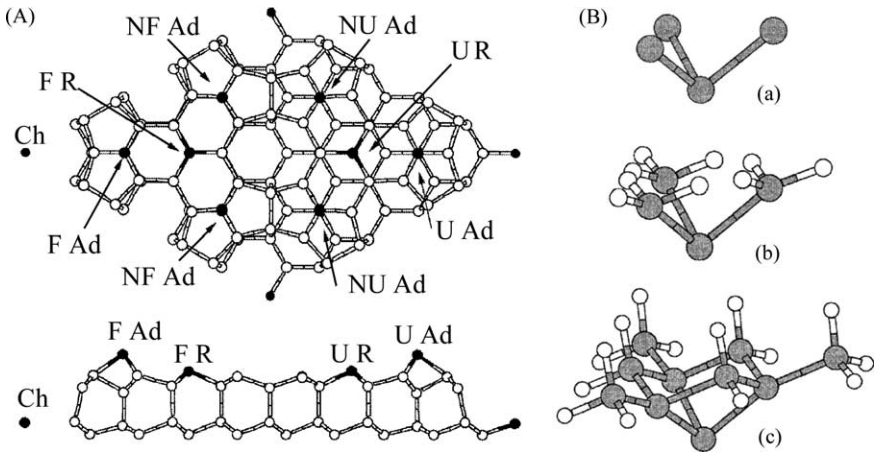

Fig. 42. (A) Top view and cross-section of the Si(1 1 1)-(5×5) reconstruction along the long diagonal. Atoms with dangling bonds are marked: corner hole (Ch), faulted (F R) and unfaulted (U R) rest atoms and the different adatoms. (B) Ball-and-stick model of the tips considered in the calculation. In (b) and (c) the dangling bonds of the Si atoms in the base of the tip are saturated with hydrogen atoms (adapted from [169]).

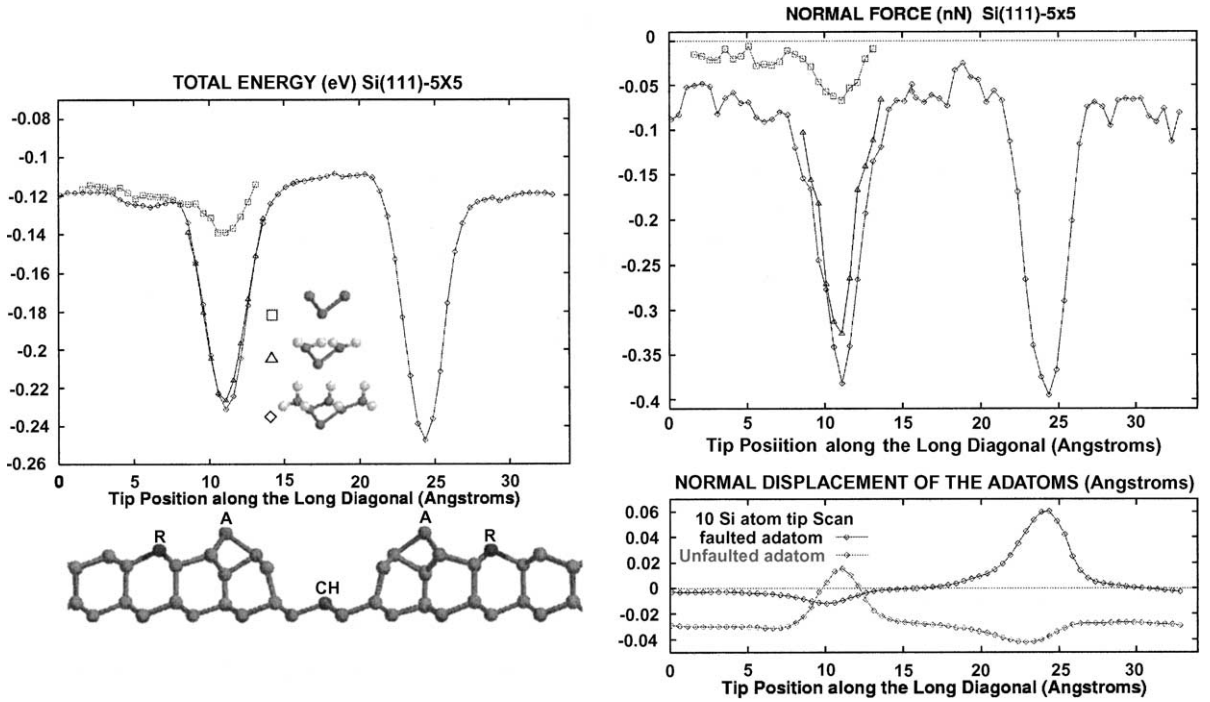

Fig. 43. Total energy (eV) and normal force (nN) for the different tips scanning over the long diagonal in the Si(5×5) reconstruction at a constant height of 5 Å. Notice that all the tips show minima in the energy and force (maximum attraction) at the position of the adatoms, with a larger contrast for the tips with a dangling bond at its apex. The normal displacement of the adatoms during the complete scan with tip (c) is also included (squares [diamonds] correspond to the adatom in the unfaulted [faulted] half of the unit cell) (adapted from [168]).

identical in the geometry, tips (a) and (b) produce significantly different interactions, with a clear enhancement of the contrast (in binding energy and force) for the tips (b) and (c). These differences come from their quite different charge distribution near the apex (see Fig. 2 in [169]). The saturation of the dangling bonds in the base of tip (b) changes the hybridisation of the atom in the apex to a state close to the sp^3 hybrid of the bulk, leaving a dangling bond pointing out of the apex atom towards the surface. The small differences between the two saturated tips (tips (b) and (c)), with a very similar charge distribution at the apex, confirm that the interaction is indeed completely dominated by the interaction of the dangling bond of the tip apex with the surface.

The extended character of the Si dangling bonds is responsible for the onset of covalent bonding at tip–surface distances as large as 5 Å. Further evidence of this bonding comes from other results than can be extracted form the simulations, like the normal displacements of the adatoms (see Fig. 43) and the charge transfer to the adatom dangling bond closest to the tip form the rest of the dangling bonds on the surface (Fig. 2 in [168]). This SR chemical interaction on the adatoms provides, at distances of the order of 5 Å, a force contribution (−0.39 nN) similar to the macroscopic vdW interaction (−0.50 nN for a macroscopic spherical tip with the experimental curvature radius of 4 nm used in the experiments). Its rapid variation both for vertical (large normal force gradients—around 10–12 N/m compared with the 2 N/m of the macroscopic vdW) and lateral tip displacements (it decays rapidly

as we move away from the adatoms) makes it the natural candidate to explain the observed atomic contrast.

Can this mechanism be checked against the experimental evidence? Experiments provide a compelling qualitative evidence of the role of the SR chemical interaction associated with different tip apex structures in the atomic contrast. Several experiments [144,146,163] show the same pattern. Upon first imaging the sample, with a tip not subject to a cleaning procedure—and thus probably covered with a thin native oxide layer—weak atomic-scale contrast was observed. However, with continued imaging, abrupt changes in contrast—after which the individual adatoms were clearly resolved—were observed. These changes probably resulted from the transfer of a few Si atoms from the surface to the tip apex, as already suggested [168] to explain the changes in resolution observed in Giessibl's [9] original images. The different contrast observed with tips subject to different preparation procedures confirms this point [143].

LT-FM-AFM [144,146] overcomes the problems of drift and piezo creep that makes it difficult to reliably position the tip above an specific site position, and provides the way for a *quantitative* confirmation of the role of SR chemical interactions: accurate frequency shift versus distance curves can be determined at specific positions and compared with the prediction of Eq. (5.9) with the tip–sample forces calculated in the simulations. Experimental frequency shifts recorded during constant height scans (Fig. 44(a)) show a rapid increase on top of the adatoms (-50 Hz compared with -2 Hz for the corner hole with a normal displacement of only 0.33 Å). Rest atoms began to be detected when the tip–sample spacing is reduced by 0.64 Å. Similar rapid changes in Δf have been reported in RT experiments [143,192]. These results are consistent with a LR component of the force identical for all sites, and a strong site-dependent SR force responsible for the atomic contrast. The LR vdW component (no LR electrostatic contribution is present as a bias voltage is applied to compensate the measured 1.16 eV contact potential) can be determined considering that above the corner hole site, the tip apex stays relatively far from any of the dangling bonds of the surface and one can assume that Δf comes only from the site-independent vdW contribution. This vdW contribution can be added to the contribution calculated from the SR chemical forces (see the approach curves over different atoms in

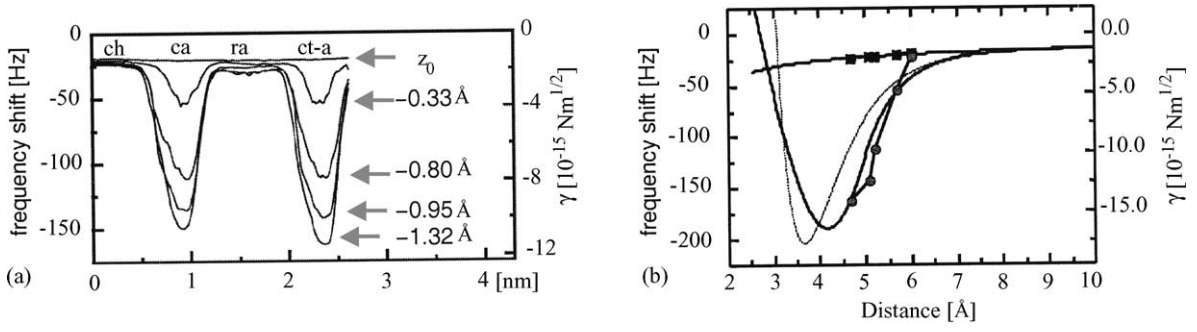

Fig. 44. (a) Line sections taken from a series of constant height scans along the long diagonal of the Si(7 × 7) reconstruction made at progressively smaller tip–sample spacings. A significant Δf develops at the positions of the adatoms. (b) Δf measured over the corner hole (squares) and centre adatom (circles) plotted versus tip–sample distance. The solid line represents the frequency shift calculated, using Eq. (5.9), from the theoretical force versus distance curves in Fig. 45(a)). Relaxation effects play a crucial role in the quantitative agreement between theory and experiment as shown by the thin line where those effects have not been included in the calculation of the frequency shift (adapted from [144]).

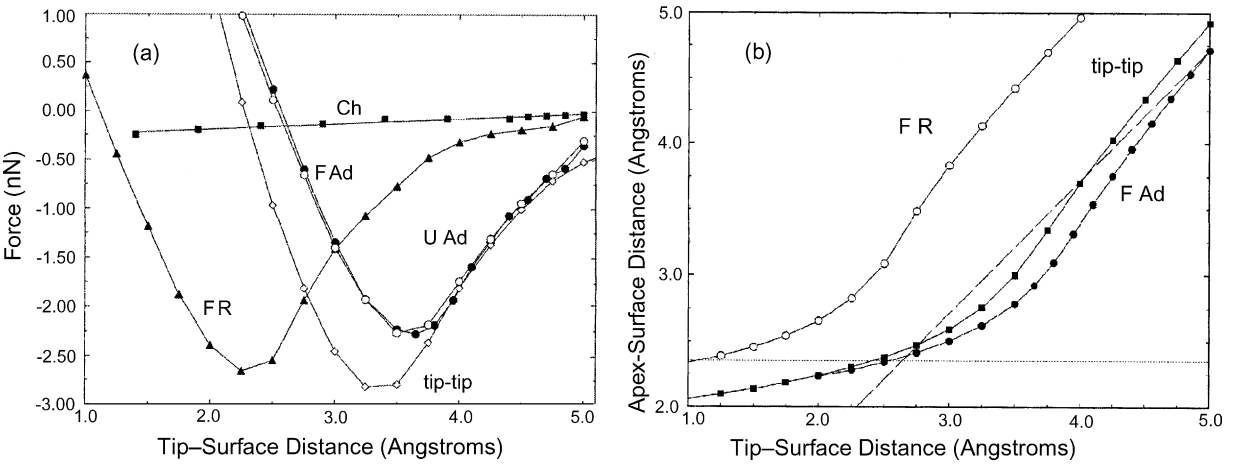

Fig. 45. (a) Normal force versus tip–surface distance for tip (c) (see Fig. 42(B)) over different atoms on the Si(1 1 1)-5 × 5 unit cell. For comparison, the interaction between two tips [tip (b) in Fig. 42(B)] is also shown. (b) Apex–adatom (apex–rest atom) distance as a function of the tip-displacement for tip (c) over a diagonal adatom (black circles) and a rest atom (white circles) in the faulted half of the Si(5 × 5) reconstruction. The apex–apex distance for the interaction between two tips is also shown (black squares). The dashed line shows the apex–adatom distance for the tip (c) over the adatom for a rigid displacement of the tip if no relaxation were allowed starting from the tip configuration at 5 Å. The horizontal dotted line correspond to the nearest-neighbour distance in bulk Si (adapted from [169]).

the surface in Fig. 45(a)) and compared to the experiment (Fig. 44(b)). The quantitative agreement provides a nice confirmation of the role of the covalent chemical forces associated with the dangling-bond interaction.

Notice that simulations unveil an important result that is not directly accessible from the experiment: As the tip–sample spacing is reduced, the attractive force between the closest atoms of the tip and sample results in significant additional displacements of these atoms. These atomic relaxations (Fig. 45(b)) make the actual change in distance between the tip apex and surface atom larger than the experimentally measured tip displacement (directly related to the ''tip–surface distance'', defined as the difference in height between the unrelaxed tip apex and the highest adatom in the unrelaxed surface, that we use in the theoretical simulations). These relaxations play a significant role in the actual distance dependence of the interaction. One can try to fit the calculated forces with Morse potentials (see Eq. (5.29)), but due to the relaxation effects, good fits for the force are only obtained when one takes d as the real apex–surface distance (and not the tip–surface distance). The frequency shift calculated from this fit considering d as the tip–surface distance leads to a significant disagreement between the distance dependence in theory and experiment (see Fig. 44(b)). Thus, quantitative comparisons require theoretical calculations for realistic systems, as these relaxations, that depend significantly on the particular atomic environment, lead to a departure of the tip–surface interaction from a simple diatomic bonding (illustrated by the interaction of a model system formed by two tips) as the tip approaches the surface and the response of the adatom or the rest atom becomes more influenced by the atoms in the layers below. These relaxation effects, already important at 5 Å, have to be taken into account in the interpretation of AFM scans and have been recently considered also for STM experiments [193].

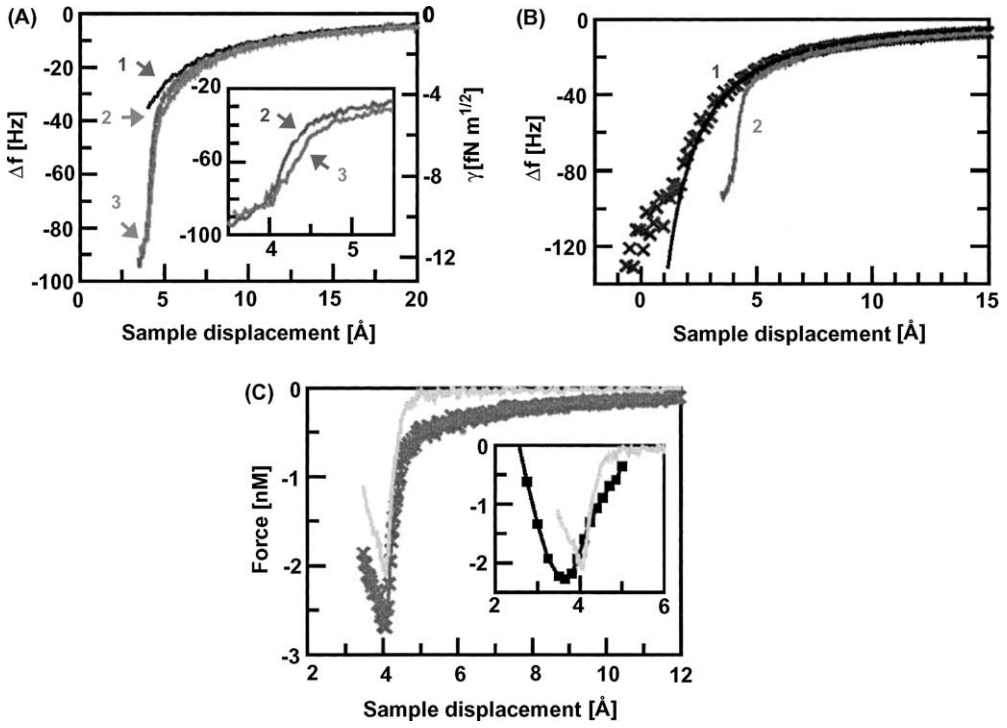

Fig. 46. (A) Frequency shift Δf and normalised frequency shift γ versus distance measured on top of the corner hole (1) and two inequivalent adatoms (2, 3). The inset shows a magnification of the data to give a better picture of the data acquired above the two inequivalent adatoms. (B) Measured Δf compared with the fit to the data using a sphere-plane model for the vdW force. (C) Total force (line with symbols) and SR force determined above adatom 2. In the inset, the measured SR force is compared with the first principles calculation (adapted from [146]).

Refined experiments [146] allowed the determination of the force over a large range of tip–sample distances using site-specific frequency–distance measurements. Fig. 46(A) shows these approach curves for two inequivalent adatoms and the corner hole. Notice that for distances greater than ~12 Å, the data measured above the three sites are virtually identical, while, at small tip–sample distances, Δf measured above the adatoms drops much faster than above the corner hole. The quality of the fit obtained with a sphere-plane geometry $F_{\mathrm{vdW}} = -A_{\mathrm{H}}R/6(z+z_0)^2$ and $A_{\mathrm{H}}R = 9.1 \times 10^{-28}$ J m and $z_0 = 1.0$ Å (see Fig. 46(B)) confirms the assumption that vdW dominates the tip–sample interaction above the corner hole. Notice that the vdW fit (Fig. 46(B)) reproduces the measured Δf over the corner hole for distances of 1.5 Å below the point of closest approach for the adatoms. Beyond that point, Δf actually decreases much less rapidly than predicted by the vdW model, indicating the onset of a strong SR repulsive force (probably a results of the proximity of the mesoscopic oxide tip to the adatoms surrounding the corner hole) and ruling out the presence of other dangling bonds on the tip that can contribute to the SR force measured above the adatoms.

The Δf data measured above the adatoms can then be inverted using the procedure of Dürig (see Section 5.4.3) to determine the force and compared, once the vdW is subtracted, with the simulations for the covalent bond forming between the tip apex atom and the nearest adatom on the surface described above (see Fig. 46(C)). The measured maximum attractive force (−2.1 nN) is in remarkably

good agreement with the calculated force (−2.25 nN). However, in the region where the attractive force increases with decreasing distance, the slope of the measured force is steeper than that of the calculated force, indicating that the relaxation effects in tip and sample are actually larger than those calculated. This is probably due to the finite size 10 Si atom cluster used in the simulations (recall the differences between tips (b) and (c) which are essentially due to the relaxation of the atomic plane (with three atoms) closest to the apex in tip (c) that is kept fixed in the smaller tip (b)), but it could also be related with the different relaxation properties of a small cluster attached to the oxide tip. In the range beyond the maximum attractive force, the slope of the measured force appears less steep than the slope of the calculated force, what is also consistent with additional relaxation effects.

Although similar in the basic features, the different experiments provide different values for the relative heights of the inequivalent adatoms and the corner hole corrugation. A recent DFT structural calculation [194] (that corrects the structural calculations in the mid-1990s [195,196]) predicts a height ordering as CoF > CeF > CoU > CeU, with height differences of $\Delta h(\mathrm{CoF}-\mathrm{CeF}) = 0.05$ Å, $\Delta h(\mathrm{CeF}-\mathrm{CoU}) = 0.05$ Å, $\Delta h(\mathrm{CoU}-\mathrm{CeU}) = 0.01$ Å, with an error bar of ±0.005 Å. The ordering and the height differences compare well with an elaborate LEED analysis (with height differences of 0.04 Å) [197]. Several FM-AFM experiments [143,153,188] reproduce basically this ordering in the observed corrugation, with $\Delta h(\mathrm{CoF}-\mathrm{CeF}) = 0.15$ Å. However, other experiments [144,146,187] show CeF to be higher than CoF adatoms (by 0.17 Å according to [144]). In any case, the experimental corrugation (comparable to STM experiments, and much larger than the theoretical height differences) points out that the observed contrast is not simply determined by the atomic structure of the surface (as reflected in the LEED or total energy calculations). Relaxations due to the tip–sample interaction and electronic effects (e.g. differences in the electronic occupancy) contribute to variations in the interaction potential above the different atomic sites, as shown by the calculated force–distance characteristics and lateral scans due to chemical forces [168,169].

(1 1 0) surfaces on III–V semiconductors provide a tougher test for the resolution capabilities of the FM-AFM. Nevertheless, true atomic resolution was soon obtained in InP(1 1 0) by Sugawara et al. [10,198,199], followed by similar experiments on GaAs(1 1 0) [200] and InAs(1 1 0) [201,202]. All these images show, under typical operating conditions, a rectangular pattern of bright protrusions—elongated along the [0 0 1] direction—as shown in Fig. 47(a) for InAs(1 1 0). At the (1 1 0) surfaces, anions relax upwards while cations relax downwards giving a height difference between the two atoms around 0.7–0.8 Å for InAs, InP and GaAs. This suggests to identify the protrusions with the anion sublattice.

Sometimes, however, two features per surface unit cell are imaged. Fig. 47 shows two examples for InAs [201,202] taken with different cantilevers. The second feature, an additional somewhat darker protrusion in (b) and a depression in (c), is located between the bright protrusions identified with the As atoms, and can be attributed to the lower lying In atoms. The scans show that (b) corresponds to a shoulder ∼0.32 Å above the minima, while in (c), a depression of 0.05 Å—which nearly reaches the level of the minima—appears at the same position. Scans along the As atoms are similar in both cases, but the corrugation amplitudes are quite different: 0.75 Å in (b) and 0.18 Å in (c). The corrugation in Fig. 47(b) is much larger than the one in Fig. 47(a), suggesting a smaller tip–surface distance. Similar results have been recently reported on GaAs(1 1 0) [203]. For relatively small Δf, only one of the sublattices is imaged. However, as Δf, is increased (tip–sample distance was reduced), besides the As sublattice, the Ga sublattice can be also weakly imaged as a shoulder.

Schwarz et al. [202] provide a qualitative argument for these differences in the contrast observed in Fig. 47 in terms of the possible tip contamination, that would change the occupancy of the tip dangling

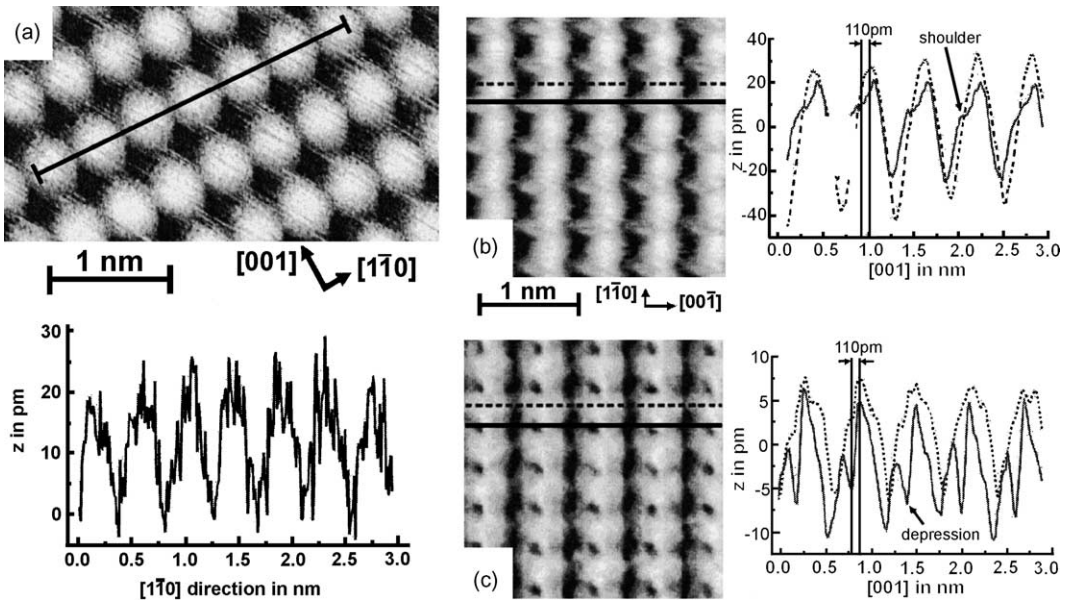

Fig. 47. (a) Atomically resolved InAs(1 1 0)-(1 × 1) as typically imaged in FM-AFM (raw data) with $\Delta f = -55.3$ Hz at LT ($T = 14$ K). Bright protrusions represent the positions of the As atoms. The section along $[1\,\bar{1}\,0]$ shows a corrugation of about 0.20 Å, and demonstrates that the peak-to-peak noise in the z piezo is about 0.1 Å (≈2 pm r.m.s.)in a 2 kHz bandwidth. (b) and (c) represent two examples of FM-AFM images where two features per surface unit cell are resolved. The second feature, an additional protrusion in (b) and a depression in (c), is located between the bright protrusions, where the low lying In atoms should be located. The line sections in the [0 0 1] direction across the bright protrusions (dashed line) and the second feature (solid line) elucidate the different characteristic of the contrast from the As and In atoms. Parameters: (a) $k \simeq 36$ N/m, $f_0 = 160$ kHz, $A = 12.7$ nm, $U_{\text{bias}} = +250$ mV. (b) as (a) with $\Delta f = -37$ Hz and no bias. (c) $T = 78$ K, $k \simeq 38$ N/m, $f_0 = 176$ kHz, $A = 11.0$ nm, $\Delta f = -447$ Hz. $U_{\text{bias}} = -447$ mV (adapted from [202]).

bond. First principles theoretical modelling of these systems (GaAs(1 1 0) in [204,205] and InP(1 1 0) in [158,206]) supports some of these qualitative arguments, explains the characteristic elliptical shape of the protrusions and yields corrugations in good agreement with the experiment (Fig. 48). However, it predicts a contrast inversion in the case of an anion contaminated tip (with a filled dangling bond) that cannot explain the contrast observed in Fig. 47(c).

5.3.3. Atomic contrast in ionic compounds coming from SR electrostatic forces

Atomistic modelling of highly ionic materials like alkali halides and oxides can be done in terms of classical potentials, and thus, it is easier than in covalent semiconductors and metals, where a proper description of the bonding requires the explicit use of quantum mechanics.

Upon formation of these ionic compounds, electron transfer from the cation to the more electronegative species (halogens or oxygen) leaves us with two closed-shell ions, where electrons are tightly bound to each nucleus. The binding properties in these systems result from a competition between the attractive electrostatic interaction of these ions and the Pauli repulsion of the electronic clouds. Due to the spherical symmetry of the electronic distribution around the closed-shell ions, this repulsion, although quantum mechanical in origin, can be well described by classical two-body potentials. The subtle effects of electronic charge redistribution that are responsible for the bonding in semiconductors

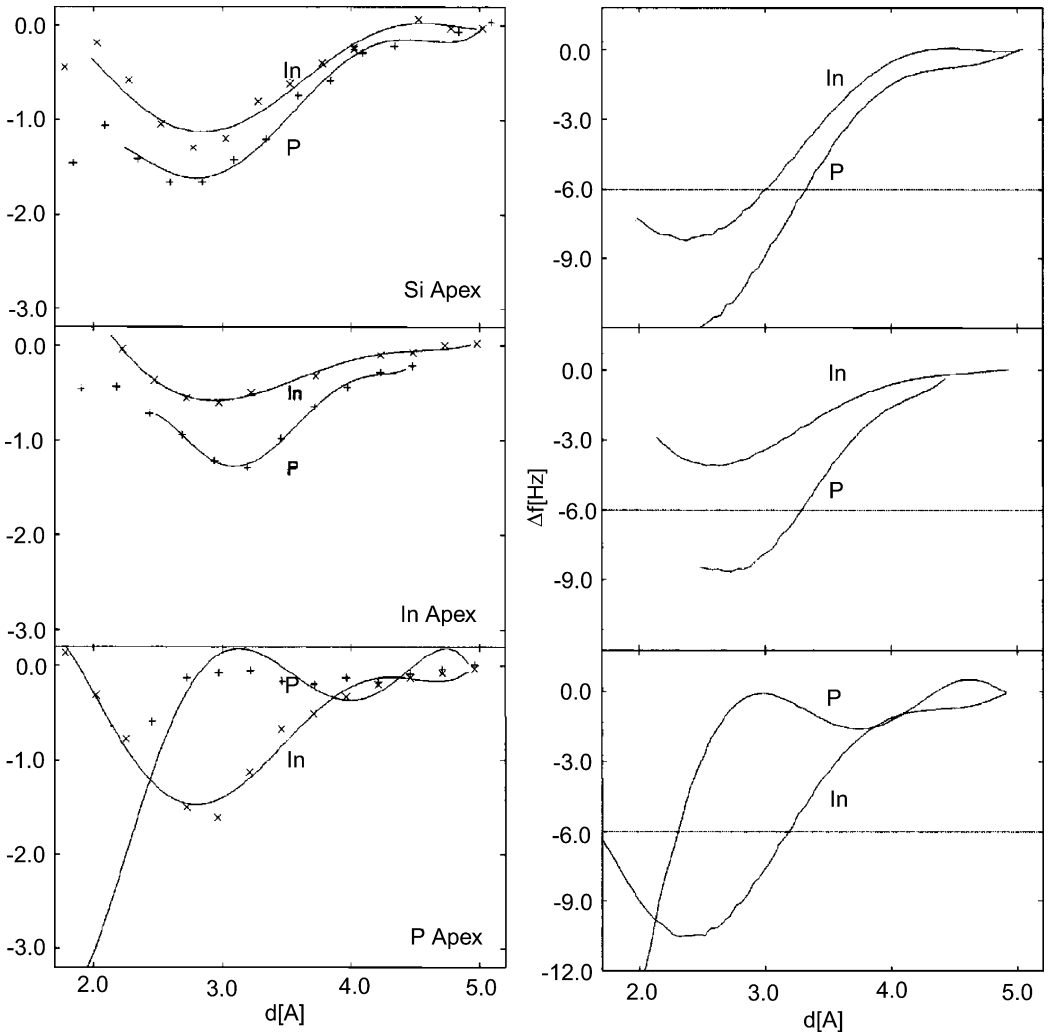

Fig. 48. Results for normal tip–surface forces (left) and frequency shifts (right) versus distance for the Si/Si tip, In/Si tip and P/Si tip over In and P sites on the InP(1 1 0) surface. Experimental parameters were taken from Ref. [10]. The horizontal line at −6 Hz corresponds to the experimental Δf. The wiggles in the curves trough the computed points in the bottom panel are artefacts due to the use of a polynomial fit (adapted from [158]).

and metals—and cannot be embedded accurately in classical potentials (even including three- and four-body terms)—can be reduced in the case of ionic insulators to the electronic polarisation of the ions, that can be described by a shell model, where the total charge of the ion is split between a core and a massless shell that are connected through a harmonic spring. The response of this classical harmonic system to the electric field in the crystal determines the polarisation. All these different classical terms can be fitted to reproduce quantum mechanical calculations for the bulk and small clusters and transferred to study different environments like surfaces and defects.

In FM-AFM imaging of the surfaces of these ionic compounds, we do not have, in principle, significant contributions from dangling-bond covalent interaction due to the presence of closed-shell

ions, and we expect the atomic contrast to be dominated by the interaction of the tip with the alternating electrostatic potential of the surface. (Notice that the cleavage surfaces in these materials are usually non-polar, they contain both anions and cations in the surface plane, and we expect to detect the variation of the electrostatic potential as we move from the cation to the anion.)

Shluger and co-workers [160,182] have modelled the operation of the FM-AFM in different ionic surfaces. LR tip–surface forces (vdW and electrostatics) are included through a model for the shape of the mesoscopic tip as a combination of a cone and a sphere, with parameters fitted to the experimental frequency shift versus distance curves for large separations ($\geq$1 nm) as discussed in Section 5.3.1. Notice that, in the case of a conducting tip interacting with charged structures like a surface di-vacancy or a charged step, or alkali halide films grown on a metallic substrate, another LR force, the electrostatic image interaction, has to be included [207]. The most challenging part is, nevertheless, the modelling of the atomistic part of the tip, close to the apex, that is going to be responsible of the atomic contrast.

A realistic model for the tip would require a Si nanotip, covered with some residual oxide layer, having adsorbed oxygen, hydrogen or water or other impurities coming from the vacuum chamber, and probably contaminated by the surface material. From a computational point of view, one would like to use as a model nanotip a MgO cluster, a hard oxide tip which has the important advantage that there are reliable interatomic potentials for the interaction between MgO and alkali halides and other oxides. As the main contribution to the contrast would come from the electrostatic interaction between the tip and the surface electrostatic potentials, one has to check the ability of the model tip to reproduce the gradients of the electrostatic potential produced at low-coordinated sites in a realistic tip. A study with ab initio methods of different Si clusters with different contaminants [160] shows that pure Si and H-contaminated Si tips are unlikely to have a strong electrostatic interactions with ionic surfaces, while O-contaminated tips (represented by a Si_{10}–O cluster) produce a localised strong potential (due to the low coordination and high ionicity), similar to the one produced by a corner oxygen in a $(MgO)_{32}$ cube (see Fig. 49).

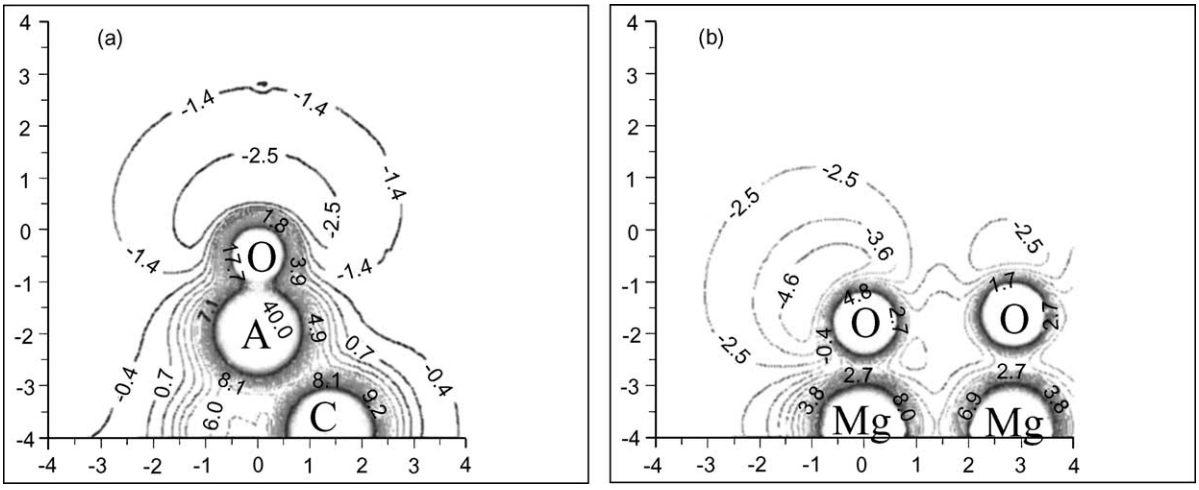

Fig. 49. Sections of the electrostatic potential calculated using first principles DFT methods for (a) an oxygen atom adsorbed on the apex of a Si_{10} cluster (like tip (c) in Fig. 42(B)), and (b) an $(MgO)_{32}$ cube. The scale of the axes is in Å and the units of the contours are in eV. The section is through the apex atom and the oxygen in the Si cluster, and through a plane which includes the (1 1 1) axis and the oxygen tip ion in the case of the $(MgO)_{32}$ cube (adapted from [160]).

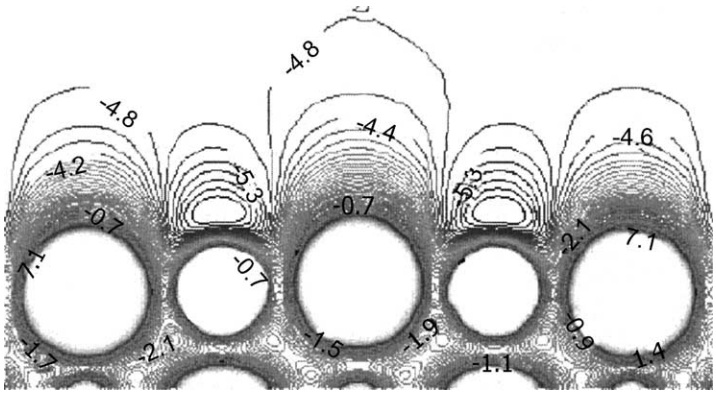

Fig. 50. Sections of the electrostatic potential (in eV) produced by an MgO surface with one Mg ion displaced by 0.15 Å out of the surface (adapted from [160]).

This method was firstly used to analyse the mechanisms of contrast formation in constant Δf scans for the LiF, NaCl and MgO ideal surfaces, and for a Mg^{2+} impurity compensated by a cation vacancy on the LiF surface [160]. These studies reveal that, for distances of closest approach around 5 Å, the main contribution to the contrast comes from the interaction of the tip with the alternating surface potential and with the surface polarisation induced by the localised electric field of the tip. The tip, oriented with the corner O towards the surface, attracts the cations (Li^+, Na^+ and Mg^{2+}), which displace towards the tip (0.07 Å in the hard oxide MgO)—increasing the interaction—and repels the anions (F^-, Cl^-, O^{2-}), displacing them into the surface (0.03 Å for MgO). The total force, including the LR interactions is always positive, but these small changes are actually responsible for the atomic contrast. Both displacements produce dipole moments that give origin to dipole potentials that decay much slower than the exponentially decaying electrostatic potentials of the ideal surface [186] (see Fig. 50 for the case of a Mg ion displaced 0.15 Å out of the surface). Notice that displacing ions outwards from the surface is easier than inwards. Therefore, the interaction of the tip with the induced lattice polarisation above the cation and anion sites is different, what strongly contributes to the image contrast. Due to the small ion polarisabilities of these systems, the polarisation of the surface ions by the tip electric field does not contribute significantly to the contrast. These studies confirm the importance of relaxation effects, that, as we have seen above, also play a crucial role in the proper description of the contrast in semiconductor surfaces.

The {0 0 1} cleavage faces of NaCl [208] and NaF, RbBr, LiF, KI [209] have been atomically resolved using FM-AFM on single crystals cleaved in UHV. Point defects were clearly visible in the images showing true atomic resolution. The mean atomic corrugation (from 0.53 ± 0.19 Å for NaF to 1.54 ± 0.75 Å for NaCl) correlates with the difference between the anion and cation ionic radii (from 0.41 Å for NaF to 0.86 Å for NaCl), except for LiF where it is significantly larger (2.40 ± 1.43 Å for a radii difference of 0.76 Å) [209]. Theoretical modelling predicts corrugations of the same order (0.3–0.7 Å) and helps with the interpretation of the experiments, as shown in the analysis of recent atomically resolved FM-AFM experiments on NaCl films grown on a Cu(1 1 1) surface [210,211]. The analysis of the contribution of the LR forces, where the image force plays a significant role in this case, leads to the prediction that the macroscopic Si tip is insulating and that the thickness of the NaCl layer, that cannot be determined accurately from the topography due to the very different nature of the forces

on the NaCl island and the metallic Cu substrate, cannot be more than 2 ML. Assuming a $(MgO)_{64}$ nanotip terminated in an O atom (as described above), the SR electrostatic chemical forces provide also an explanation for the enhanced brightness at steps and kinks in terms of the enhanced gradient of the electrostatic potential at these low-coordinated sites and the larger displacements of these atoms that further extends the electrostatic potential.

A recent work combining this modelling and experiment has provided, for the first time, an unambiguous identification of sublattices of an insulator imaged by force microscopy [147]. These experiments use an effective constant height mode (instead of the common constant frequency mode), achieved by operating the AFM with a extremely small loop gain for the distance control loop [212–214]. They employed oxide-coated tips brought into slight contact with the surface prior to imaging. The theoretical analysis of the experimental Δf versus distance curves indicates that this method of preparation leads to blunt tips with stable nanoasperities formed probably by surface constituents that provide the best atomic resolution imaging on fluorides [147]. The influence of residual charges was minimised by applying a bias voltage of $+3.3$ V between the conducting tip and the metallic plate supporting the crystal at the back.

Fig. 51(a) shows an experimental image of the CaF_2 (1 1 1) surface taken at an average frequency shift of -126 Hz and a scan line along the [1 2 1] direction. The most remarkable feature of this, an other images obtained under similar conditions, is a triangular pattern with apexes along the [1 2 1] and equivalent directions. The scan shows that the triangular symmetry is due to a secondary smaller maximum, or shoulder, next to the largest maximum. Statistical analysis of the 73 pairs of primary and secondary maxima in 15 scan lines allows a quantitative characterisation of the average distance

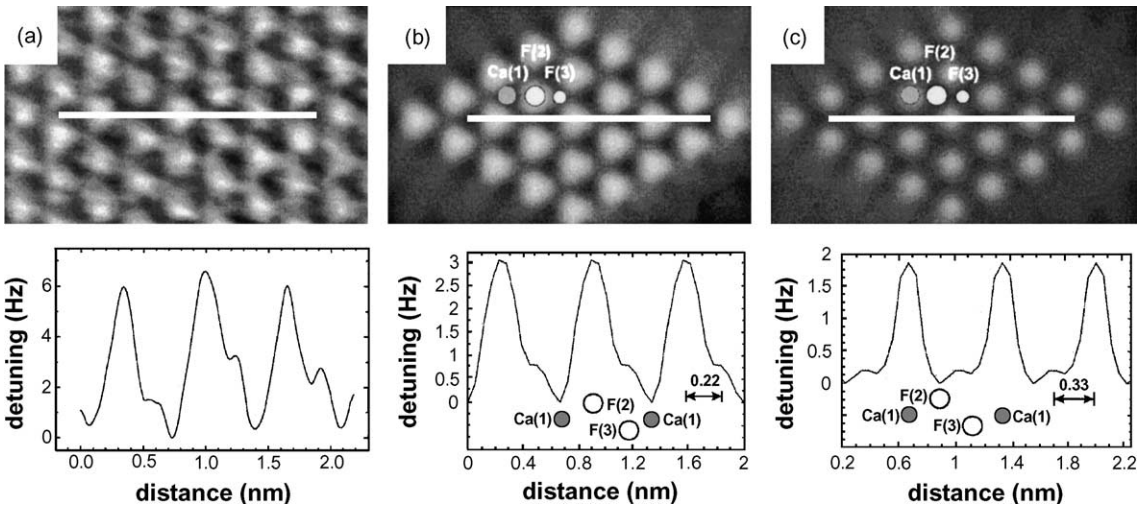

Fig. 51. (a) Experimental FM-AFM image (3.0×2.2 nm^2) and scan line of the CaF_2 (1 1 1) surface taken at constant height with an average frequency shift of -126 Hz. The white line is along the [1 2 1] direction and shows the position of the scan line. The original data has been processed by a low-pass Fourier filter (and in some cases a box reject filter removing stripes parallel to the scanning direction) and the scan is the result of an average over the three equivalent [1 2 1] directions (see [214] for details). (b) Simulated image and scan line produced at constant height of 4 Å (with reference to the Ca sublattice) with a tip with positive potential (Mg^{2+} ion at the apex). The average Δf is -126 Hz. The circles indicate the positions of the outer most fluorine layer (2), the calcium layer (1) and the lower fluorine layer (3). The layers are separated by about 0.8 Å. (c) As in (b) with a negative potential tip (O^{2-} ion at the apex) (adapted from [147]).

between the maxima, 0.25 ± 0.05 nm, and the height ratio, 0.51 ± 0.37 (thermal drift makes it difficult to establish a reference height and reduces the accuracy of the measurement).

The comparison of the experimental and theoretical images stresses the crucial role of the local potential at the tip apex in the observed contrast and provides a way to characterise the tip and to determine the imaged sublattice. Fig. 51(b) shows a simulated image at a tip–surface separation of 0.4 nm (chosen to match the average Δf in the experimental image) with the 64-atom MgO cube nanotip oriented so that a Mg^{2+} ion was at the apex. The theoretical scan reproduces the main features of the experiment—although there is a factor of 2 in the variations with respect to the average Δf—with maxima associated to the strong attraction between the positive potential from the tip and the negative potential over the F^- ions, and minima due to the repulsion at the Ca^{2+} sites. Notice that the secondary maxima, responsible for the triangular symmetry, are related to the interaction with the deeper F^- ions (F(3) in the image). Analysis of the scan lines shows that the distance between the shoulder and the main peak is 0.22 nm and the height ratio is 0.27, in agreement with the experiment. Simulations with a nanotip oriented so that an O^{2-} ion was at the apex and the same tip–surface separation of 0.4 nm give an inverted contrast, with maxima in the frequency shift over the Ca^{2+} ions due to the interaction with the negative potential from the tip, and minima over the F^- ions due to the repulsion of the negative potential over these atoms and the negative tip potential (see Fig. 51(c)). The scans also show a secondary maximum—associated with the weaker repulsion over the deeper F(3) site compared to the protruding F(2) site—between the two F^- ions at 0.33 nm from the main peak. However, this secondary maximum is only 0.11 of the height of the primary maximum and does not lead to a significant triangular distortion of the image.This analysis shows that the apex of the tip used in the experiments had a positive local electrostatic potential that it is imaging the protruding F(2) sites as bright spots, with the deeper F(3) sites producing an elongation of the bright spots that gives the triangular pattern observed. Although most tips are initially oxidised, yielding a negative potential, it is possible that during the preparation, the tip has been contaminated by positive species from the surface. The non-ideal atomic structure of real tips is probably responsible for the systematic differences found in scans in equivalent [1 2 1] directions [214] that limits the quantitative comparison with the theory.

Different oxide surfaces—including NiO(1 0 0) [203], TiO_2(1 1 0)-1 × 1 [215,216] and TiO_2(1 0 0) [217,218]—have been imaged with atomic resolution. The assignment of the structural models to the observed images in the case of the (1 0 0) and (1 1 0) faces of TiO_2 has been based on the assumption that the bright features arise from the most protruding O atoms. Notice that STM with positive sample bias on the TiO_2(1 1 0)-1 × 1 surface images the unoccupied states localised on the Ti atoms and not the O atoms protruding 1.1 Å, as electronic effects dominate over the simple topography.

Simultaneous atomic resolution imaging with FM-AFM and STM under FM-AFM feedback control [219] has recently tried to solve the problem of the assignment of the observed features in the TiO_2(1 1 0)-1 × 1 surface and the controversial structure of the TiO_2(1 1 0)-1 × 2 reconstruction [218,220]. The defects on the bright lines (dark spots in FM-AFM, bright spots in STM) can be assigned to single atom vacancies of the bridging oxygen ridge, with the FM-AFM perfectly tracing the vacancy in the surface topography, and STM imaging the empty states associated with the dangling bonds of the Ti atom underneath (see Fig. 52). The topography of the FM-AFM images of the 1 × 2 reconstruction also seems to follow the true surface topography of the assumed added Ti_2O_3 model.

Notice that this experimental assignment seems to be in contradiction with calculations including electrostatic interactions with an oxygen terminated MgO tip for the TiO_2(1 1 0)-1 × 1 surface [182] that indicate that the SR interaction of this tip is stronger with the Ti rows, and thus, predict the Ti rows

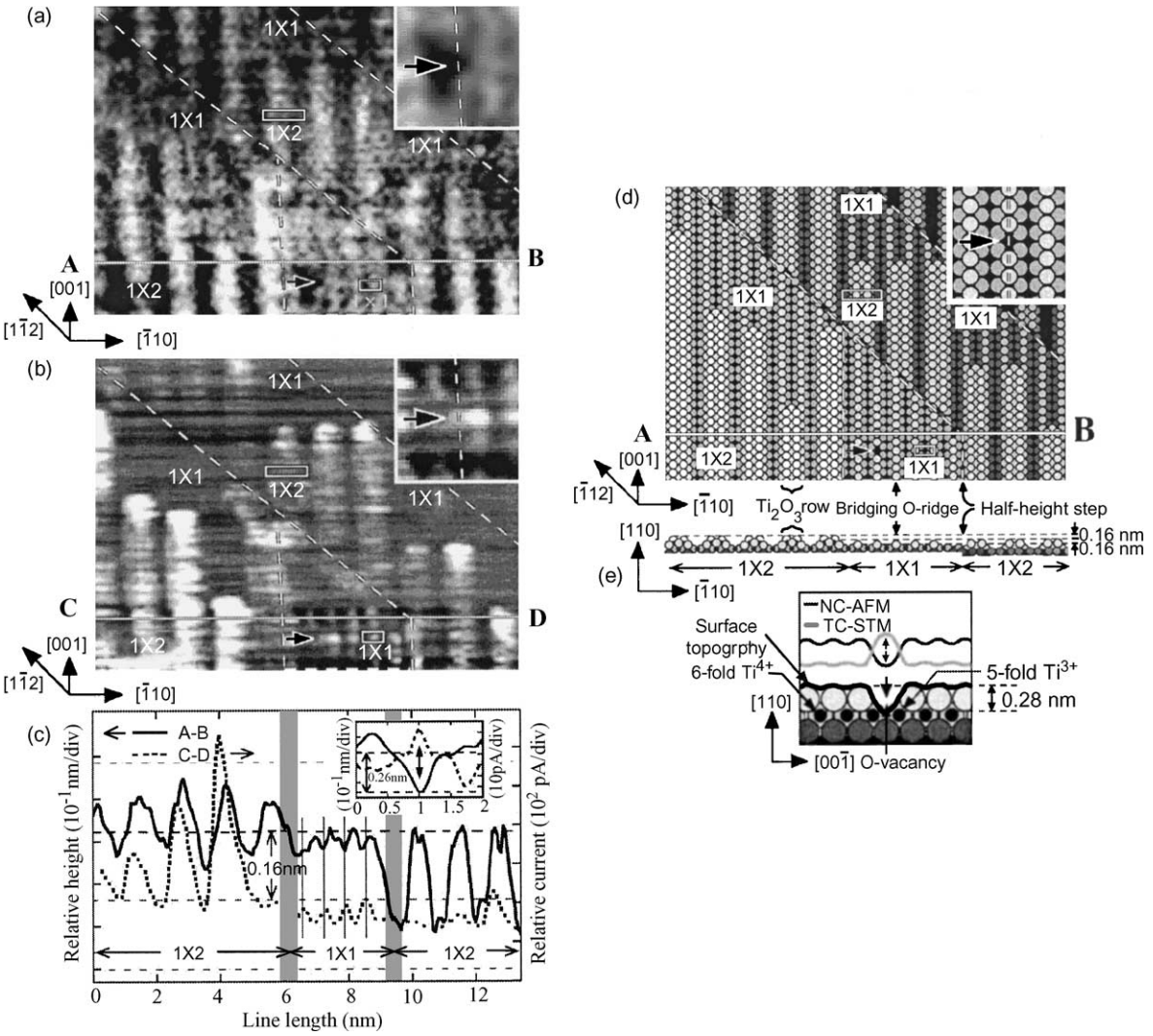

Fig. 52. FM-AFM image of a TiO_2(1 1 0) surface in the topographic mode ($10 \times 14\ nm^2$, $U_{bias} \sim +0.7$ V, $\Delta f = -5$ Hz) including unit cells of (1×1) and (1×2) reconstruction. Inclined broken lines indicate half-height steps along the [1 $\bar{1}$ 2]. The area around the arrow is magnified in the inset. (b) The tunnelling current STM image obtained simultaneously with (a). (c) The cross-sections of lines AB and CD and the dashed lines in the corresponding insets. The corrugation of the STM current is antiphase in (1×1) and in phase in (1×2) with the FM-AFM corrugation, as indicated by the four vertical lines. (d) Model for the area imaged in (a), including the (1×1) and (1×2) areas and the half steps along [1 $\bar{1}$ 2] and [0 0 1]. Large circles (grey scaled according to depth) and small filled circles represent O and Ti atoms. The cross-section of line AB is at the bottom. (e) Cross-sectional model through the dashed line in the inset of (a) (adapted from [219]).

to be seen as bright (O rows as dark) in FM-AFM images. However, very recent ab initio DFT calculations with a clean Si tip [205] show that FM-AFM images the ridge oxygens, in agreement with the experimental observation. Further ab initio simulations, with oxidised tips, are necessary to determine if covalent or electrostatic effects play the dominant role in the formation of the FM-AFM contrast in these surfaces.

5.3.4. Weakly interacting systems: graphite and noble gases

In all the materials we have considered so far, atomic contrast in FM-AFM was the result of relatively strong SR electrostatic or covalent interactions. The forces binding together two graphite (0 0 0 1) planes or a noble gas crystal are significantly weaker and this brings the question whether these surfaces can be imaged with atomic resolution. Allers et al. [183] succeeded in imaging the (0 0 0 1) surface of HOPG and the (1 1 1) surface of a Xe thin film deposited on HOPG [145] using a home-built FM-AFM operating at 22 K.

All FM-AFM images of HOPG exhibit a trigonal pattern of maxima and minima with a distance of 2.46 Å, quite different from the hexagonal structure of the surface. Line sections (see Fig. 53) reveal the presence of two maxima and two minima, separated by 1.42 Å, the nearest neighbour carbon distance. Simulations based on LJ potentials [164,184] show that, in the attractive regime, F_{ts} is larger (more binding) on the hollow (H) sites, in the centre of the hexagons, than above the carbon atoms. This is a characteristic feature of the graphite (0 0 0 1) surface (independent of the chosen parameterisation for the LJ interactions), due to the fact that the tip apex interacts with six nearest carbon atoms if it is located at the H sites, but only with one plus three carbon atoms if it is placed directly above a carbon atom. This leads to an inversion of the contrast in the FM-AFM corrugation: H sites appear as maxima, while the A- and B-type atoms (A-type atoms have a nearest neighbour atom in the layer underneath and B-type atoms not) are imaged as two different minima. The simulated image and scans (see Fig. 53) reproduce quite well the main features of the experiment, including the experimental corrugation, and show that the FM-AFM is able to distinguish between the two inequivalent atoms. Notice that a

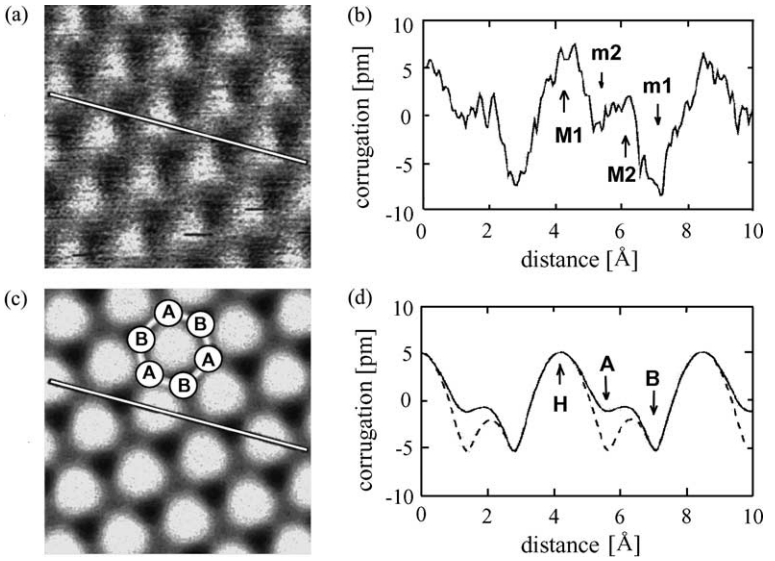

Fig. 53. A comparison between the experimental and theoretical FM-AFM image of graphite (0 0 0 1) (image size: 10×10 Å^2) and their corresponding line sections along the $[1\,\bar{1}\,0\,0]$ direction. (a) Experimental image obtained in non-contact in UHV at LT ($T = 22$ K). Parameters: $k = 35$ N/m, $f_0 = 160$ kHz, $A = 8.8$ nm, $\Delta f = -63$ Hz. (b) The line section demonstrates the existence of two different types of minima and maxima in the image. (c) Simulated image assuming that A and B sites over the surface have a different interaction with the tip. (d) The line section (solid line) reveals that the hollow (H) sites are imaged as the higher maxima, whereas the positions of the carbon atoms appear as the two different minima. Without considering A- and B-type sites inequivalent the line section would look like the dashed line (adapted from [184]).

simulation assuming equivalent atoms ($r_A = r_B = r_0$) yields a scan (dashed line in Fig. 53) were the atoms are imaged as equivalent minima, in disagreement with the experiment.

FM-AFM experiments on a Xe thin film deposited on HOPG [145] show maxima arranged in a structure with sixfold symmetry and a distance between maxima of $4.5 \pm 10\%$, that fits well with the nearest neighbour distance of 4.35 Å in the (1 1 1) surface of FCC Xe. This suggests to identify the maxima with the positions of the Xe atoms (no contrast inversion). The apparent corrugation is about 25 pm, considerably larger than the one found in HOPG. Giessibl and Bielefeldt [163] have analysed theoretically this system using LJ potentials and found a maximal corrugation of 5 pm. They attribute this deviation between theory and experiment to elastic deformations of the sample induced by the interaction with the tip (Xe atoms are pulled out of the surface), in similarity with the early proposal to explain the large experimental corrugations in STM images of Al(1 1 1) [221]. An alternative point of view is suggested by ab initio calculations that show that the interaction of noble atoms with metallic surfaces has a significant component (comparable to the pure vdW) coming from covalent interactions due to the overlap of the Xe 6s orbitals with the metal wavefunctions [222,223]. We speculate that a similar contribution can appear due to the covalent interaction of the tip dangling bonds with the Xe atoms and explain the discrepancies with the experimental corrugations.

5.4. *Inversion procedures: determination of the interaction potential from the frequency shift*

This section addresses different strategies to solve the so-called inversion problem: how to determine the tip–sample interaction from measured frequency shift versus distance curves. Notice that the determination of these potential above specific sites opens the possibility of using the FM-AFM as a spectroscopic technique, with chemical identification capabilities which has been pursued for long time with the STM.

5.4.1. *Inversion through numerical simulations of the cantilever motion*

Gotsmann et al. [157,224] have devised a solution of the inversion problem through numerical simulations of the cantilever motion using Eqs. (5.4) and (5.5). His method is based on the standard mathematical approach to a best-fit problem. A trial force $F_{ts}(s)$ is chosen and a $\Delta f(d)$ curve is calculated introducing that force into those equations. From the deviation of the resulting $\Delta f(d)$ curve with respect to the experimental one a new trial force is derived and the process repeated until the simulated $\Delta f(d)$ curve matches accurately the experiment.

The trick for an efficient implementation of this approach is to avoid the variation of the whole force curve in each iteration and concentrate on the determination of the force in the new tip–sample distance range probed by the tip as we approach it to the surface. As Δf is measured for a finite number of tip–sample distances, the experimental determination of Δf introduces naturally a discretization of the distance in small steps Δd. For each approach step j of the cantilever holder, the tip moves through a part of the potential (given over the extension $\Delta d_j \simeq \Delta d$ for $A \simeq$ constant) which has not been reached in the previous step. The force curve on this "new" part can be linearised if Δd is small. For each step j, the gradient of the force curve is varied on the part corresponding to Δd_j but not altered on the parts $\Delta d_i, i < j$ associated with the previous steps. In this way, the appropriate force curve is determined step by step. The force curves are then a finite set of values determined without any model assumption concerning the properties of tip–sample interactions. The determination of a force curve using this approach takes only 5–10 times the calculation time for the non-inverse problem. Notice that the resulting force curves can

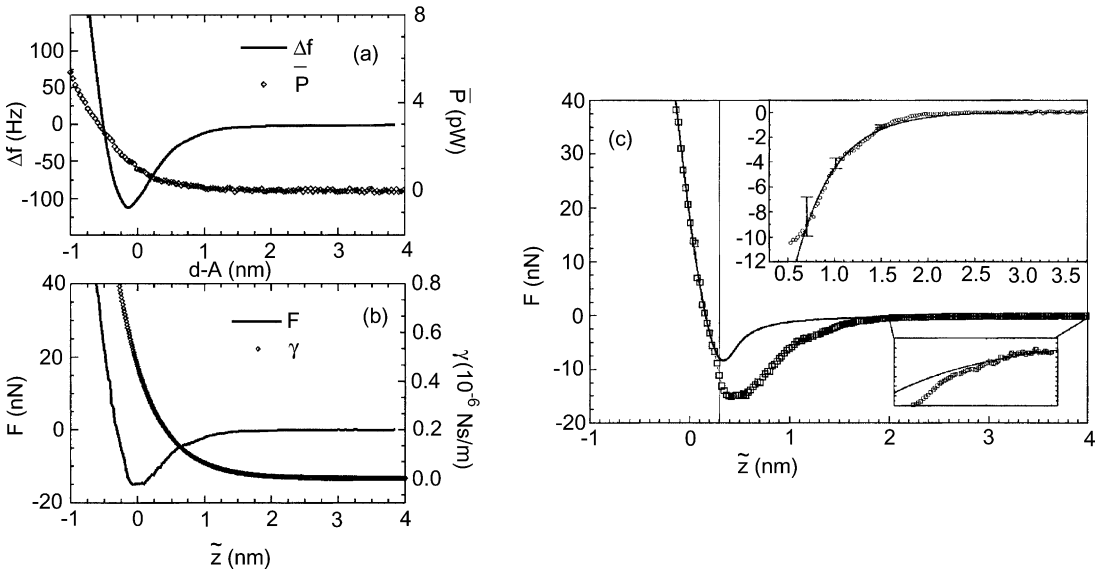

Fig. 54. Frequency shift versus distance for an Al tip on Au(1 1 1) (a). Experimental data. The dissipation power $P(d)$ is calculated using Eq. (5.45). (b) Conservative force F and damping coefficient γ versus distance determined numerically using the procedure described in Section 5.4.1. (c) Reconstructed force curve from Fig. 54 together with a curve from the MYD model. The inset shows the difference between the two curves. Operation parameters: $f_0 = 289\,210$ Hz, $A = 42.5$ nm, $k = 50 \pm 5$ N/m, $Q = 22\,671$. The contact potential (-496 ± 5 mV) is compensated (adapted from [225]).

then be *interpreted* in terms of the models already described for contact forces or attractive forces by fitting of the relevant parameters (Hamaker constant, elastic moduli, tip shape and radius, etc.).

A recent application to the interaction of an Al tip on a Au(1 1 1) surface highlights the capability of the method to detect SR chemical forces [225]. Fig. 54(a) shows the Δf curve measured and the force determined from it (with an accuracy of 0.05 Hz and a discretization of the tip–sample distance $\Delta d = 24$ pm). This force curve can be directly compared with the MYD model [39] as, in this particular case, all the parameters in the model are known (elastic constants for the tip and sample, Hamaker constant) or determined in the experiment (tip radius fitted to measurements of Δf due to electrostatic forces). The determination of absolute tip–sample distances requires a choice of the origin ($d = 0$) that in this case was done in accordance to the repulsive regime of the model. Fig. 54(b) shows that there is an excellent agreement with the model for LR vdW forces as well as in the repulsive regime dominated by the elastic deformation of tip and sample. However, in the attractive SR regime there is a significant difference between the model and the experimental data, that indicates that an additional attractive interaction, which is not accounted for in the MYD model, is sensed. This interaction (see the inset of Fig. 54(c)) shows the exponential decay that one can expect for SR chemical forces, although the decay length, of about 4 Å, is surprisingly large, as already notice in other experiments [185,226] (see the discussion at the end of Section 5.3.1).

5.4.2. *Inversion through the analysis of Δf as a function of the oscillation amplitude*

When the vibrating cantilever is brought close to the sample surface, the potential which determines the oscillation is modified: the effective potential is the sum of the harmonic (parabolic) potential of the

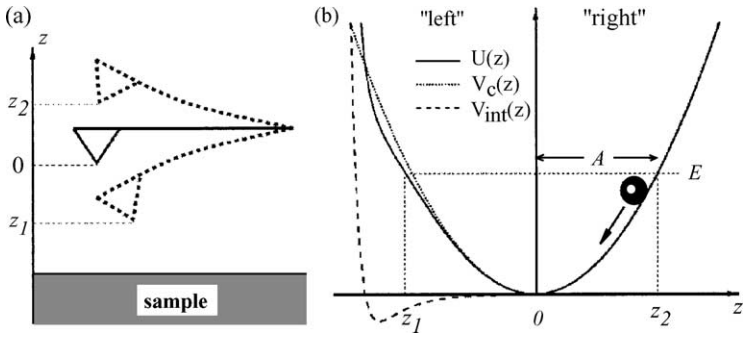

Fig. 55. Definitions used for the inversion problem according to Ref. [227]. The effective tip potential (solid line) is the sum of the parabolic cantilever potential (dotted line) and the tip–sample interaction potential (dashed line). To calculate the tip–sample potential from Δf, it is assumed that the "right" part of the effective potential ($z > 0$) can be replaced by the original parabolic cantilever potential (adapted from [227]).

free CL and the tip–sample interaction potential V_{ts}. This effective potential has an asymmetric shape and the tip oscillation becomes anharmonic: the frequency of the oscillation depends on the amplitude. This is the idea exploited by the method developed by Hölscher et al. [227] to determine V_{ts} from the experimental determination of Δf as a function of the oscillation amplitude.

Energy conservation provides the period of oscillation T in a given effective potential $U(z)$ as a function of the total energy of the system E

$$T(E) = \sqrt{2m}\int_{z_1}^{z_2} \frac{\mathrm{d}z}{\sqrt{E - U(z)}} \tag{5.31}$$

where m is the effective mass of the oscillating system and z_1 and z_2 are the turning points of the oscillation where $E = U(z_1) = U(z_2)$. (Notice that we are taking the origin of z and U at the minimum of the effective potential, see Fig. 55.) This relation cannot, in principle, be inverted to determine $U(z)$ from $T(E)$ because the inverted function $z(U)$ is double-valued. Each value of U corresponds to two different values of z.

However, in the case of FM-AFM, this problem can be solved by considering separately the two regions of the potential $U(z)$ which are located to the left and right of its minimum (see Fig. 55). For typical tip–sample distances, $V_{ts}(z)$ is very small in the right side, and we can assume that the effective potential is given only by the parabolic term: $U(z) = V_{\text{parabolic}}(z) = kz^2/2$ for $z \geq 0$, where k is the CL stiffness.

With this assumption, one can integrate from 0 to z_2 in that equation, to eliminate the z_2 dependence, and get a function $U(z)$ that can be inverted [228] (notice that $U = kA^2/2$ and $E = kA'^2/2$)

$$z_1(A) = -\int_0^A \frac{f_0 - \Delta f(A')}{f_0 + \Delta f(A')} \frac{A'\,\mathrm{d}A'}{\sqrt{A^2 - A'^2}} \tag{5.32}$$

Using the above equation is straightforward to calculate the position $z_1(A)$ from a frequency shift versus amplitude curve $\Delta f(A')$. From this, one can determine the tip–sample interaction potential

$$V_{ts}(z_1) = U(z_1) - V_{\text{parabolic}}(z_1) = \tfrac{1}{2}k[A(z_1)^2 - z_1^2] \tag{5.33}$$

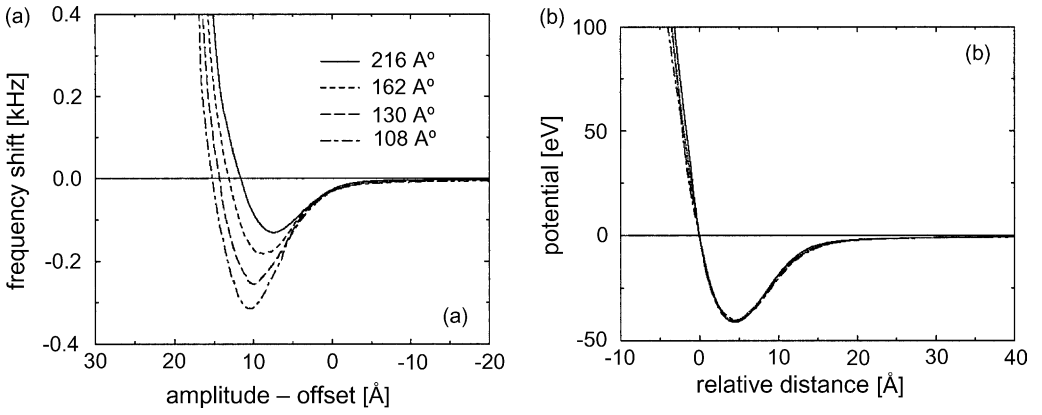

Fig. 56. (a) Four measured $\Delta f(A_{\text{exp}})$ curves recorded in UHV with a Si tip and a graphite sample for various cantilever–sample distances. The curves are individually shifted (with the offset shown in the legend) along the x-axis in order to fit all of them into the same graph. (b) The tip–sample potential calculated from the experimental data shown in (a). Note that all the curves are nearly identical despite the different $\Delta f(A_{\text{exp}})$ curves. The zero point of the x-axis is arbitrarily chosen (adapted from [227]).

Notice that the amplitude measured in an FM-AFM experiment A_{exp} is not the amplitude of the parabolic part A that appears in Eq. (5.32), but both can be easily related

$$A_{\text{exp}} = \tfrac{1}{2}(z_2 - z_1) = \tfrac{1}{2}(A - z_1) \tag{5.34}$$

This can be included in the calculation with a simple search algorithm which varies the amplitude until the condition (5.34) is fulfilled.

The method has been shown to recover accurately the V_{ts} (including both SR and vdW attractive contributions) used to generate a Δf (A_{exp} curve by solving numerically the corresponding equation of motion (see Fig. 2 in Ref. [227]). Fig. 56 shows the application of the method to experimental data for a silicon tip and a graphite sample. $\Delta f(A_{\text{exp}})$ curves have been measured for four different cantilever–sample distances at RT. Notice that, despite the quantitative differences between the curves, the reconstruction of the tip–sample potential using these data leads to identical results. The depth of the measured potential ($\sim$40 eV, much larger than the expected binding energy for a sharp monoatomic tip) indicates either a blunt tip or elastic tip deformations. However, nothing prevents atomic resolution to be achieved with this proposed spectroscopic method if a suitable tip is chosen and the range of the interaction is controlled.

5.4.3. Inversion of the integral equation

Dürig [151,229] has developed an inversion method based on the consideration of the relation between Δf and F_{ts} given by Eq. (5.15) as an integral equation in F_{ts} and the search for its solution in terms of the properties of its kernel. This is the method used by Lantz et al. [144,146] to extract the tip–sample interaction from their LT measurements of Δf as a function of the distance over specific sites of the Si(1 1 1)-7 × 7 (see Fig. 46(C)).

We start from Eq. (5.15) and note that the effective force gradient $k_{\text{ts}}^{\text{eff}} = 2k\Delta f/f_0$ can be written as a convolution product of the force F_{ts}

$$k_{\text{ts}}^{\text{eff}}(z) = \mathscr{A}(F_{\text{ts}}) = \frac{2}{\pi A^2}\int_z^{z+2A} F_{\text{ts}}(s)K_1\left(\frac{s-z}{A} - 1\right)\mathrm{d}s \tag{5.35}$$

with the weakly divergent kernel

$$K_1(u) = -\frac{u}{\sqrt{1-u^2}} \tag{5.36}$$

As usual, s is the absolute tip–sample distance, A the oscillation amplitude and in this section to avoid confusion with the derivatives, we take z as the distance of closest approach (noted as d in the rest of the paper).

The operator $\mathscr{A}$ cannot be inverted in closed form to get F_{ts} from $k_{ts}^{eff}(z)$, but, for SR forces that decay over a distance much shorter than the vibration amplitude, the kernel $K_1(u)$ can be approximated by its leading divergent term at $u = -1$, $K_1(u) \simeq 1/[2(1+u)]^{1/2}$, which yields

$$k_{ts}^{eff}(z) = \mathscr{B}(F_{ts}) \equiv \frac{\sqrt{2}}{\pi A^{3/2}} \int_z^\infty \frac{F_{ts}(s)}{\sqrt{s-z}}\, ds \tag{5.37}$$

This simplified operator can be inverted in closed form [151]

$$F_{ts}(s) = \mathscr{B}^{-1}(k_{ts}^{eff}) \equiv -\frac{A^{3/2}}{\sqrt{2}} \int_s^\infty \frac{(d/dz)k_{ts}^{eff}(z)}{\sqrt{z-s}}\, ds \tag{5.38}$$

In general, F_{ts} includes LR interactions that decay as inverse-power laws and it is not clear to what degree the approximate kernel works. Dürig [229] has studied its performance with a LJ-type force $F_{ts}(s) = F_0(l^4/3s^6 - 1/s^2)$, where l is the distance that corresponds to the maximum attractive force and provides a natural length scale for the interaction. The approximate kernel $\mathscr{B}$ works very well for $A/l \gg 1$ and even captures the qualitative features of k_{ts}^{eff} for $A \sim l$, but fails for small vibration amplitudes, where it should converge to the differential operator $-d/ds$ (see Fig. 2 in Ref. [229]).

Typical operation conditions in FM-AFM correspond precisely to the intermediate regime $1 \leq A/l \leq 10$ (or the $A/l \ll 1$ in the operation with stiffer cantilevers [230]) where $\mathscr{B}$ would yield rather inaccurate results. But the accuracy of the inversion can be improved with an iterative approach that combines both the exact and the approximate kernel

$$F_{ts}^{n+1}(s) = F_{ts}^{n}(s) + \mathscr{B}^{-1}[k_{ts}^{eff}(z) - \mathscr{A}(F_{ts}^{n}(s))] \tag{5.39}$$

One starts with the measured $k_{ts}^{eff}(z)$ and produce an approximate interaction force $F_{ts}^{0}(s) = \mathscr{B}^{-1}(k_{ts}^{eff}(z))$. The corresponding effective force gradient $k_{ts}^{eff,0}(z)$ is then calculated using the exact operator $\mathscr{A}$ with $F_{ts}^{0}(s)$ as the input argument. In general, the measured and recovered effective force gradient functions will not be identical. The difference $k_{ts}^{eff}(z) - k_{ts}^{eff,0}(z)$ is then taken as a new argument in the approximate inversion operator $\mathscr{B}^{-1}$ to calculate a correction term ΔF_{ts} to the interaction force. The process is repeated until consistency is achieved. Dürig has shown the efficiency of this inversion algorithm for the LJ-type force considered above. Two iterations are enough to recover the interaction with a 1% accuracy in the large amplitude limit, and it is still very effective in the intermediate regime $A/l = 1$ were 10 iterations are needed. In general, the algorithm converges for any A/l value for exponentially decaying functions (or a linear combination of them), and its efficiency drops in with $(l/A)^{3/2}$ (i.e., 30 times more iterations are needed for the model force in the case $A/l = 0.1$ than in the $A/l = 1$ case). Similar ideas can be applied to recover the tunnel current from measured dynamic data [229].

5.5. Optimal range of experimental parameters for operation

Suitable operating conditions (cantilever stiffness and frequency, vibration amplitude, tip preparation, Δf set point, bias voltage, etc.) to obtain atomic resolution were determined essentially by trial and error in the first experiments. The "classical" mode of operation is characterised by $k \sim 20$ N/m, $f_0 \sim 100$ kHz, $A \sim 10$ nm, $Q \sim 10^4 - 10^5$ and $\Delta f \sim -10 - 100$ Hz (see Table 1 in [150] for a summary of the early experiments). The theoretical analysis of the previous sections and the large experimental evidence accumulated put us now in the position to discuss, from a more fundamental perspective, the optimal range of parameters for operation with atomic resolution with the best signal-to-noise ratio. Given our conclusion that SR chemical interactions are responsible for the lateral atomic contrast, one would conclude that the enhancement of the sensitivity to these SR interactions should be the goal. Nevertheless, other considerations as operation stability, and the minimisation of the tip and surface damage have to be considered. As a result, there is still a strong debate about the optimal operation conditions. We hope that the analysis below will fulfil the following two goals: First, to provide an account of the possible advantages of operation with very small amplitudes (<10 Å), with special emphasis on the noise reduction, the enhanced sensitivity to SR interactions, and the efficient extraction of the force from the measured Δf. Second, to illustrate the interplay between LR and SR forces in the corrugation observed, and in particular, its role in the understanding of some intriguing results like: (1) the contrast reversal observed under certain operation conditions and (2) the better resolution obtained in some experiments with blunter tips.

5.5.1. Operation with small amplitudes: noise considerations

In FM-AFM a scan across the sample (x–y plane) at constant frequency shift gives us a map $z(x, y, \Delta f, k, f_0, A_0)$ that represents the variation of the normal position of the cantilever z needed to keep Δf constant. Three are the main sources of vertical noise in $z(x, y, \Delta f, k, f_0, A_0)$: mechanical noise, amplitude noise and frequency noise [150]. These sources are statistically independent and thus the total noise is $(\delta z)^2 = (\delta z_f)^2 + (\delta A_0)^2 + (\delta z_{\text{mechanical}})^2$.

Mechanical noise has its origin in the mechanical connection between the cantilever and the sample through the xyz scanner and the coarse positioning system. Acoustic noise, building vibrations, etc. can cause a variation $\delta z_{\text{mechanical}}$ of the distance between the CL and the sample. Proper design of the microscope and insulation from external vibrations help to bring $\delta z_{\text{mechanical}}$ down to a few picometres.

Amplitude noise comes from the thermal vibrations of the cantilever. Thermal fluctuations in the total energy of the cantilever imply fluctuations in the oscillation amplitude δA_0. As $k(A_0 + \delta A_0)^2/2 - kA_0^2/2 \approx k_B T$ (energy fluctuations are of the order of $k_B T$) the amplitude noise is given by $\delta A_0 \approx k_B T / kA_0$. For typical values of operation in FM-AFM ($kA_0 \sim 200$ nN) this contribution is extremely small, even at room temperature where $\delta A_0 \sim 2 \times 10^{-4}$ Å.

Frequency noise, associated with our uncertainty in the determination of the frequency, is the largest contribution to noise under typical operation conditions in FM-AFM. It has two uncorrelated sources: the quality of our frequency detector $\delta(\Delta f)_{\text{instrumental}}$ (typically ~0.1 Hz), and the variations in Δf due to thermal vibrations of the cantilever, $\delta(\Delta f)_{\text{thermal}}$, that was already calculated (see Eq. (5.3)) by Albrecht et al. [3].

In order to relate the frequency noise with the vertical noise, we have to use that a variation δd in the distance of closest approach will lead to a variation in the frequency shift given by $\delta(\Delta f) = (\partial \Delta f / \partial d)\delta d$.

Thus the vertical noise is given by

$$\delta z_f = \delta d = \frac{\delta(\Delta f)}{\partial \Delta f / \partial d} \tag{5.40}$$

that depends on the characteristics of the tip–sample interaction.

To get a final expression for the frequency noise we have to calculate the derivative of Δf with respect to the closest approach distance. This requires a knowledge of the real tip–sample interaction. Giessibl et al. [150] has explored typical noise values assuming different inverse-power and exponential interactions to model F_{ts} and obtained

$$\delta z_f(d) = \frac{k}{F_{ts}^{max}} M(d) \sqrt{\frac{k_B T B}{\pi Q_0 k A_0^2 f_0}} \tag{5.41}$$

where $F_{ts}^{max} = \max(-F_{ts})$ and $M(d)$ depends on the model force considered (e.g., $M(d) = 2\lambda^2(1+\sqrt{\pi/2}(A_0/\lambda)^{3/2})$ for $F_{ts}(z) = F_0\, e^{-z/\lambda}$). Notice that the noise is proportional to $1/F_{ts}^{max}$ and $1/\sqrt{f_0}$, i.e. larger attractive forces and higher frequencies make it easier to achieve atomic resolution.

In order to ensure operation stability, CL stiffness k cannot be chosen independently from the amplitude A_0. Jump-to-contact can be avoided taking either $k > \max(-\partial^2 V_{ts}/\partial d^2) = k_{ts}^{max}$ or $kA_0 > F_{ts}^{max}$. These two conditions can be merged to

$$k = s \frac{F_{ts}^{max}}{A_0 + (F_{ts}^{max}/k_{ts}^{max})} \tag{5.42}$$

with a "safety factor" $s > 1$.

Fig. 57(a) shows calculated noise for the different model interactions as a function of the oscillation amplitude (CL properties considered: $Q_0 = 10^4$, $f_0 = 100$ kHz, $B = 1$ kHz, $T = 300$ K and $\delta(\Delta f)_{instrumental} = 0.1$ Hz). k is determined through Eq. (5.42) taking $s = 100$ (representative of FM-AFM experiments). Notice that minimum noise corresponds to really small amplitudes, $((A_0/d) \sim 1)$ for all the cases considered. This implies that k is in the range 500–3000 N/m for the different model forces. Compare this with the typical operation parameters in FM-AFM $k = 10$ N/m and $A_0 = 100$ Å.

The tip–sample interaction has so far been considered as non-dissipative. However, experiments have shown significant damping of the CL when it oscillates close to the surface. Dissipation processes in FM-AFM are still under debate (see Section 5.6), but Giessibl has discussed the effect of dissipation on the optimum operation using a simple model, where $F_{diss}(z) = -\mu F_{ts}(z)$ independent of the velocity. One can then estimate the energy loss per oscillation cycle as $\Delta E_{ts}(d) = 2\mu[V_{ts}(d + 2A_0) - V_{ts}(d)]$. This energy loss diminishes the quality factor (Q_0) of the CL. Since $Q_0 = E/\Delta E_{CL}$, where $E = kA_0^2/2$ is the total energy in the CL and ΔE_{CL} the energy loss due to internal friction in the cantilever, we can define the effective Q

$$Q = \frac{E}{\Delta E_{CL} + \Delta E_{ts}} = \frac{Q_0}{1 + (2Q_0 \Delta E_{ts}/kA_0^2)} \tag{5.43}$$

Vertical noise is then given by Eq. (5.41) replacing Q_0 by this effective Q. Fig. 57(b) shows the noise once dissipative effects are considered, with $\mu = 0.05$ taken from the analysis of dissipation for a silicon tip interacting with potassium chloride measured by Bammerlin et al. [208]. Notice that larger amplitudes are required for minimum noise, as we could expect from Eq. (5.43), where the reduction of Q due to dissipation can be compensated using large amplitudes.

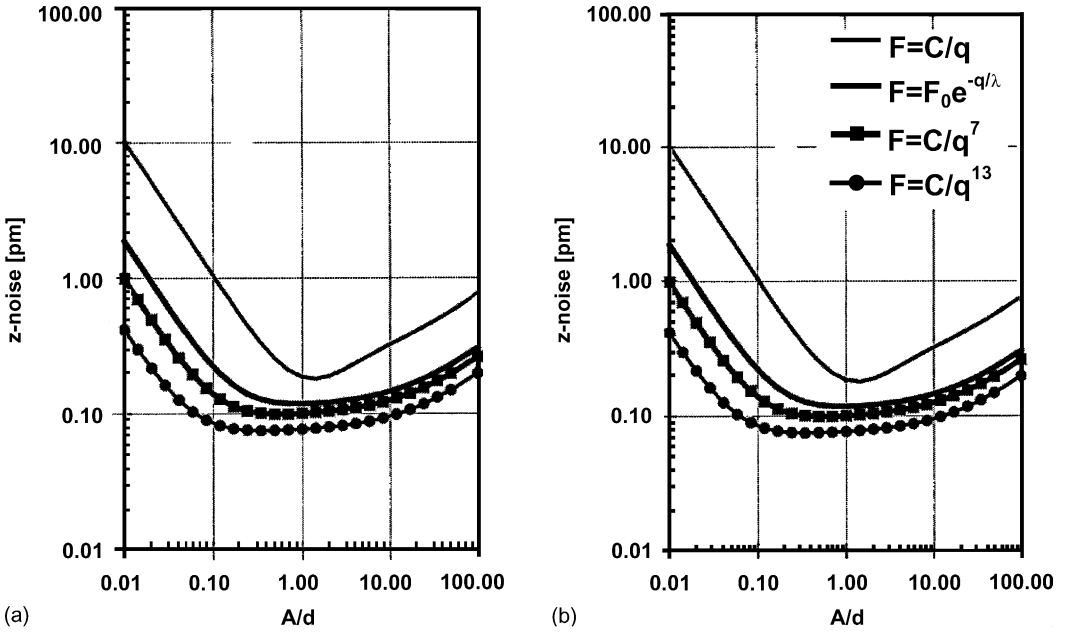

Fig. 57. (a) Calculated noise in sample topography as a function of the oscillation amplitude for exponential and inverse-power force models. (b) As (a) including the effect of dissipation (adapted from [150]).

These results suggest that operation with minimum noise can be achieved with amplitudes in the Å-range and k of the order of hundreds of N/m. Giessibl has achieved atomic resolution on the Si(1 1 1)-7 × 7 with a force sensor based on a quartz tuning fork [230]. The tuning fork has a theoretical $k \approx 1800$ N/m and $f_0^{\text{bare}} = 32\,768$ Hz, that reduces to 15–30 kHz once the tungsten tip is attached to it. The imaging parameters used in his experiments were $\Delta f = -160$ Hz, $f_0 = 16\,860$ Hz, $A = 8$ Å, acquisition speed 4 lines/s (80 nm/s), and the operation was stabilised (see below) with a sample bias +1.6 V. The r.m.s. frequency error $\delta\Delta f$ is 9 Hz. In this way, he was able to obtain images with a very good vertical resolution, such that the height differences of the four types of adatoms were clearly resolved and corner holes were very deep in comparison to previous FM-AFM images [153].

5.5.2. *Operation with small amplitudes: force inversion*

Operation with small amplitudes, of the same order as the range of the tip–sample interaction, offers the possibility to reconstruct the force field, in the distance interval probed by the tip, from a single-shot experiment. Our discussion starts from the Fourier analysis of the tip motion presented in Section 5.2.3. Let us recall that the tip motion can be written as a Fourier expansion with amplitudes a_n given by the correspondent weighted moments of the interaction force (see Eq. (5.14)). The orthogonality of the Chebyshev polynomials $T_n(u)$ allows, in principle, to reconstruct the force in terms of the a_n

$$F_{\text{ts}}[d + a_1(1+u)] = \sum_{n=0}^{\infty} f_n(d, a_1) T_n(u) \quad \text{with} \quad f_n(d, a_1) = a_n(d, a_1) k \left(1 - \frac{n^2\omega^2}{\omega_0^2}\right)$$

In large-amplitude dynamic force sensing, where the interaction is probed only at the very extreme of the tip oscillation at closest approach, a large number of coefficients, determined with great precision,

are necessary to represent SR forces, and is more effective to use one of the inversion procedures discussed in Section 5.4.

On the contrary, if the oscillation amplitude is of the same order of magnitude as the range of interaction the Chebyshev series converge rapidly. Dürig [152] has shown that a Morse-type force $F_{ts}(s) = F_0[\exp(-2s/l) - \exp(-s/l)]$ can be reconstructed fairly accurately with just four coefficients $f_0, \ldots, f_3$ that can be determined in a single experiment by lock-in techniques: $f_0 = ka_0$ from the average lever deflection a_0, $f_1 = k_{ts}^{eff} = 2ka_1\Delta f/f_0$ from the frequency shift, and $f_2 = -a_2(3k + 4k_{ts}^{eff})$ and $f_3 = -a_3(8k + 9k_{ts}^{eff})$. Although the details of the force close to the turning points are not very well reproduced (a typical problem of this kind of expansions), the position of the force minimum (the adhesion maximum) can be efficiently determined in a single experiment. This instantaneous determination of the force can be exploited to extend the spectroscopic capabilities of the AFM (distinguishing between different chemical species) and to provide a more stable operation through the determination of the local minimum of the force curve.

5.5.3. *Interplay between LR and SR forces in the observed contrast*

One additional complication of AFM versus other probe techniques like STM is that the imaging signal in AFM is not monotonic with respect to the distance. The tunnelling current increases monotonically with decreasing tip–sample distance. However, the SR tip–sample chemical force, increases rapidly for tip–sample distances below 5 Å until it reaches a minimum (maximum attractive force) where it starts decreasing with distance and becoming repulsive (see Fig. 45). This non-monotonic behaviour reflects in the frequency shift, that changes the sign of its derivative in a very small distance range. As topographic images in FM-AFM use the frequency shift as the feedback signal, stable feedback is only possible on a monotonic branch of the frequency shift curve. That implies that the region where stable operation with atomic resolution in the attractive regime ($d\Delta f_{SR}/dz > 0$, positive slope) reduces to ≈2 Å range in the tip–sample distance.

LR interactions (electrical or vdW) have a monotonic behaviour that can be used to extend the range of stable operation. Notice that the condition we have to fulfil is $d\Delta f/dz > 0$ with $\Delta f = \Delta f_{SR} + \Delta f_{LR}$ (positive slope of the *total* frequency shift). Large enough LR forces can compensate the decrease of Δf_{short} beyond its minimum and provide a wider range of stable operation. This is the case in the experiments of Giessibl on the Si(1 1 1)-(7 × 7) with a tuning fork [153,230,231], where the electrostatic force supplied by a 1.6 V bias voltage between tip and sample provides the background force necessary to keep $d\Delta f/dz > 0$ for distances close to 2.35 Å, where the SR force is already significantly repulsive.

The interplay between the background forces and the SR chemical contribution also lies behind the contrast reversal (adatoms appeared lower than corner hole) with bias voltage observed in some experiments on the Si(1 1 1)-(7 × 7) [232,233]. In this case, the background forces become so strong that one can probe in a stable way the region of strong repulsion in the chemical force on top of the adatoms while the total force on the tip is still attractive and decreases (becomes more attractive) with distance.

Nevertheless, one has to be careful with this strategy, because, as noticed by Lantz et al. [144] in their study of the Si(1 1 1)-(7 × 7), a LR background interaction (vdW in their case) tends to reduce the measured corrugation. The reason is that this interaction would give a contribution Δf_{LR} that is essentially site independent but distance dependent. When the tip is on top of one of the lower atoms in the surface it has to get closer in order to reach the frequency shift set point. That distance would be

smaller than the one due solely to SR chemical forces due to the distance variation of the LR force, and this effect reduces the corrugation that one would expect on terms of the site-dependent SR forces. If the LR force is large compared with the chemical contribution to Δf the corrugation will be significantly reduced, and can, eventually, be inverted. This highlights the importance of tip sharpness (to minimise the vdW contribution) in order to improve the corrugation, at least in the ''classical'' FM-AFM operation. It is possible that in the approach followed by Giessibl, the increased sensitivity to SR forces due to the small amplitude can still provide significant atomic corrugation with relatively large background forces.

The interplay of these effects may be dependent on the material under study. During imaging of insulators, several groups [147,209] have noticed an increase in corrugation after a series of tip crashes with the surface. The large frequency shifts obtained after the crash indicate a rather blunt tip, but it is possible that, in these materials, the tip retain a stable atomic-size asperity as its apex. This tip would benefit from the possibility of stable operation at closer distances and the ability of the atomic-size structure at the apex to sense atomic size features to produce a higher corrugation.

5.6. Damping

5.6.1. Dissipative forces in NC-AFM operation: experimental characterisation

During operation of the AFM in contact mode dissipation takes place: a part of the work done by the forces is converted into heat. Stick-slip processes, where a lateral force is built up while the tip sticks to an atomic site, are thought to be the microscopic origin of dissipation. When the tip finally slips to a new relaxed position the stored energy is released instantaneously compared to the time scale of most experiments and converted into phonon and electronic excitations, and irreversible changes in the surface. The mean power dissipation in these experiments is $\bar{P} = \bar{F}_{\mathrm{L}} v$, where $\bar{F}_{\mathrm{L}}$ is the mean lateral force and v the scan velocity. Recent atomic-scale friction experiments, at $v = 50$ nm/s, have found as typical values $\bar{P} = 1.2 \times 10^{-16}$ W on Cu(1 1 1) [211] and $\bar{P} = 0.2 \times 10^{-16}$ W on NaCl(1 0 0) [234].

However, dissipation also occurs in non-contact modes of force microscopy, where the atomic structure of tip and sample are reliably preserved. The analysis of the resonance of an oscillating cantilever with a metallic tip in electrostatic interaction with a semiconducting sample by Denk and Pohl [235] provided the first experimental demonstration. In this experiment, the cantilever oscillation was damped by Joule dissipation of charge carriers, which were moved by the oscillating electric field produced by the tip vibration. Recently, Stowe et al. [236] demonstrated the dependence of electrostatic damping, also close to a semiconducting surface, on bias voltage, dopant concentration and tip–sample distance.

FM-AFM has opened the possibility to measure the atomic-scale variation of the dissipation, as shown for the first time by Lüthi et al. [189] on the Si(1 1 1)-7 × 7 surface, where an inverted contrast with atomic resolution—with the strongest damping on the corner holes—was obtained (see Fig. 58). Remember that in FM-AFM the oscillation amplitude is kept constant by a feedback loop that determines the amplitude A_{exc} needed to excite the piezoactuator. When the cantilever oscillation is damped due to the tip–sample interaction, A_{exc} will increase to maintain the oscillation amplitude constant. By recording A_{exc} while varying the tip–sample distance or scanning over the surface we can obtain information on the distance dependence or the atomic-scale mechanisms responsible for the dissipation contrast. Notice that, while the LR electrostatic damping by Joule dissipation is well established, the SR contributions responsible for the atomic contrast are still under debate.

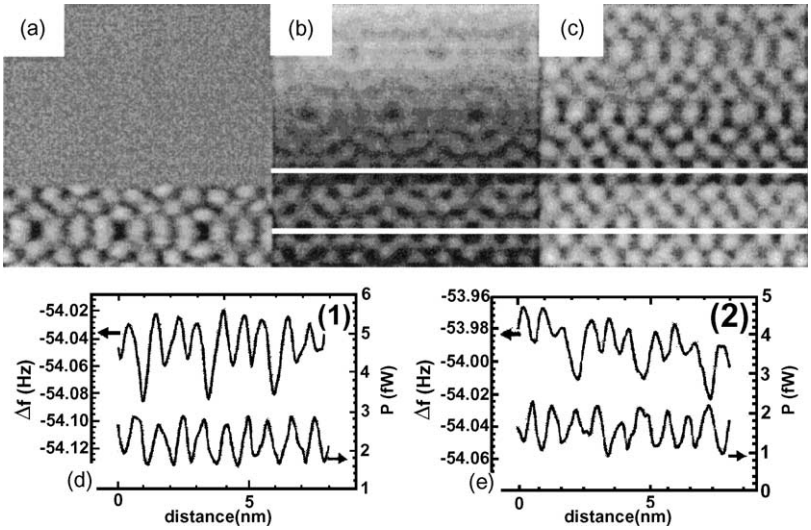

Fig. 58. (a) Topography, (b) frequency shift and (c) dissipation measured on a Si(1 1 1)-7 × 7 surface. In the lower third of the frame, the tip–sample distance was regulated to constant tunnelling current, then the regulator was switched off in order to scan at constant height. Cross-sections of the frequency shift and the dissipation before and after switching off the regulator are plotted in (d) and (e). The experimental parameters were $\bar{I}_t = 48$ pA, $f_0 = 160\,322$ Hz, $A = 8.8$ nm, $k = 28.5$ N/m, $U_{bias} = 2$ V and $Q = 15\,700$ (adapted from [237]).

In the following, we describe the measurement of dissipation in FM-AFM and identify, from the experiments, the relevant parameters, leaving the discussion of the mechanisms to the end of this section.

In all dynamic force microscopy measurements, there is an intrinsic source of dissipation caused by internal friction in the oscillating cantilever. This dissipation is characterised by the quality factor of the cantilever Q and the power dissipation P_0 is given by

$$P_0 = 2\pi f_0 \frac{kA^2/2}{Q} \tag{5.44}$$

Q can be determined in a phase variation experiment [237] for the freely oscillating cantilever. Spring constants k and oscillation amplitudes can be determined with typical 10% errors, what reflects on 25% errors for the absolute values of power dissipation.

P_0 produces a background signal in which variations of the dissipation due to the tip–sample interaction have to be measured. In order to determine the dissipation power P_{ts} from the measured A_{exc} (or gain factor [157]), it is possible to use equations developed for the intermittent contact mode AFM [87,103] modified for the FM-AFM

$$P_{ts} = P_0 \left(\frac{A_{exc}}{A_{exc,0}} - \frac{f}{f_0} \right) \tag{5.45}$$

where $A_{exc,0}$ is the excitation needed to maintain the oscillation amplitude far from the surface. Typically, $\Delta f \ll f_0 \Rightarrow f/f_0 \simeq 1$ and the first term dominates.

Gotsmann et al. [157] have studied the distance dependence of dissipative forces. They performed simulations, using Eq. (5.4), with a dissipative force $F_{ts}^{diss}(z, \dot{z}) = \gamma(z)\dot{z}$—justified for many different

dissipation mechanisms such as electronic dissipation or simple models of viscoelasticity—and an exponential decay with the absolute tip–sample distance z for the damping coefficient $\gamma(z) = \gamma_0 \exp(-z/z_0)$. The simulations support the use of Eq. (5.45) to determine P_{ts} from A_{exc} as the deviation between that equation and the direct calculation of the dissipation power in the simulation (average over one cycle of $F_{ts}^{diss}[z(t), \dot{z}(t), d]\dot{z}(t)$) is less than 0.05%. Their results show that for dissipation rates of the order of 10^{-12} W—typical of a Si tip coming into close proximity to a mica surface [157] and on a Si(7 × 7) surface [237]—there is little influence of the energy dissipation on the $\Delta f(d)$ curves. Further investigation is still needed to check if this independence of frequency shift and dissipation still holds for much larger dissipation rates—as expected on polymer samples [103]—or less strict settings of the PI controller.

These authors also show how to determine dissipative forces (or dissipation coefficients) from the dissipation power $P_{ts}(d)$ determined from experimental data, using a variation method similar to one describe in Section 5.4.1 to determine the conservative tip–sample forces from the frequency shift. The application of this analysis to measurements of an Al tip on a gold (1 1 1) surface [225] is shown in Fig. 54, where both the $P_{ts}(d)$ curve and the damping coefficient $\gamma(d)$ are displayed. These results indicate a strong damping in the contact regime, that rises rapidly as the surface is elastically deformed, and a significant amount of damping in the attractive regime. Experiments with a Si tip on mica [157] provide similar values of the dissipation power and a similar distance dependence. While the dissipation in the attractive regime on the Si/mica experiments can be attributed to the creation of image charges in the tip induced by residual static charges or thermally fluctuating charges on the mica surface, the origin of the LR dissipation in the Al/Au measurements is unclear, as both materials are good conductors and the contact potential difference is compensated during the experiments.

Notice, from Fig. 54, that the dissipation has a monotonic dependence with distance that makes it more attractive as a feedback parameter than the non-monotonic behaviour of the frequency shift. Gauthier and Tsukada [238] proposed that this behaviour could be used as the basis for a new type of force microscopy, with a feedback closer to the one of STM than to the conventional FM-AFM. Such an experiment has been already performed by Jarvis et al. [155], that emphasise the monotonic increase of dissipation as an advantage for the distance regulation.

Dürig [152] has also addressed the determination of dissipative forces from the measurement of the higher harmonics of the cantilever movement, in similarity with the method discussed in Section 5.5.2. He applied the procedure to the adhesion hysteresis measured quasi-statically with a W trimer on Au(1 1 1) [239]. He showed that the dissipative force could be recovered in an hypothetical FM-AFM experiment using a small amplitude of 1 nm measuring only cantilever harmonics terms up to the fourth-order. Notice that, according to Gotsmann et al. [157], Eq. (5.45) can be used to calculate the dissipation losses due to adhesion hysteresis effects.

Before turning to the issue of the atomically resolved dissipation contrast, we consider a set of experiments performed by Loppacher et al. [237] that explored the dependence of dissipation on distance, bias voltage and oscillation amplitude in order to reveal the contributions from LR and SR tip–sample interactions to dissipation in FM-AFM. They recorded simultaneously the frequency shift, the dissipation and the tunnelling current during approach of a Si tip to clean, atomically flat Cu(1 1 1) surfaces, taking care to stop the approach when certain threshold values of I_{tunnel} or A_{exc} were reached in order to avoid changes in the tip structure.

In the first series of measurements they explored the influence of bias voltage with a Si tip covered by Cu after prolonged scanning in contact mode. The comparison between the curves with $V_{bias} = 0.0$ V

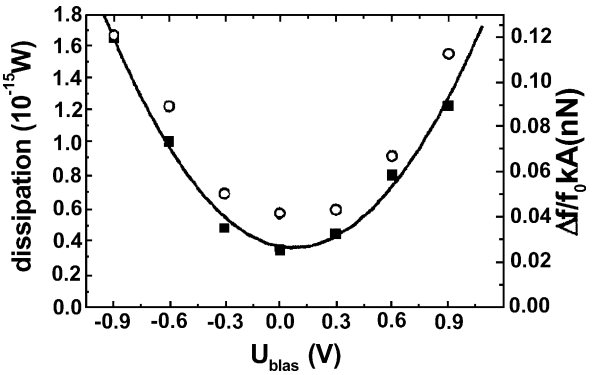

Fig. 59. Dissipation (solid squares) and reduced frequency shift (open circles) at $d = 1$ nm as a function of the bias voltage. The values are a results of an analysis of the LR contribution to the power dissipation (see text). The solid line is a parabola fitted to the dissipation data (adapted from [237]).

and $V_{\text{bias}} = 0.9$ V shows that while in both cases a steep increase in dissipation in the last nanometer before the approach is stopped, only the $V_{\text{bias}} = 0.9$ V curve presents an additional LR contribution, that can be fitted with a function $P = c/(z - z_0)^2$. Fig. 59 shows this LR contribution to the dissipation at a distance of 1 nm as a function of the bias voltage, together with the measured LR contribution to Δf, that provides a measure of the LR conservative force. Both Δf and the dissipation show a similar quadratic behaviour, that indicates that electrostatic contributions to force and dissipation are proportional to each other. The finite value at zero bias can be easily explained in Δf as the contribution from LR vdW forces. In the case of the dissipation, it may be due to remaining electrostatic forces (notice the small value 0.3×10^{-15} W), that cannot be completely eliminated as the complicated geometrical and chemical structure of the tip precludes a well-defined contact potential [237].

This electrostatic dissipation, due to the creation of dissipation currents in the silicon tip, can be described, as in intermittent contact force microscopy [87], by a phase shift $\Delta\varphi$ between the tip oscillation and the force oscillation. If the tip velocity is given by $v(t) = \omega A \cos(\omega t)$ and the force oscillation by $F(t) = F_\omega \sin(\omega t + \Delta\varphi)$, the mean dissipation power would be

$$P = \frac{\omega}{2\pi} \int_0^{2\pi/\omega} F(t) v(t)\, \mathrm{d}t = -\frac{1}{2} \omega A F_\omega \sin(\Delta\varphi) \tag{5.46}$$

where the first Fourier coefficient F_ω is related to the frequency shift by $F_\omega = kA\Delta f/f_0$. The value $(\Delta\varphi) = 1.2°$ determined using Eq. (5.46) with the results plotted in Fig. 59 for $V_{\text{bias}} = -0.9$ V has the same order of magnitude that the value determined directly in a phase variation experiment.

After subtraction of the LR contribution from Δf and dissipation, the remaining SR contributions present an exponential variation with different decay lengths (0.33–0.45 nm for Δf, and 0.21–0.28 nm for dissipation). Surprisingly, the ratio between the decay lengths of Δf, dissipation and tunnelling is always the same 1:1.5:2. As a reference, the theoretical approach of Dürig [152] to determine the relation between friction and force (same decay as Δf) would predict for exponentially decaying forces the same exponential decay for the friction with a prefactor $\kappa^{3/2}$, where κ is the decay length. For polynomial force laws $1/z^p$, the friction would be found to be proportional to $1/z^{p+3/2}$.

In a second set of measurements, they compared approach curves with a clean (sputtered) Si tip, where the contact potential has been compensated, with different oscillation amplitudes. As expected,

significant dissipation occurs only in the SR regime, but is much lower than in the variable voltage experiment, even though the forces acting on the tip are comparable. There is a clear increase of dissipation with increasing oscillation amplitude, possibly proportional to the square root dependence suggested in the models of Gotsmann et al. [157] and Gauthier and Tsukada [238].

5.6.2. Atomic contrast in the damping

Atomic contrast in A_{exc} has been obtained in metallic (Cu(1 0 0)) [140], semiconducting (Si(1 1 1)-7 × 7) [189,237,240], and ionic surfaces (NaCl islands on Cu(1 1 1)) [210]. The contrast in Cu(1 0 0) is very weak, and could be explained just by a convolution between the topography and the general distance dependence of the dissipation. That could be also the case in the data, shown in the lower part of Fig. 58, for the topography, Δf and dissipation on the Si(7 × 7) while the tip–sample distance is regulated to a constant tunnelling current. On the contrary, the constant height scans in the upper part provide a convincing proof of the true atomic-scale variation of force and dissipation. Notice that the characteristic appearance of the unit cells is not modified, with the strongest dissipation occurring above the corner holes. The reduction of the negative frequency shift with the distance (the tip drifts towards the surface while scanning without regulation) suggests that the tip is very close to the surface in these measurements. Finally, the strong atomic-scale dissipation contrast at step edges in NaCl/Cu(1 1 1) confirms that dissipation can be detected in FM-AFM with atomic resolution. However, quantitative results depend critically on the state of the tip: Experiments on NaCl/Cu(1 1 1), Cu(1 0 0) and KBr(1 0 0) [237] show that while the topography is hardly affected by a tip change—except for a change in corrugation height—the dissipation can exhibit dramatic changes. In the case of KBr(1 0 0), dissipation contrast at the step edges arises only after an accidental tip crash, while topographic images show comparable contrast.

The origins of atomic-scale dissipation, leading to atomically resolved contrast, in FM-AFM are still under debate. In the first experimental report, Lüthi et al. [189] suggested the coupling with acoustic phonons as the microscopic dissipation mechanism. Molecular dynamics simulations of FM-AFM on the Si(1 1 1)-7 × 7 by Abdurixit et al. [241] revealed that the response of surface atoms to the force exerted by the approaching tip is partially non-adiabatic despite the quasi-static movement of the tip on the atomic scale. A small amount of energy can be transferred to acoustic phonons—either directly, or via anharmonic decay of local vibrations excited by the force pulses—provided that the inverse interaction time $f\sqrt{A/\lambda}$ (f frequency of tip oscillation, A oscillation amplitude, λ decay length of the potential) lies between the highest natural frequency of the system (adatom vibration against neighbouring atoms, $f_{max} = 16$ THz) and the lowest mechanical frequency of the slab. The power dissipation connected with the non-adiabatic response was found to depend quadratically on the tip–sample interaction force. Their prediction for the relation between the decay length of force and dissipation agrees reasonably well with the experiments discussed above. However, the simulations cannot explain the inverted contrast found in the experiments: they show maximum dissipation not at the corner holes but on top of the adatoms. This can be related to the fact that the simulations include only attractive chemical forces, and the experimental results suggest that the tip is very close to contact.

Gauthier and Tsukada [238] have shown that there is dissipation in the tip–sample interaction due to thermal fluctuations even for a fully adiabatic approach of the tip towards the surface. The basic idea is to consider how the fluctuations in the position of the closest atoms in the tip and sample, that are treated as stochastic processes, are coupled by the tip–sample interaction. Their treatment of this problem, similar to the classical Brownian motion, leads to a Langevin equation for the tip motion that

contains, apart from the standard dissipation coefficient associated with the internal friction of the cantilever—described by the Q value of the cantilever—an additional dissipation coefficient

$$\gamma_{ts}[z(t)] = \frac{\pi m}{k_B T}\Theta(\omega = 0)\left(\frac{dF_{ts}|z|}{dz}\right)^2 \tag{5.47}$$

where m is the mass of the cantilever, $k_B T$ the average thermal energy, $\Theta(\omega) \propto n_v[\bar{r}, \omega]/\omega^2$, and $n_v[\bar{r}, \omega]$ the local density of phonon states (LDOSs) with frequency ω at point $\bar{r}$ over the surface. Thus, γ_{ts} is proportional to the square of the tip–sample force gradient and to the LDOS of low-lying (acoustic) phonons. This expression for γ_{ts} implies that the power dissipation is proportional to the square of the amplitude and predicts a relation for the decay lengths of dissipation and force in agreement with the experiment. The crucial step to make the predictions quantitative is to estimate $\Theta(\omega = 0)$. Gauthier and Tsukada neglected the effect of the surface (and the influence of the tip) and considered the bulk value. For Si, a Debye approximation gives $\Theta(\omega = 0)$ of the order of 10^{-5} Å^2 ps, and, assuming a simple LJ potential for the tip–sample interaction, leads to values of the power dissipation that are orders of magnitude smaller than those obtained in the FM-AFM experiments discussed above.

This problem led Gauthier and Tsukada to propose that the atomic-scale damping in FM-AFM is not mainly a consequence of the action of some microscopic dissipation mechanism but rather results from the inaccessibility of some solutions of the cantilever equation of motion [172]. Recall from the discussion in Section 5.2.7 that the stable state corresponds to the lower branch of the resonance curve. But, the amplitude of this state is somehow smaller than A_0. In constant amplitude experiments, the driving amplitude A_d would have to be increased in order to reach a state where oscillation with the prescribed A_0 amplitude were possible. In other words, some damping $\Delta A_d \neq 0$ exists even if there is no additional dissipation mechanism involved. This proposal leads to damping values that reproduce correctly the orders of magnitude of the experiments and provides atomic resolution: a simple one-dimensional model shows features and calculated corrugations that agree well with experiments.

As we emphasise in Section 5.2.7, stability and accessibility can be significantly altered when one integrates the self-driven equations of motion that describe the operation of the FM-AFM. A fully non-autonomous treatment of the real operation of the microscope [175] indicates that the interplay between the response of the electronics and the non-linear character of the tip–sample interaction—and not the stability considerations mentioned above, as these numerical simulations show that all the solutions near the resonance state are stable due to the active role of the feedback—can have an influence in the atomic-scale corrugation of the damping signal.

Finally, let us come back to a relevant aspect of dissipation not really considered by the different theoretical approaches: the extreme dependence of atomic-scale damping with tip configuration. The increase in dissipation contrast at step edges observed after a tip crash leads Loppacher et al. [237] to suggest that the tip picked up some adatoms in the crash, which may jump forth and back when the tip enters the strong force field of the step edges, while the tip stays stable above the terraces. Such instabilities would be comparable to the stick-slip processes observed in friction force microscopy but they lead to a significant higher dissipation due to the high frequency of the cantilever oscillation (which sums up the dissipation of atomic processes in each cycle). The inclusion of this type of effects, that reflect the different environment of tip and surface compared to the bulk estimation of $\Theta(0)$, in the formulation leading to Eq. (5.47) might improve the agreement with the experiments. A step in this direction is possible using the recent proposal made by Kantorovich [242] to treat the stick-slip process as a non-equilibrium process. Notice, however, that, as mentioned above, the interplay between the

electronics and the tip–sample interaction may affect the damping. The fully non-autonomous simulations by Gauthier et al. [175] show that a resonance between the scan speed and the response time of the system can provide a simple explanation for the spatial shift and contrast inversion between topographical and damping images and the extreme sensitivity of the damping to a tip change. Thus, while there is a clear physical link between the frequency shift and the tip–sample interaction, more work is needed in order to separate the intrinsic contribution of the atomic dissipation processes and that of the electronics to the observed atomically resolved damping.

6. Conclusions

The past decade has witnessed the development and impact of dAFM methods in surface, material and polymer sciences as well as in molecular biology. The remarkable versatility to study surface properties offered by a vibrating probe has originated a variety of experimental methods, applications and concepts of varying complexity that could be included under the generic name of dAFM. However, to simplify the exposition of a growing field we have restricted this report to discuss dAFM methods designed to explore the topography and spectroscopic properties of a surface as opposed to methods devoted to the study of electrostatic or magnetic properties.

According to the dominant feedback parameter used to generate an image we have distinguished between AM- and FM-AFM methods. Both methods share major physical concepts or processes such as the shift of resonance frequency due to tip–surface forces, the competition between attractive and repulsive forces to determine the tip motion, the presence of several oscillation states or the origin of contrast at nanometer scale. However, the modifications introduced in the equation of motion by the feedback process produces distinctive tip motions in amplitude and FM-AFM methods, which in turn explains and justify a separate analysis. Broadly speaking those methods have defined two different scientific communities.

Sophistication and robustness are some of the attributes that better characterise AM-AFM. Those attributes makes AM-AFM a leading technique to image surfaces in air or liquid environments. In this report we have attempted to give a comprehensive review of the major experimental and theoretical applications of this mode. Its extensive use in material and polymer sciences as well as in molecular biology or the semiconductor industry may convey the impression that AM-AFM is already an established technique. However, this is not the case. Let us just mention two applications where we expect considerable developments in the near future: high-resolution imaging in liquids and compositional characterisation.

The potential of AFM methods to investigate biological processes in situ was recognised several years ago. However, the performance of AM-AFM in liquids is still unsatisfactory. On the one hand, the experimental equipment is more involved than the one used in air environments. On the other hand, the tip motion is also more complicated due to the coupling of different oscillation modes of the microcantilever beam and the compression of the liquid layer between the tip and the surface.

Simultaneous mapping of topography and composition has always been one of the main goals of microscopic techniques. The extreme sensitivity of phase shifts to material and topographic properties has made phase images an unavoidable tool in many applications. It has opened an innovative approach to investigate material properties with nanometer resolution. However, quantitative characterisation of material properties, i.e., spectroscopy capabilities is still limited due to the lack of selectivity to isolate the specific sample property responsible for the phase shift modification. Again theoretical as well as

experimental improvements are needed to fulfil the potential of AM-AFM for characterisation of material properties.

The FM operation mode has finally fulfilled the long standing goal of true atomic resolution with AFM. FM-AFM has not only extended the atomic resolution capabilities of probe microscopies up to now unexplored insulating materials, but its combination with STM—through the use of heavily doped conducting cantilevers—promises new insight into the properties of semiconductor and metallic surfaces. The possibility of recovering the tip–sample interaction through different inversion methods adds spectroscopic capabilities, including chemical identification of different species on the surface, that have been sought for long time in STM.

Achieving atomic resolution poses stringent conditions on the tip used. Tip preparation issues have become increasingly important as experiments and theoretical approaches, including realistic calculations of the tip–sample interaction, become sophisticated enough to allow a quantitative comparison. The development of new methods to produce well characterised tips, a common trend in all the probe microscopies including STM, would be one of the key issues in the future.

However, atomic resolution is not the only advance offered by FM-AFM. As we have shown in the previous sections, FM-AFM is a very powerful tool for the accurate determination of tip–sample interactions. This provides the basis for the characterisation of material properties, like elastic constants and adhesive interactions, and tip geometry through the fitting to standard mesoscopic models. FM-AFM experiments are accurate enough to actually show the influence of SR chemical forces not accounted for in the models. On the other hand, its application to the imaging of organic systems, although still in its childhood, promises a better contrast and a more detailed imaging than the one obtained with the AM-AFM.

FM-AFM is one of those few cases where a further complication of the equipment and operation actually leads to a simpler dynamical behaviour for the cantilever. The self-driven oscillator defined by the interplay between the electronics, through the loop that keeps the oscillation amplitude constant, the non-linearity of the tip–surface interaction and the dissipation seems to be free of the complicated phase space and stability issues that play a central role in AM-AFM. The basic quantity, the frequency shift, can be described by a classical treatment of the tip–surface interaction as a perturbation of the harmonic motion described by a conservative equation, assuming that the energy losses—associated to the cantilever itself and the tip–surface interaction—are exactly compensated dynamically by the oscillation amplitude control feedback loop.

This simplified description does not probably apply to the damping, that have also been used as source of atomically resolved images, and where all the microscopic mechanisms proposed up to now to explain the dissipation fail to reproduce even the correct order of magnitude found in the experiments. Further experiments and simulations are needed to understand the role of the electronics and to identify the relevant microscopic damping mechanisms. In this sense, the FM-AFM is called to have a crucial role in the development of the emerging field of nanotribology.

Acknowledgements

One of us (RG) wishes to thank his graduate students during the writing of this report, A. San Paulo, T. Rodríguez, M. Tello and M. Calleja for multiple and clarifying discussions on dAFM issues, as well as for their assistance with the preparation of the figures. RG also acknowledges stimulating discussions

with many AFM scientists, specially C. Bustamante, J. Colchero, B. Gotsmann and G. Haugstad. RP acknowledges the long standing collaboration with the groups of Kiyoyuki Terakura and Ivan Stich on the theoretical simulation on FM-AFM, and fruitful discussions with many members of the dAFM community, in particular A. Baratoff, F.J. Giessibl, H. Hug, A. Schwarz and Y. Sugawara. This work has been supported by the Dirección General de Investigación Científica y Técnica under projects PB-98-0471 (RG) and PB-97-0028 (RP).

Appendix A. Normalised frequency shift γ

One can easily calculate the normalised frequency shift γ and its large-amplitude limit γ_{1A} (defined in Section 5.2.5) for the relevant model interactions—including, inverse-power, power law and exponential interactions—as a function of the oscillation amplitude A_0 and the distance of closest approach d.

(a) $F_{ts}(s) = C/s^n$ (inverse-power)

$$\gamma(d,A_0) = \frac{C\sqrt{A_0}}{d^n}\left[F_1^{n,1/2}\left(\frac{-2A_0}{d}\right) - F_2^{n,3/2}\left(\frac{-2A_0}{d}\right)\right] \tag{A.1}$$

where $F_c^{a,b}$ is the hypergeometric function (see, e.g., Ref. [243] for definitions and properties of these functions).

For their interest, we include here the explicit expressions in simple algebraic terms [53] for small values of n, which are suitable to describe the frequency shifts associated with electrostatic and vdW interactions

$$\begin{aligned}
\gamma_{n=1}(d,A_0) &= \frac{C}{A_0^{1/2}}\left[\frac{d/A_0+1}{\sqrt{(d/A_0+1)^2-1}} - 1\right],\\
\gamma_{n=2}(d,A_0) &= \frac{C}{A_0^{3/2}}\frac{1}{[(d/A_0+1)^2-1]^{5/2}},\\
\gamma_{n=3}(d,A_0) &= \frac{3C}{2A_0^{5/2}}\frac{d/A_0+1}{[(d/A_0+1)^2-1]^{5/2}},\\
\gamma_{n=4}(d,A_0) &= \frac{C}{2A_0^{7/2}}\frac{1+4(d/A_0+1)^2}{[(d/A_0+1)^2-1]^{7/2}},\\
\gamma_{n=5}(d,A_0) &= \frac{5C}{8A_0^{9/2}}\frac{(d/A_0+1)[3+4(d/A_0+1)^2]}{[(d/A_0+1)^2-1]^{9/2}},\\
\gamma_{n=6}(d,A_0) &= \frac{3C}{8A_0^{11/2}}\frac{(d/A_0+1)+12(d/A_0+1)^2+8(d/A_0+1)^4}{[(d/A_0+1)^2-1]^{11/2}}
\end{aligned} \tag{A.2}$$

The large-amplitude limit γ_{1A} is given by

$$\gamma_{1A}(d) = \frac{1}{\sqrt{2\pi}}\frac{\Gamma(n-1/2)}{\Gamma(n)}\frac{C}{d^{n-1/2}} \tag{A.3}$$

where $\Gamma(n)$ is the gamma function [243] ($\Gamma(n-1/2) = \sqrt{\pi}(2n-3)!!/2^{n-1}$ and $\Gamma(n) = (n-1)!$).

(b) $F_{ts}(s) = C(-s)^m$ for $s < 0$ and $F_{ts} = 0$ for $s > 0$ (power law)

$$\gamma(d, A_0) = \frac{C|d|^{m+1/2}\Gamma(m+1)}{\sqrt{2\pi}}\left[\frac{F^{1/2,1/2}_{m+3/2}(-2A_0/d)}{\Gamma(m+3/2)} + \frac{d}{2A_0}\frac{F^{1/2,3/2}_{m+5/2}(-2A_0/d)}{\Gamma(m+5/2)}\right] \tag{A.4}$$

$$\gamma_{lA}(d) = \frac{1}{\sqrt{2\pi}}\frac{\Gamma(m+1)}{\Gamma(m+3/2)}C(-d)^{m+1/2} \quad \text{for } s < 0 \tag{A.5}$$

(c) $F_{ts}(s) = C\exp(-\kappa s)$ (exponential forces)

$$\gamma(d, A_0) = C\exp(-\kappa d)\sqrt{A_0}[M_1^{1/2}(-2\kappa A_0) - M_2^{3/2}(-2\kappa A_0)] \tag{A.6}$$

with M_b^a the Kummer function [243]

$$\gamma_{lA}(d) = \frac{C\exp(-\kappa d)}{\sqrt{2\pi\kappa}} \tag{A.7}$$

References

[1] G. Binnig, C. Gerber, C. Quate, Phys. Rev. Lett. 56 (1986) 930.
[2] Y. Martin, C.C. Williams, H.K. Wickramasinghe, J. Appl. Phys. 61 (1987) 4723.
[3] T.R. Albrecht, P. Grütter, D. Horne, D. Rugar, J. Appl. Phys. 69 (1991) 668.
[4] D. Anselmetti, R. Lüthi, E. Meyer, T. Richmond, M. Dreier, J.E. Frommer, H.-J. Güntherodt, Nanotechnology 5 (1994) 87.
[5] C. Bustamante, D. Keller, Phys. Today 48 (1995) 33.
[6] C. Möller, M. Allen, V. Elings, A. Engel, D. Müller, Biophys. J. 77 (1999) 1150.
[7] A. San Paulo, R. García, Biophys. J. 78 (2000) 1599.
[8] G. Reiter, G. Castelein, P. Hoerner, G. Riess, J.-U. Sommer, G. Floudas, Eur. Phys. J. E 2 (2000) 319.
[9] F.J. Giessibl, Science 267 (1995) 68–71.
[10] Y. Sugawara, M. Otha, H. Ueyama, S. Morita, Science 270 (1995) 1646.
[11] S. Kitamura, M. Iwatsuki, Jpn. J. Appl. Phys. 35 (1995) L145.
[12] R. García, M. Calleja, F. Pérez-Murano, Appl. Phys. Lett. 72 (1998) 2295.
[13] Q. Zhong, D. Imniss, K. Kjoller, V.B. Elings, Surf. Sci. 290 (1993) L688.
[14] W. Han, S.M. Lindsay, T. Jing, Appl. Phys. Lett. 69 (1996) 4111.
[15] H.J. Butt, M. Jaschke, Nanotechnology 6 (1995) 1.
[16] J.E. Sader, J. Appl. Phys. 84 (1998) 64.
[17] R.W. Stark, W.M. Heckl, Surf. Sci. 457 (2000) 219.
[18] J. Chen, R.K. Workman, D. Sarid, R. Höper, Nanotechnology 5 (1994) 199.
[19] D. Sarid, T.G. Ruskell, R.K. Workman, D. Chen, J. Vac. Sci. Technol. B 14 (1996) 864.
[20] B. Anczykowski, D. Krüger, H. Fuchs, Phys. Rev. B 53 (1996) 15485.
[21] J. Tamayo, R. García, Langmuir 12 (1996) 4430.
[22] R.G. Winkler, J.P. Spatz, S. Sheiko, M. Möller, P. Reineker, O. Marti, Phys. Rev. B 54 (1996) 8908.
[23] A. Kühle, A.H. Soerensen, J. Bohr, J. Appl. Phys. 81 (1997) 6562.
[24] N.A. Burham, O.P. Behrend, F. Oulevey, G. Gremaud, P.-J. Gallo, D. Gourdon, E. Dupas, A.J. Kulik, H.M. Pollock, G.A.D. Briggs, Nanotechnology 8 (1997) 67.
[25] R. García, A. San Paulo, Phys. Rev. B 60 (1999) 4961.
[26] L. Wang, Surf. Sci. 429 (1999) 178.
[27] L. Wang, Appl. Phys. Lett. 73 (1998) 3781.

[28] L. Nony, R. Boisgard, J.P. Aimé, J. Chem. Phys. 111 (1999) 1615.
[29] J.P. Aimé, R. Boisgard, L. Nony, G. Gauthier, Phys. Rev. Lett. 82 (1999) 3388.
[30] M. Marth, D. Maier, J. Honerkamp, R. Brandsch, G. Bar, J. Appl. Phys. 85 (1999) 7030.
[31] M.V. Salapaka, D.J. Chen, J.P. Cleveland, Phys. Rev. B 62 (2000) 1106.
[32] O. Sahin, A. Atalar, Appl. Phys. Lett. 78 (2001) 2973.
[33] B. Anczykowski, D. Krüger, K.L. Babcock, H. Fuchs, Ultramicroscopy 66 (1996) 251.
[34] J. Israelachvili, Intermolecular and Surface Forces, Academic Press, London, 1992, and references therein.
[35] U. Hartman, in: Theory of STM and Related Scanning Probe Methods, Springer, Berlin, 1993.
[36] K.L. Johnson, K. Kendall, A.D. Roberts, Proc. R. Soc. London Ser. A 324 (1971) 301.
[37] B.V. Derjaguin, V.M. Muller, Y.P. Toporov, J. Colloid. Interf. Sci. 53 (1975) 314.
[38] D. Maugis, J. Colloid. Interf. Sci. 150 (1992) 243.
[39] V.M. Muller, V.S. Yushenko, B.V. Derjaguin, J. Colloid. Interf. Sci. 92 (1983) 92.
[40] J.A. Greenwood, K.L. Johnson, Phil. Mag. 43 (1981) 697.
[41] W.N. Unertl, J. Vac. Sci. Technol. A 17 (1999) 1779.
[42] B. Capella, G. Dietler, Surf. Sci. Rep. 34 (1999) 1.
[43] R. García, M. Calleja, H. Rohrer, J. Appl. Phys. 86 (1999) 1898.
[44] J. Colchero, A. Storch, M. Luna, J. Gómez-Herrero, A.M. Baró, Langmuir 14 (1998) 2230.
[45] T. Stiffer, O. Marti, B. Bhushan, Phys. Rev. B 62 (2000) 13667.
[46] A. Valencia, M. Brinkmann, R. Lipowsky, Langmuir 17 (2001) 3390.
[47] M. Nonnenmacher, M.P. O'Boyle, H.K. Wickramasinghe, Appl. Phys. Lett. 58 (1991) 2921.
[48] A.P. French, Vibrations and Waves, The MIT Introductory Physics Series, W.W. Norton and Co., New York, 1971.
[49] G.Y. Chen, R.J. Warmack, A. Huang, T. Thundat, J. Appl. Phys. 78 (1995) 1465.
[50] S.N. Magonov, V. Elings, M.-H. Whangbo, Surf. Sci. 375 (1997) L385.
[51] M.H. Whangbo, G. Bar, R. Brandsch, Surf. Sci. 411 (1998) L794.
[52] G. Bar, R. Brandsch, M.H. Whangbo, Surf. Sci. 411 (1998) L802.
[53] H. Hölscher, U.D. Schwarz, R. Weisendanger, Appl. Surf. Sci. 140 (1999) 344.
[54] P. Gleyces, P.K. Kuo, A.C. Boccara, Appl. Phys. Lett. 58 (1991) 2928.
[55] R. Boisgard, D. Michel, J.P. Aimé, Surf. Sci. 401 (1998) 199.
[56] R. García, A. San Paulo, Phys. Rev. 61 (2000) R13381.
[57] A. San Paulo, R. García, Phys. Rev. B 66 (2002) 041406(R).
[58] X. Chen, M.C. Davies, C.J. Roberts, S.J.B. Tendler, P.M. Williams, N.A. Burnham, Surf. Sci. 460 (2000) 292.
[59] W. van der Water, J. Molenaar, Nanotechnology 11 (2000) 192.
[60] N. Sasaki, M. Tsukada, R. Tamura, K. Abe, N. Sato, Appl. Phys. A 66 (1998) S287.
[61] J.P. Hunt, D. Sarid, Appl. Phys. Lett. 72 (1998) 2969.
[62] J.M.T. Thompson, H.B. Stewart, Nonlinear Dynamics and Chaos, Wiley, Chichester, UK, 1997.
[63] A. Kühle, A.H. Sorensen, J.B. Zandbergen, J. Bohr, Appl. Phys. A 66 (1998) S329.
[64] P.J. de Pablo, J. Colchero, M. Luna, J. Gómez-Herrero, A.M. Baró, Phys. Rev. 61 (2000) 14179.
[65] R. García, A. San Paulo, Ultramicroscopy 82 (2000) 79.
[66] G. Haugstad, R. Jones, Ultramicroscopy 76 (1999) 77.
[67] P.K. Hansma et al., Appl. Phys. Lett. 64 (1994) 1738.
[68] F. Moreno-Herrero, P.J. de Pablo, J. Colchero, J. Gómez-Herrero, A.M. Baró, Surf. Sci. 453 (2000) 152.
[69] S.C. Fain, K.A. Barry, M.G. Bush, B. Pettiger, R.N. Loie, Appl. Phys. Lett. 76 (2000) 930.
[70] A. San Paulo, R. García, Phys. Rev. B 64 (2001) 1934.
[71] T.R. Rodríguez, R. García, Appl. Phys. Lett. 80 (2002) 1646.
[72] F.M. Ohnesorge, Surf. Interf. Anal. 27 (1999) 279.
[73] D. Keller, F.S. Franke, Surf. Sci. 294 (1993) 409.
[74] J. Vesenka, S. Manne, R. Giberson, T. Maersh, E. Henderson, Biophys. J. 65 (1993) 992.
[75] F. Biscarini, P. Levy, Appl. Phys. Lett. 71 (1997) 888.
[76] N.F. van Hulst, M. García-Parajo, M.F. Moers, M.H.P. Veerman, A.G.T. Ruiter, J. Struct. Biol. 119 (1997) 222.
[77] D.J. Muller, A. Engel, Biophys. J. 73 (1997) 1633.
[78] R.M. Overney, E. Meyer, J. Frommer, H.-J. Güntherodt, M. Fujihira, H. Takano, Y. Gotoh, Langmuir 10 (1994) 1281.

[79] R. García, J. Tamayo, L. González, Y. González, Micro/Nanotribology and Its Applications, Kluwer Academic Publishers, Dordrecht, The Netherlands, 1997, pp. 275–282.
[80] E.L. Florin, V.T. Moy, H.E. Gaub, Science 264 (1994) 415.
[81] E.W. Van der Vegte, G. Hadziannou, Langmuir 13 (1997) 4357.
[82] U. Rabe, W. Arnold, Appl. Phys. Lett. 64 (1994) 1493.
[83] K. Yamanaka, H. Ogiso, O. Kolosov, Appl. Phys. Lett. 64 (1994) 178.
[84] D. Chernoff, in: Proceedings of the Microscopy and Microanalysis 888, MSA, Jones and Begell Publishing, New York, 1995.
[85] J. Tamayo, R. García, Appl. Phys. Lett. 71 (1997) 2394.
[86] S.N. Magonov, V. Elings, V.S. Papkov, Polymer 38 (1997) 297.
[87] J.P. Cleveland, B. Anczykowski, A.E. Schmid, V.B. Elings, Appl. Phys. Lett. 72 (1998) 2613.
[88] A. Noy, C.H. Sanders, D.V. Vezenov, S.S. Wong, C. Lieber, Langmuir 14 (1998) 1508.
[89] G. Bar, R. Brandsch, M.-H. Whangbo, Langmuir 14 (1998) 7343.
[90] G. Bar, Y. Thomann, M.H. Whangbo, Langmuir 14 (1998) 1219.
[91] M. Czajkowsky, M. Allen, V. Elings, Z. Shao, Ultramicroscopy 74 (1998) 1.
[92] R. García, J. Tamayo, M. Calleja, F. García, Appl. Phys. A 66 (1998) S309.
[93] X. Chen, M.C. Davies, C.J. Roberts, S.J.B. Tendler, P.M. Williams, J. Davies, A.C. Dawkes, J.C. Edwards, Ultramicroscopy 75 (1998) 171.
[94] O.P. Behrend, L. Odoni, J.L. Loubet, N.A. Burnham, Appl. Phys. Lett. 75 (1999) 2551.
[95] R. García, J. Tamayo, A. San Paulo, Surf. Interf. Anal. 27 (1999) 312.
[96] P.J. James, M. Antognozzi, J. Tamayo, T.J. McMaster, J.M. Newton, M.J. Miles, Langmuir 17 (2001) 349.
[97] G. Reiter, G. Castelein, J.U. Sommer, A. Röttele, T. Thurn-Albrecht, Phys. Rev. Lett. 87 (2001) 2261.
[98] TappingMode AFM, Digital Instruments, Santa Barbara, USA.
[99] J. Tamayo, R. García, Appl. Phys. Lett. 73 (1998) 2926.
[100] M. Stark, C. Möller, D.J. Müller, R. Guckenberger, Biophys. J. 80 (2001) 3009.
[101] J.B. Pethica, W.C. Oliver, Phys. Scripta T 19 (1987) 61.
[102] G. Bar, L. Delineau, R. Brandsch, M. Bruch, M.-H. Wangbo, Appl. Phys. Lett. 75 (1999) 4198.
[103] B. Anczykowski, B. Gotsmann, H. Fuchs, J.P. Cleveland, V.B. Elings, Appl. Surf. Sci. 140 (1999) 376.
[104] M. Bezanilla, B. Drake, E. Nudler, M. Kashev, P.K. Hansma, H.G. Hansma, Biophys. J. 67 (1994) 2454.
[105] Y.L. Lyubchenko, L.S. Shlyakhtenko, Proc. Natl. Acad. Sci. USA 94 (1997) 496.
[106] D.D. Dunlap, A. Maggi, M.R. Soria, L. Monaco, Nucleic Acids Res. 25 (1997) 3095.
[107] G. Zuccheri, A. Scipioni, V. Cavalieri, G. Gargiulo, P. De Santis, B. Samori, Proc. Natl. Acad. Sci. USA 98 (2001) 3074.
[108] C. Rivetti, M. Guthold, C. Bustamante, J. Mol. Biol. 264 (1996) 919.
[109] C. Rivetti, M. Guthold, C. Bustamante, J. Mol. Biol. 280 (1998) 41.
[110] M. Valle, J.M. Valpuesta, J.L. Carrascosa, J. Tamayo, R. García, J. Struct. Biol. 116 (1996) 390.
[111] V.J. Morris, A.R. Kirby, A.P. Gunning, Atomic Force Microscopy for Biologists, Imperial College Press, London, 1999.
[112] S.N. Magonov, D. Reneker, Annu. Rev. Mater. Sci. 27 (1997) 175 and references therein.
[113] A. San Paulo, R. García, Surf. Sci. 471 (2000) 71.
[114] S. Kopp-Marsaudon, Ph. Leclère, F. Dubourg, R. Lazzaroni, J.P. Aimé, Langmuir 16 (2000) 8432.
[115] Image courtesy of Advance Surface Microscopy, Inc., USA.
[116] G. Binnig, H. Rohrer, Rev. Mod. Phys. 71 (1999) S324.
[117] T. Junno, K. Deppert, L. Montelius, L. Samuleson, Appl. Phys. Lett. 66 (1995) 3627.
[118] T. Junno, S.-B. Carlsson, H. Xu, L. Montelius, L. Samuelson, Appl. Phys. Lett. 72 (1998) 548.
[119] T.R. Ramachandran, C. Baur, A. Bugacov, A. Madhukar, B.E. Koel, A. Requicha, C. Gazen, Nanotechnology 9 (1998) 237.
[120] E.S. Snow, D. Park, P.M. Campbell, Appl. Phys. Lett. 69 (1996) 269.
[121] J.A. Dagata, T. Inoue, J. Itoh, K. Matsumoto, H. Yokoyama, J. Appl. Phys. 84 (1998) 6891.
[122] M. Tello, R. García, Appl. Phys. Lett. 79 (2001) 424.
[123] H.G. Hansma, J. Vac. Sci. Technol. B 14 (1996) 1390.
[124] C.A. Putmam, K.O. Van der Werf, B.G. De Grooth, N.F. Van Hulst, J. Greve, Appl. Phys. Lett. 64 (1994) 2454.

[125] T.E. Schäffer, J.P. Cleveland, F. Ohnesorge, D.A. Walters, P.K. Hansma, J. Appl. Phys. 80 (1996) 3622.
[126] S.J. O'Shea, M.A. Lantz, H. Tokumoto, Langmuir 15 (1999) 922.
[127] G.Y. Chen, R.J. Warmack, A. Huang, T. Thundat, J. Appl. Phys. 78 (1995) 1465.
[128] M. Lantz, Y.Z. Liu, X.D. Cui, H. Tokumoto, S.M. Lindsay, Surf. Interf. Anal. 27 (1999) 354.
[129] J.W.M. Chon, P. Mulvaney, J.E. Sader, J. Appl. Phys. 87 (2000) 3978.
[130] M.P. Scherer, G. Frank, A.W. Gummer, J. Appl. Phys. 88 (2000) 2912.
[131] J. Tamayo, A.D.L. Humphris, R.J. Owen, M.J. Miles, Biophys. J. 81 (2001) 526.
[132] B. Anczykowski, J.P. Cleveland, D. Krüger, V. Elings, H. Fuchs, Appl. Phys. A 66 (1998) S885.
[133] R.D. Jäggi, A. Franco-Obregón, P. Stederus, K. Ensslin, Appl. Phys. Lett. 79 (2001) 135.
[134] F.J. Giessibl, Phys. Rev. B 56 (1997) 16010.
[135] G.M. McClelland, R. Erlandsson, S. Chiang, Rev. Prog. Quant. Nondestruct. Eval. 6 (1987) 1307.
[136] C. Loppacher, M. Bammerlin, F. Battiston, M. Guggisberg, D. Müller, H.R. Hidber, R. Lüthi, E. Meyer, H.-J. Guntherodt, Appl. Phys. A 66 (1998) S215.
[137] F.J. Giessibl, Jpn. J. Appl. Phys. 33 (1994) 3726.
[138] S. Orisaka, T. Minobe, T. Uchihashi, Y. Sugawara, S. Morita, Appl. Surf. Sci. 140 (1999) 243.
[139] C. Loppacher, M. Bammerlin, M. Guggisberg, F. Battiston, R. Bennewitz, S. Rast, A. Baratoff, E. Meyer, H.-J. Guntherodt, Appl. Surf. Sci. 140 (1999) 287.
[140] C. Loppacher, M. Bammerlin, M. Guggisberg, S. Schär, R. Bennewitz, A. Baratoff, E. Meyer, H.-J. Guntherodt, Phys. Rev. B 62 (2000) 16944.
[141] T. Minobe, T. Uchihashi, T. Tsukamoto, S. Orisaka, Y. Sugawara, S. Morita, Appl. Surf. Sci. 140 (1999) 298.
[142] Y. Sugawara, S. Orisaka, S. Morita, Appl. Surf. Sci. 157 (2000) 239.
[143] T. Uchihashi, Y. Sugawara, T. Tsukamoto, M. Ohta, S. Morita, M. Suzuki, Phys. Rev. B 56 (1997) 9834.
[144] M.A. Lantz, H.J. Hug, P.J.A. van Schendel, R. Hoffmann, S. Martin, A. Baratoff, A. Abdurixit, H.-J. Guntherodt, Ch. Gerber, Phys. Rev. Lett. 84 (2000) 2642.
[145] W. Allers, A. Schwarz, U.D. Schwarz, R. Wiesendanger, Europhys. Lett. 48 (1999) 276.
[146] M.A. Lantz, H.J. Hug, R. Hoffmann, P.J.A. van Schendel, P. Kappenberger, S. Martin, A. Baratoff, H.-J. Guntherodt, Science 291 (2001) 2580.
[147] A.S. Foster, C. Barth, A.L. Shluger, M. Reichling, Phys. Rev. Lett. 86 (2001) 2373.
[148] Y. Maeda, T. Matsumoto, T. Kawai, Appl. Surf. Sci. 140 (1999) 400.
[149] T. Uchihashi, T. Ishida, M. Komiyama, M. Ashino, Y. Sugawara, W. Mizutani, K. Yokoyama, S. Morita, H. Tokumoto, M. Ishikawa, Appl. Surf. Sci. 157 (2000) 244.
[150] F.J. Giessibl, H. Bielefeldt, S. Hembacher, J. Mannhart, Appl. Surf. Sci. 140 (1999) 352.
[151] U. Dürig, Appl. Phys. Lett. 75 (1999) 433.
[152] U. Dürig, New J. Phys. 2 (2000) 5.1–5.12.
[153] F.J. Giessibl, S. Hembacher, H. Bielefeldt, J. Mannhart, Science 289 (2000) 422.
[154] S.P. Jarvis, H. Yamada, S.-I. Yamamoto, H. Tokumoto, J.B. Pethica, Nature 384 (1996) 247.
[155] S.P. Jarvis, H. Yamada, K. Kobayashi, A. Toda, H. Tokumoto, Appl. Surf. Sci. 157 (2000) 314.
[156] A. Oral, R.A. Grimble, H. Özgür Özer, P.M. Hoffmann, J.B. Pethica, Appl. Phys. Lett. 79 (2001) 1915.
[157] B. Gotsmann, C. Seidel, B. Anczykowski, H. Fuchs, Phys. Rev. B 60 (1999) 11051.
[158] J. Tobik, I. Stich, R. Perez, K. Terakura, Phys. Rev. B 60 (1999) 11639.
[159] I. Stich, J. Tobik, R. Perez, K. Terakura, S.H. Ke, Prog. Surf. Sci. 64 (2000) 179.
[160] A.I. Livshits, A.L. Shluger, A.L. Rohl, A.S. Foster, Phys. Rev. B 59 (1999) 2436.
[161] N. Sasaki, M. Tsukada, Appl. Surf. Sci. 140 (1999) 339.
[162] N. Sasaki, M. Tsukada, Jpn. J. Appl. Phys. 38 (1999) 192.
[163] F.J. Giessibl, H. Bielefeldt, Phys. Rev. B 61 (2000) 9968.
[164] H. Hölscher, A. Schwarz, W. Allers, U.D. Schwarz, R. Wiesendanger, Phys. Rev. B 61 (2000) 12678.
[165] J. Tersoff, D.R. Hamann, Phys. Rev. Lett. 50 (1983) 1998.
[166] S.H. Ke, T. Uda, R. Perez, I. Stich, K. Terakura, Phys. Rev. B 59 (1999) 13267.
[167] U.D. Schwarz, H. Holscher, R. Wiesendanger, Phys. Rev. B 62 (2000) 13089.
[168] R. Perez, M.C. Payne, I. Stich, K. Terakura, Phys. Rev. Lett. 78 (1997) 678.
[169] R. Perez, I. Stich, M.C. Payne, K. Terakura, Phys. Rev. B 58 (1998) 10835.

[170] H. Hölscher, W. Allers, U.D. Schwarz, A. Schwarz, R. Wiesendanger, Appl. Phys. A 72 (2001) S35.
[171] F.J. Giessibl, H. Bielefeldt, S. Hembacher, J. Mannhart, Ann. Phys. Berlin 10 (2001) 887.
[172] M. Gauthier, M. Tsukada, Phys. Rev. Lett. 85 (2000) 5348.
[173] M. Gauthier, N. Sasaki, M. Tsukada, Phys. Rev. B 64 (2001) 085409.
[174] N. Bogoliubov, Y.A. Mitropolsky, Asymptotic Methods in the Theory of Nonlinear Oscillations, Gordon and Breach, New York, 1961.
[175] M. Gauthier, R. Perez, T. Arai, M. Tomitori, M. Tsukada, Interplay between nonlinearity, scan speed, damping, and electronics in frequency modulation atomic force microscopy, Phys. Rev. Lett. (2002), in press.
[176] J.P. Aime, G. Couturier, R. Boisgard, L. Nony, Appl. Surf. Sci. 140 (1999) 333.
[177] F.H. Stillinger, T.A. Weber, Phys. Rev. B 31 (1985) 5262.
[178] J. Tersoff, Phys. Rev. B 38 (1988) 9902.
[179] R. Perez, P. Gumbsch, Phys. Rev. Lett. 84 (2000) 5347.
[180] R. Perez, P. Gumbsch, Acta Mater. 48 (2000) 4517.
[181] P.M. Hoffmann, R.A. Grimble, S. Jeffery, J.B. Pethica, A. Oral, H. Özgür Özer, Proc. R. Soc. A 457 (2001) 1161.
[182] A.L. Shluger, A.I. Livshits, A.S. Foster, C.R.A. Catlow, J. Phys. Condens. Matt. 11 (1999) R295.
[183] W. Allers, A. Schwarz, U.D. Schwarz, R. Wiesendanger, Appl. Surf. Sci. 140 (1999) 247.
[184] H. Hölscher, A. Schwarz, W. Allers, U.D. Schwarz, R. Wiesendanger, Phys. Rev. B 62 (2000) 6967.
[185] M. Guggisberg, M. Bammerlin, C. Loppacher, O. Pfeiffer, A. Abdurixit, V. Barwich, R. Bennewitz, A. Baratoff, E. Meyer, H.-J. Guntherodt, Phys. Rev. B 61 (2000) 11151.
[186] F.J. Giessibl, Phys. Rev. B 45 (1992) 13815.
[187] R. Erlandsson, L. Olsson, P. Martensson, Phys. Rev. B 54 (1996) R8309.
[188] N. Nakagiri, M. Suzuki, K. Okiguchi, H. Sugimura, Surf. Sci. 373 (1997) L329.
[189] R. Lüthi, E. Meyer, M. Bammerlin, A. Baratoff, L. Howald, Ch. Gerber, H.-J. Guntherodt, Surf. Rev. Lett. 4 (1997) 1025.
[190] N. Suehira, Y. Sugawara, S. Morita, Jpn. J. Appl. Phys. 40 (2001) L1.
[191] K. Takayanagi, Y. Tanishiro, M. Takahashi, S. Takahashi, J. Vac. Sci. Technol. A 3 (1985) 1502.
[192] S. Morita, Y. Sugawara, K. Yokohama, T. Uchihashi, Nanotechnology 11 (2000) 1.
[193] W.A. Hofer, A.J. Fisher, R.A. Wolkow, P. Grutter, Phys. Rev. Lett. 87 (2001) 236104.
[194] S.H. Ke, T. Uda, K. Terakura, Phys. Rev. B 62 (2000) 15319.
[195] K.D. Brommer, M. Needels, B.E. Larson, J.D. Joannopoulos, Phys. Rev. Lett. 68 (1992) 1355.
[196] I. Stich, M.C. Payne, R.D. King-Smith, J.-S. Lin, L.J. Clarke, Phys. Rev. Lett. 68 (1992) 1351.
[197] S.Y. Tong, H. Huang, C.M. Wei, W.E. Packard, F.K. Men, G. Glander, M.B. Webb, J. Vac. Sci. Technol. A 6 (1988) 615.
[198] H. Ueyama, M. Ohta, Y. Sugawara, S. Morita, Jpn. J. Appl. Phys. 34 (1995) L1086.
[199] Y. Sugawara, H. Ueyama, T. Uchihashi, M. Ohta, S. Morita, M. Suzuki, S. Mishima, Appl. Surf. Sci. 113/114 (1997) 364.
[200] Y. Sugawara, T. Uchihashi, M. Abe, S. Morita, Appl. Surf. Sci. 140 (1999) 371.
[201] A. Schwarz, W. Allers, U.D. Schwarz, R. Wiesendanger, Appl. Surf. Sci. 140 (1999) 293.
[202] A. Schwarz, W. Allers, U.D. Schwarz, R. Wiesendanger, Phys. Rev. B 61 (2000) 2837.
[203] H. Hosoi, K. Sueoka, K. Hakayama, K. Mukasa, Appl. Surf. Sci. 157 (2000) 218.
[204] S.H. Ke, T. Uda, R. Perez, I. Stich, K. Terakura, Phys. Rev. B 60 (1999) 11631.
[205] S.H. Ke, T. Uda, I. Stich, K. Terakura, Phys. Rev. B 63 (2001) 245323.
[206] J. Tobik, I. Stich, K. Terakura, Phys. Rev. B 63 (2001) 245324.
[207] L.N. Kantorovich, A.S. Foster, A.L. Shluger, A.M. Stoneham, Surf. Sci. 445 (2000) 283.
[208] M. Bammerlin, R. Lüthi, E. Meyer, A. Baratoff, J. Lü, M. Guggisberg, C. Gerber, L. Howald, H.-J. Guntherodt, Probe Microscopy 1 (1997) 3.
[209] M. Bammerlin, R. Lüthi, E. Meyer, A. Baratoff, J. Lü, M. Guggisberg, C. Loppacher, C. Gerber, H.-J. Guntherodt, Appl. Phys. A 66 (1998) S293.
[210] R. Bennewitz, A.S. Foster, L.N. Kantorovich, M. Bammerlin, Ch. Loppacher, S. Schär, M. Guggisberg, E. Meyer, A.L. Shluger, Phys. Rev. B 62 (2000) 2074.
[211] R. Bennewitz, T. Gyalog, M. Guggisberg, M. Bammerlin, E. Meyer, H.-J. Guntherodt, Phys. Rev. B 60 (1999) R11301.

[212] M. Reichling, C. Barth, Phys. Rev. Lett. 83 (1999) 768.
[213] C. Barth, M. Reichling, Surf. Sci. 470 (2000) L99.
[214] C. Barth, A.S. Foster, M. Reichling, A.L. Shluger, J. Phys. Condens. Matt. 13 (2001) 2061.
[215] K. Fukui, H. Onishi, Y. Iwasawa, Phys. Rev. Lett. 79 (1997) 4202.
[216] K. Fukui, H. Onishi, Y. Iwasawa, Appl. Surf. Sci. 140 (1999) 259.
[217] H. Raza, C.L. Pang, S.A. Haycock, G. Thornton, Appl. Surf. Sci. 140 (1999) 271.
[218] C.L. Pang, H. Raza, S.A. Haycock, G. Thornton, Appl. Surf. Sci. 157 (2000) 233.
[219] M. Ashino, Y. Sugawara, S. Morita, M. Ishikawa, Phys. Rev. Lett. 86 (2001) 4334.
[220] M. Ashino, T. Uchihashi, K. Yokohama, Y. Sugawara, S. Morita, M. Ishikawa, Appl. Surf. Sci. 157 (2000) 212.
[221] J. Wintterlin, J. Wiechers, H. Brune, T. Gritsch, H. Hofer, R.J. Behm, Phys. Rev. Lett. 62 (1989) 59.
[222] R. Perez, F.J. Garcia-Vidal, P.L. de Andres, F. Flores, Surf. Sci. 307–309 (1994) 704.
[223] J. Nunes, M. Scheffler, private communication.
[224] B. Gotsmann, B. Anczykowski, C. Seidel, H. Fuchs, Appl. Surf. Sci. 150 (1999) 314.
[225] B. Gotsmann, H. Fuchs, Phys. Rev. Lett. 86 (2001) 2597.
[226] A. Schirmeisen, G. Cross, A. Stalder, P. Grütter, M. Tschudy, U. Dürig, Appl. Surf. Sci. 157 (2000) 274.
[227] H. Hölscher, W. Allers, U.D. Schwarz, A. Schwarz, R. Wiesendanger, Phys. Rev. Lett. 83 (1999) 4780.
[228] L.D. Landau, E.M. Lifshitz, Mechanics: Course of Theoretical Physics, Vol. 1, third ed., Pergamon Press, Oxford, 1976.
[229] U. Dürig, Appl. Phys. Lett. 76 (2000) 1203.
[230] F.J. Giessibl, Appl. Phys. Lett. 76 (2000) 1470.
[231] F.J. Giessibl, S. Hembacher, H. Bielefeldt, J. Mannhart, Science 291 (2001) 2509.
[232] T. Arai, M. Tomitori, Appl. Surf. Sci. 157 (2000) 207.
[233] A. Baratoff, et al., private communication.
[234] E. Gnecco, R. Bennewitz, T. Gyalog, C. Loppacher, M. Bammerlin, E. Meyer, H.-J. Guntherodt, Phys. Rev. Lett. 84 (2000) 1172.
[235] W. Denk, D. Pohl, Appl. Phys. Lett. 59 (1991) 2171.
[236] T. Stowe, T. Kenny, D. Thomson, D. Rugar, Appl. Phys. Lett. 75 (1999) 2785.
[237] C. Loppacher, R. Bennewitz, O. Pfeiffer, M. Guggisberg, M. Bammerlin, S. Schär, V. Barwich, A. Baratoff, E. Meyer, Phys. Rev. B 62 (2000) 13674.
[238] M. Gauthier, M. Tsukada, Phys. Rev. B 60 (1999) 11716.
[239] G. Cross, A. Schirmeisen, A. Stalder, P. Grütter, M. Tschudy, U. Dürig, Phys. Rev. Lett. 80 (1998) 4685.
[240] M. Guggisberg, M. Bammerlin, A. Baratoff, R. Lüthi, C. Loppacher, F. Battiston, J. Lü, R. Bennewitz, E. Meyer, H.-J. Guntherodt, Surf. Sci. 461 (2000) 255.
[241] A. Abdurixit, A. Baratoff, E. Meyer, Appl. Surf. Sci. 157 (2000) 355.
[242] L.N. Kantorovich, J. Phys. Condens. Matt. 13 (2001) 945.
[243] M. Abramowitz, I.A. Stegun, Handbook of Mathematical Functions, ninth ed., Dover, New York, 1970.